MAGNETIC RESONANCE IMAGING OF THE LUNG

MAGNETIC RESONANCE IMAGING OF THE LUNG AT 3 AND 1.5 TESLA

By

SERGEI I. OBRUCHKOV, B.Sc.

A Thesis

Submitted to the School of Graduate Studies

in Partial Fulfilment of the Requirements

for the Degree

Master Of Science

McMaster University

MASTER OF SCIENCE (2006) McMaster University

(Medical Physics and Applied Radiation Sciences) Hamilton, Ontario

TITLE: Magnetic Resonance Imaging Of The Lung At 3 and 1.5 Tesla

AUTHOR: Sergei I. Obruchkov, B.Sc.(Dalhousie University)

SUPERVISOR: Professor M.D. Noseworthy

NUMBER OF PAGES: xvi, 129

Abstract

Routine lung imaging is most often done using nuclear medicine techniques, and more recently using hyperpolarized gas MR. The former suffers from radiation and poor spatial resolution, while the latter requires expensive hardware and costly ^{3}He. With increasing numbers of clinical MRI magnets >1.5T this thesis presents data investigating whether the advantages of higher magnetic field could be applied in lung imaging. Two different approaches to lung perfusion were examined: a non contrast free breathing technique with respiratory and cardiac gating was compared to breath held Gd-enhanced lung perfusion MR imaging. The two techniques were evaluated at two field strengths 3 Tesla and 1.5 Tesla.

Healthy volunteers were scanned using both a 3 Tesla and a 1.5 Tesla MRI system each with 8 parallel receivers, using a cardiac gated Fast Spin Echo pulse sequence. Acquisition was cardiac triggered, with different time delays incremented to cover the entire cardiac cycle. To reduce motion artifacts acquired k-space data was reconstructed using minimal variance algorithm according to physiological data recorded from respiratory bellows and ECG leads.

Contrast injected (Gd-DTPA-BMA) perfusion measurements were performed using both SPGR and EC-TRICKS pulse sequences. Images were acquired in one breath hold of 30 seconds. Non-contrast ECG gated FSE perfusion images were assessed by measuring percent signal change between images acquired in the systolic and diastolic phases of the cardiac cycle. Gd-based perfusion was done through measurement of time to peak of the bolus arrival and signal enhancement integral. Comparable absolute signal magnitude changes were observed through the entire lung from both methods, although the methods differ temporally.

Despite worsening susceptibility at higher field, a 3T MR scanner can be used for evaluation of lung perfusion. We suggest increased SNR at higher field allows non-contrast based MR perfusion imaging comparable to Gd-based bolus methods. Thus it is possible to perform perfusion imaging in clinical populations, where the use of breath holds is often intolerable. The nature of the FSE-based signal change is likely due to difference in blood flow between systolic and diastolic phases. The contrast based methods offer a significant increase in signal but are compromised by cardiac motion produced artifacts. Although the longitudinal relaxivity of Gd decreases with increasing field (from 4.06±0.3 at 1.5 Tesla to 3.88±0.16 at 3 Tesla) the higher polarization of spins at higher fields allows the use of half dose to produce MRA images that are of comparable quality to full dose at 1.5T.

Acknowledgements

I wish to thank my supervisor professor Michael D. Noseworthy, Ph.D for all his guidance, support and encouragement throughout this project. I also would like to thank my supervisory committee, Dr. Julian Dobranowski, MD, Myrna Dolovich, P.Eng and professor Gerald Moran Ph. D. It is an honor to be guided by such bright people.

There is an incredible number of people who helped me with this project. I would like to thank the entire Diagnostic Imaging Department of St. Joseph's Healthcare. Thank you for taking me in as one of your own, and taking up with me and my experiments. Toni Cormier thank you very much for all your help.

I would like to acknowledge the department of Medical Physics and Applied Radiation Sciences. I could not complete this thesis without their support.

A special thanks goes out to the Dalhousie University Physics class of 2003, my development as a student and a physicist could not have had a better start. Thank you very much for still being there for me.

And of course I would like to thank the most important people in my life, my parents Igor and Galina I couldn't be here without your help. Thank you for all of your sacrifices and your unwavering support. My beautiful and incredible wife Heather I simply don't know how I could do anything without you, thank you for your love, your support and your confidence in me. It keeps me going.

dedicated to my wife...

Table of Contents

List of Figures

List of Tables

List of Notations and Abbreviations

R_1	Longitudinal relaxation constant of a contrast agent
T_1	Longitudinal relaxation parameter
T_2	Transverse relaxation parameter
χ	Magnetic susceptibility
CEMRA	Contrast enhanced magnetic resonance angiography
CNR	Contrast to noise ratio
CT	Computed Tomography
DC	Direct current
ETL	Echo train length
FID	Free induction decay
FOV	Field of view
FSE	Fast spin echo
GE	General Electric
GRE	Gradient recalled echo
Gd-DTPA-BMA	Gadolinium complex of diethylenetriaminepentaacetic acid bismethylamide.
Gd	Gadolinium
IR	Inversion recovery
LV	Levenberg-Marquardt
MIP	Maximum intensity projection
MRA	Magnetic resonance angiography
MRI	Magnetic resonance imaging
MTT	Mean transit time
MVA	Minimal variance algorithm

NEX	Number of excitations
NMR	Nuclear magnetic resonance
PE	Phase encoding
PR	Projection reconstruction
RF	Radio Frequency
ROI	Region of interest
SE	Spin echo
SNR	Signal to noise ratio
SPGR	Spoiled gradient recalled
SoS	Sum of squares
TE	Time to echo
TR	Repetition time
TTP	Time to peak
T	Tesla
bpm	Beats per minute
cc	Cubic centimeter
ml	Milliliter
mM	Millimolar
mm	Millimeter
ms	Milliseconds
s	Second

Chapter 1

Introduction

1.1 Current Methods of Lung Imaging

Lung imaging is currently being done using either invasive methods or methods that involve ionizing radiation. Due to the dose accumulation associated with these procedures, studies that involve the effects of drugs or a treatment follow-up cannot be performed without subjecting patients to high radiation levels or increasing the risk of complication after the procedure. For example, routine clinical imaging of lung parenchyma is performed using chest radiography and computed tomography (CT). CT is currently the gold standard for assessing morphological changes of lung parenchyma with high spatial resolution <1mm. Kauczor et al. 2002 stated that the whole lung can be scanned within 5 seconds, but the use of CT for functional assessment is quite limited.

X-ray pulmonary angiography currently is the most accurate method for detecting perfusion deficiency caused by diseases such as pulmonary embolism. This technique, however, is an invasive procedure: a catheter is inserted, into the vein of the groin, through the chambers of the heart, and into the pulmonary artery leading to the lungs. The contrast medium is then injected into the lung arteries through the catheter, and fluoroscopic X-rays are taken.

A pulmonary ventilation/perfusion scintigraphy is a pair of nuclear scan tests that use inhaled and injected radioisotopes to measure ventilation and perfusion in

all areas of the lungs. The perfusion scintigraphy scan is performed by injecting radioactively labeled albumin into a vein and the patient is then positioned under the arm of a SPECT camera(s). The lungs are scanned to detect the location of the radioactive particles as blood flows through the lungs. The ventilation scintigraphy scan is performed by scanning the lungs while having the person inhale radioactive gas, usually ^{133}Xe. The images are acquired by the same SPECT camera used for perfusion scans. These techniques however are low resolution and Mai et al. (1999) finds them inconclusive in two thirds of cases.

MRI, on the other hand, is a valuable tool that can be safely used on a large percentage of population (people without some types of metallic implants or cardiac pacemakers) as often as the study requires. MR imaging of the lung is difficult not only because of lung morphology but also because of its physiological motion. Recent development of fast MR imaging techniques opened a new window for functional assessment of the lung. The newer generation of MR scanners with higher-strength gradient systems* and echo-planner capability† can control the gradients very accurately and rapidly. The fast MR techniques, are crucial for MR lung imaging, which is a continually growing field. MRI is currently the preferred choice for medical studies since the images can be collected as many times as necessary during the study unlike the methods that use ionizing radiation. To date many different approaches to MR lung imaging have been explored, such as rapid acquisition, functional lung images using hyperoxia, gadodiamide, and hyperpolarized gases. Our intensions were to develop MRI lung imaging methods that could be compatible with many existing clinical systems and be valuable for clinical applications. Human participation in this

*Gradient system controls the plane where the images are being acquired and spatial resolution/localization

†Echo-planar capability enables to scan very rapidly, as fast as sixteen frames per second.

study is necessary since the morphological and physiological properties of the lung cannot be recreated *in vitro*.

We proposed development of MRI methods to gather image data sets of lung lung parenchyma, lung perfusion and lung ventilation using current clinical MRI systems. These techniques could later be used for studying lung diseases such as pulmonary edema, evaluating treatment and drug delivery methods.

There are three major issues one must consider: patient comfort, lung coverage and image quality. Two motions have to be considered and both have to be minimized in order to produce diagnostically valuable data. The respiratory motion artifact can be minimized by either breath holds or gating (e.g. navigator echo technique). Cardiac motion artifact suppression on the other hand can only be achieved via cardiac gating.

Breath holding techniques sometimes are not possible in people with respiratory problems. The subject's motion will impact image quality. Approaches taken in these experiments try to maximize image quality without sacrificing subject comfort. The use of cardiac gating and respiratory gating was applied to eliminate breath holds. In order to reduce scan times acceleration techniques such as fast spin echo (FSE) were used to limit scan time.

Application of Fast Spin Echo pulse sequences to image lungs is not novel. However a clever spin on the technique has been applied by Ogasawara et al. 2004 who successfully imaged physiological changes due to the cardiac cycle, enabling MRI to be a useful modality for imaging lungs.

This thesis expands on work by Ogasawara et al. at 3.0 Tesla, and compares it to dynamically enhanced MR contrast agent lung imaging.

Chapter 2

Physics of Magnetic Resonance Imaging

In this chapter the source of NMR signal is discussed, and how the spectroscopic NMR technique is used as a powerful imaging modality. This include a brief description of the major pulse sequences, MR contrast agents, motion induced MR artifacts and their minimization.

2.1 Spin

Nuclear magnetic resonance is a science of understating the behavior of spin in a static magnetic field and its interactions with surrounding chemical and physical environments. The physical nature of spin however is a complex question that lies in the realm of theoretical physics which, along with other phenomena such as the nature of mass, inertia and gravity are still not very well understood. A good review of current literature on this subjects can be found in Krasnoholovets (2000) work. Uncovering the true nature of spin is not the subject of this thesis. However one point that must be left with the reader is that spin can be regarded as a fundamental property of the particle like mass or charge. The spin I property can be measured with physical instruments, measured in units of $\hbar$ and quantized in multiples of $\frac{1}{2}$. Spin can be positive, negative or zero. Individual unpaired electrons, protons, and neutrons each possess a spin of $\frac{1}{2}$. The spin of the nucleus depends on the number of protons and neutrons it is composed of. If a nucleus has unpaired protons or neutrons it has non-zero spin and is NMR visible.

2.2 Basic NMR Physics

In order to understand NMR principles an understanding of nuclear interactions within a magnetic field is required. First the energy of a proton in a magnetic field is considered, then the classical picture of a proton as a charged spinning particle is presented.

2.2.1 Zeeman Splitting

Once a proton with spin I, is placed in a uniform magnetic field $\vec{B}_a$ it possesses a moment $\vec{\mu}$ and an angular momentum $\hbar\vec{I}$. Magnetic moment and angular momentum quantities are parallel vectors and we may write them as.

$$\vec{\mu} = \gamma\hbar\vec{I} \tag{2.1}$$

with γ as the magnetogyric ratio, a nuclear specific constant present to make the two quantities equal. For the hydrogen nucleus, or the proton, the magnetic moment is tiny 1.4102×10^{-26} JT^{-1}, and magnetogyric ratio is $\frac{\gamma}{2\pi} = 42.575$ MHzT^{-1}.

In the applied magnetic field $\vec{B}_a$, the energy of interaction for a particle with moment $\vec{\mu}$ is

$$E = -\vec{\mu} \cdot \vec{B}_a. \tag{2.2}$$

The applied magnetic field is usually a vector in a single direction $\vec{B}_a = B_o\hat{z}$ then equation 2.2 simplifies to

$$E = -\mu_z \cdot B_o = -\gamma\hbar B_o I_z \tag{2.3}$$

Where the allowed values of spin I_z are $m_I = I, I-1, ..., -I$ which correspond to quantized energy levels $E_I = -m_I\gamma\hbar B_o$. The number of quantized energy levels in

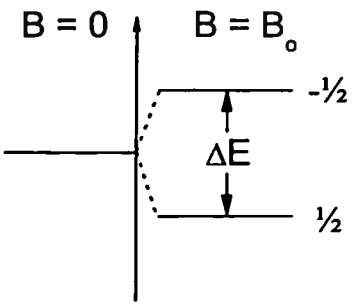

Figure 2.1: Zeeman splitting of energy levels in the presence of the magnetic field B_o. Higher energy state corresponds to those nuclei that are aligned antiparallel to B_o. Energy difference between two states is described by Eq. 2.4.

the magnetic field is $2I + 1$. This means that once a nucleus with non zero spin is placed in a magnetic field it can take on one of $2I + 1$ energy states. This is known as Zeeman splitting and is illustrated in Figure 2.1 for hydrogen nuclei.

The ^1H nucleus in a magnetic field B_o has two possible energy states $m_I = \pm\frac{1}{2}$. The energy difference between the two states in terms of $\hbar\omega_o$ can be calculated from equation 2.3 to be:

$$\Delta E = 2\mu B_o = \gamma\hbar B_o = \hbar\omega_o \tag{2.4}$$

NMR is a quantum mechanical phenomenon and the NMR signal is viewed as the energy measured between the transition of the proton from the higher energy state m_- to the lower m_+. With a sufficiently large magnetic field, ΔE becomes larger then the thermal energy k_bT at room temperature so there are no spontaneous transitions from lower to higher energy state. Most commonly this energy is in the form of electromagnetic radiation. Calorimetric techniques had also been attempted in order to measure magnetic resonance by Gorter (1936) however these methods did not succeed.

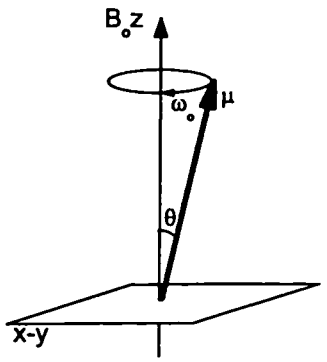

Figure 2.2: Spin placed in magnetic field B_o will start to precess around the field with frequency ω_o.

2.2.2 Nuclear Precession in the Magnetic Field

In a classical picture, rotation of the proton generates a magnetic moment $\vec{\mu}$. In the absence of a magnetic field it is oriented randomly but when placed in a static magnetic field $\vec{B_o}$ it aligns with it, either parallel or anti-parallel. Once aligned it will start to precess about $\vec{B_o}$ as shown in Figure 2.2; this is similar to the spin top precessing in earth's gravitational field. It is readily observed from the rate of change of angular momentum of the system which is equal to the torque $\vec{\tau}$ that acts on the system. Mathematically this is a cross product between the two vectors:

$$\vec{\tau} = \hbar \frac{d\vec{I}}{dt} = \vec{\mu} \times \vec{B_o} \tag{2.5}$$

substituting from Eq. 2.1 this becomes:

$$\frac{d\vec{\mu}}{dt} = \gamma \vec{\mu} \times \vec{B_o}. \tag{2.6}$$

Combining constants from the above equation into a single constant,

$$\omega_o = \gamma B_o \tag{2.7}$$

were ω_o is a natural frequency of the precession also known as Larmor frequency. Solution to the differential equation Eq. 2.6 is the motion of the proton around the magnetic field, written in terms of ω_o as,

$$\mu = \mu_o e^{-i\omega_o t}. \tag{2.8}$$

This precession is field dependent and further it dictates the conditions at which the occurrence of resonance is observed. If proton precess in a magnetic field with frequency ω_o, and is irradiated with electromagnetic radiation field of the same frequency perpendicular to the B_o the two fields couple, energy is absorbed and the spin is tipped.

2.2.3 Bulk Magnetization

NMR experiments are performed on large numbers of spins; usually on the order of Avogadro's number. Then bulk magnetization $\vec{M}$ can be viewed as the sum of all the nuclei moments $\vec{\mu}$ in the unit volume.

$$\vec{M} = \sum_i \vec{M}_i \tag{2.9}$$

It is possible to rewrite the equation of motion Eq. 2.6 using Eq. 2.9

$$\frac{d\vec{M}}{dt} = \gamma \vec{\mu} \times \vec{B}_o \tag{2.10}$$

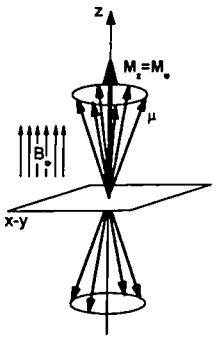

Figure 2.3: In a static magnetic field the population of nuclei aligned with B_o is larger then those that are antiparallel to the field $N_+ > N_-$. This excess of spins with individual magnetic moments μ contribute to the longitudinal magnetization M_o of the entire sample.

In thermal equilibrium at temperature T the magnetization will be along the $\hat{z}$ direction:

$$M_{xy} = 0; M_z = M_o \tag{2.11}$$

where M_{xy} is transverse and M_z is longitudinal magnetization.

If nuclei are placed in a static magnetic field, and are in thermal equilibrium, the population ratio of spins in different energy states is determined by the Boltzman factor for the energy difference of $2\mu B_o$:

$$\frac{N_+}{N_-} = e^{-\frac{2\mu B_o}{k_B T}} \tag{2.12}$$

The magnetization of a system is related to the population difference $N_+ - N_-$ of the spins. The excess of spins aligned with the magnetic field contribute to the total nuclear magnetization of the sample $\vec{M_z} = (N_+ - N_-)\vec{\mu}$ as shown in Figure 2.3.

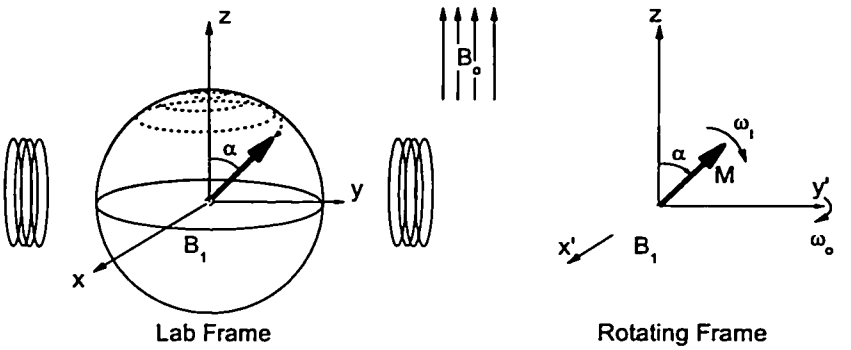

Figure 2.4: Magnetization $\vec{M}_z$ is flipped by angle *alpha* using the field B_1. In the lab frame the motion of the nuclei is described by a nutation around the z axis. In the rotating frame of reference the x-y plane is rotating at ω_o and magnetization this way is seen as tipping along the y'-axis. The rate of tipping is determined by the frequency of the applied field B_1.

2.2.4 NMR Signal Detection

In order to measure the NMR signal, the longitudinal magnetization M_z must be tipped into the transverse x-y plane, which gives rise to transverse magnetization M_{xy}. This is achieved by applying a pulsed electromagnetic field $\vec{B}_1$ applied perpendicular to the main magnetic field $\vec{B}_o$ at the resonant frequency ω_o. In effect the B_1 applies torque onto the nuclear spins which rotates the $\vec{M}$ by a prescribed angle α. The torque is dependent on the strength of the applied field B_1 and the pulse duration. This can be represented on a Bloch sphere in laboratory coordinates, or in rotating frame of reference where the x-y plane rotates at the Larmor frequency (Figure 2.4). The B_1 field is usually generated by a coil that is perpendicular to B_o. That coil can also be used to detect a time varying magnetic field created by transverse magnetization M_{xy} rotating at the Larmor frequency.

The hydrogen nuclei will absorb energy most efficiently at the Larmor frequency which from Eq. 2.7 is magnetic field dependent. Using 1.5T and 3T MRI scanners the corresponding Larmor frequencies are 63.86 MHz and 127.73 MHz respectively.

When a sample is irradiated with RF satisfying the resonance condition in the rotating frame of reference, the $\vec{M}$ will tip away from the z axis at a precessional frequency ω_1 (Figure 2.4) that is dependent on the B_1 RF field as described by:

$$\omega_1 = \gamma B_1 \tag{2.13}$$

The magnetization will continue tipping as long as B_1 is applied. Usually B_1 is applied in pulses of RF energy, tipping $\vec{M}$ by a specific angle α. Because the receiver is located in the x-y plane the signal will be directly related to M_{xy}. The maximum signal is then obtained when a tip angle $\alpha = 90^o$. In order to detect NMR signals most efficiently a series of pulses must be applied (discussed bellow).

Ignoring relaxation (*i.e.* return to equilibrium) effects , the measured signal S(t) from a 3D sample located in a static magnetic field B_o, following a B_1 excitation pulse, with the distribution of transverse magnetization $M_{xy}(\vec{r})$ would be:

$$S(t) = \int_{vol} M_{xy}(\vec{r}) e^{-i\omega_o t} d^3\vec{r}. \tag{2.14}$$

In this case it is not possible to distinguish signals originating from different location of the volume. Instead NMR averages signal from the entire sample.

2.2.5 Longitudinal and Transverse Relaxation

Tipping magnetization, by an angle α gives rise to two magnetization components: M_{xy} transverse and M_z longitudinal magnetization. Following excitation, the transverse component of the magnetization decays away while the longitudinal component returns to its thermal equilibrium state. The magnetization component M_z of the system is approaching the equilibrium magnetization at a rate proportional to the

departure from equilibrium M_o. Mathematically this can be described by differential equation:

$$\frac{dM_z}{dt} = \frac{M_o - M_z}{T_1} \tag{2.15}$$

is a differential equation for T_1 relaxation. The solution to this is:

$$M_z = M_o + (M_z(0) - M_o)e^{-t/T_1}, \tag{2.16}$$

where T_1 is called longitudinal or spin-lattice relaxation time constant and characterizes the return of magnetization to equilibrium along the z direction (Figure 2.5). This relaxation is done predominantly via exchange of energy between the nucleus and surrounding environment. The T_1 values lengthen with increasing field strength, because the amount of energy nuclei have to release, in order to return to equilibrium, increases with B_o. At the atomic level the nuclei are surrounded by randomly fluctuating magnetic fields. These fields result from moving molecules and other nuclei all possessing a magnetic moments. These fluctuating fields tend to enhance the energy exchange between the nuclei and the lattice, shortening T_1. This effect is the basic principle behind MR contrast agents such as Gd-DTPA-BMA.

The behavior of the transverse magnetization component is dominated by the dephasing of individual magnetic moments leading to magnetization loss (incoherence). We can describe this behavior by

$$\frac{dM_{xy}}{dt} = -\frac{M_{xy}}{T_2}, \tag{2.17}$$

which is differential equation describing T_2 relaxation. The solution to this is simply:

$$M_{xy} = M_{xy}(0)e^{-t/T_2}, \tag{2.18}$$

where T_2 is known as the spin-spin or transverse relaxation time constant. The interaction of nuclear dipoles with each other causes some spins to precess faster or slower then others. This brings an even distribution of spins that causes loss of spin coherence and results in decay of transverse magnetization, as shown in Figure 2.5. Transverse relaxation determined by molecular mobility where spins bound to big slow turning macromolecules experience rapid T_2 decay while smaller more mobile spins, exhibit much slower decay. Comparing to longitudinal relaxation, transverse magnetization always decays faster, generally

$$T_2 \leqslant T_1.$$

In addition to T_2 another source of loss of transverse magnetization is B_o inhomogeneities which give rise to a time constant T_2^*. Mathematically expressed as

$$\frac{1}{T_2^*} = \frac{1}{T_2} + \gamma \Delta B_o \tag{2.19}$$

where ΔB_o is the inhomogeneity of external magnetic field ($\gamma\Delta$ B_o is sometimes called $1/T_2'$). In a biological tissue with a nonzero ΔB_o transverse magnetization is largely described by T_2^*. In most cases $T_2^* \leq T_2$ causing shorter free induction decay (FID) and loss of NMR signal. However using special techniques such as spin echo, which is discussed in more detail in section 2.4.2, the signal loss can be recovered.

2.3 Magnetic Resonance Imaging

Magnetic Resonance Imaging (MRI) is an extension of NMR. Historically it was called NMR imaging (or less commonly Zeugmatography), omission of the word "nuclear" has been made by clinicians in order to shed any association with bad publicity

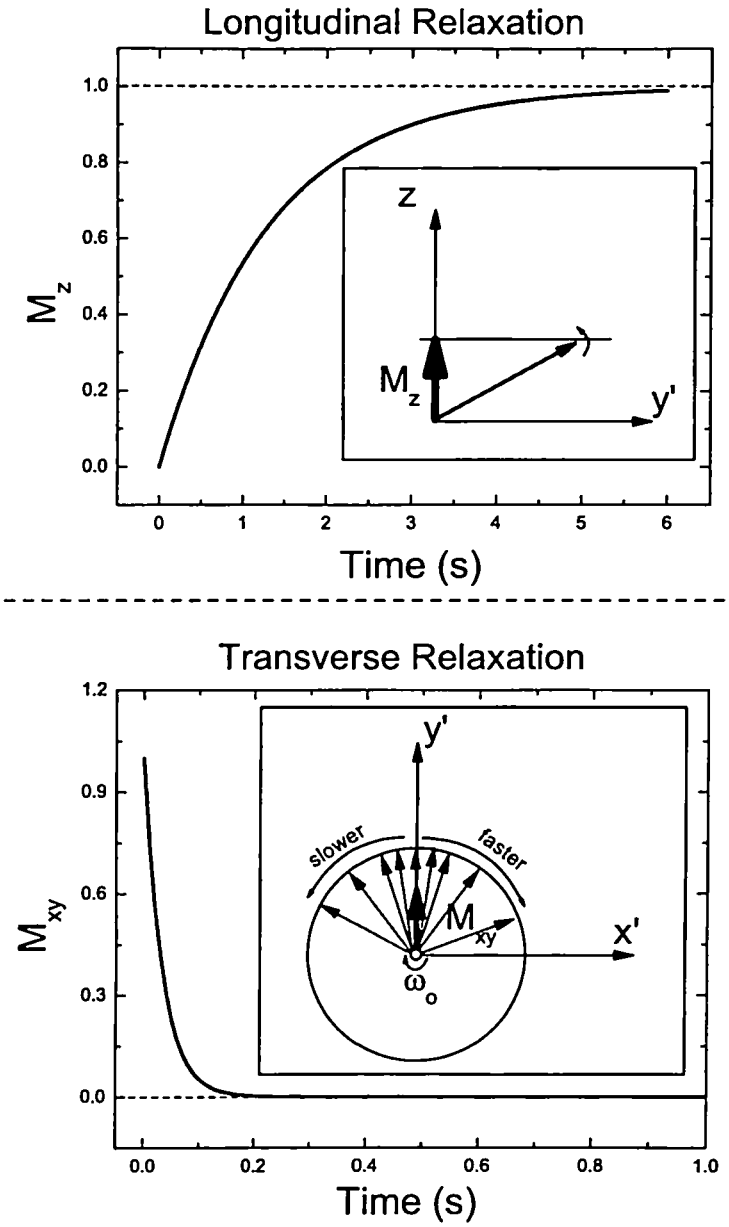

Figure 2.5: Longitudinal relaxation must recover to the initial state along z, as described by Eq. 2.16. The energy during the longitudinal recovery is absorbed by the surrounding lattice. Transverse relaxation occurs due to spin-spin interaction and acts to disperse the distribution of precessional frequency ω_o. Some spins slow down while others precess more rapidly. The end result is loss of spin precessional coherence. Transverse relaxation is governed by Eq. 2.18.

that follows nuclear technology. The purpose of MR imaging is to spatially map and localize the distribution of transverse magnetization in a 3D object. This is achieved through the use three orthogonal magnetic field gradients. By changing the strength and uniformity of B_o 2D or 3D data can be collected that characterize physical properties of a material such as nuclear spins density, and relaxation times T_1, T_2 and T_2^*. This is meant as a basic introduction to imaging for a much more rigorous explanation of the MRI please refer to Haacke et al. (1999) or Bernstein et al. (2004).

2.3.1 Selective Excitation

Selective excitation of spins is one of the most powerful features of MRI as an imaging modality. It is possible to excite only a specific volume of spins and then spatially encode it. Typically this is done through the combined use of magnetic gradient and modulated RF pulse. For example a gradient G_z is superimposed on top of the main magnetic field B_o. This creates a gradient of spins with Larmor frequencies spatially distributed along z axis.

In order to induce resonance in a spins of an axial slice of thickness Δz an RF pulse is designed such that it caries a range of frequencies, and a bandwidth of

$$\Delta\omega = \gamma G_z \Delta z. \tag{2.20}$$

The only spins excited are those matching the frequencies of the applied RF pulse. Those spins residing outside of the RF pulse frequency range will remain unexcited. A summary of this is shown in Figure 2.6.

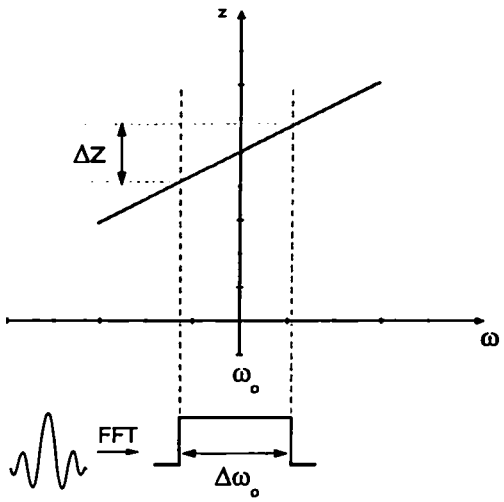

Figure 2.6: Sample with the magnetic gradient G_z distributes the precessional frequencies $\omega(z)$ linearly along z. A Fourier transform of a Sinc pulse is a square function in the frequency domain. Applying Sinc pulse width $\Delta\omega_o$ will excite only those spins that fall within the $\omega(z)$ function. Thus exciting spins only within Δz.

2.3.2 Spatial Encoding

Spatial encoding of a selected slice is done using gradients $\vec{G}$. Varying the magnetic field in the spatial domain, distributes the Larmor frequency of the nuclei as function of their spatial position $\vec{r}$ according to:

$$\omega(\vec{r}) = \omega_o + \gamma\vec{G}\cdot\vec{r} \tag{2.21}$$

By prescribing at specific times, magnitudes, and different time intervals the MR signal S(t) can be spatially encoded. Thus, with the application of gradients, the measured NMR signal can be rewritten from the Eq. 2.14 using the spatially dependent Larmor frequency:

$$S(t) = \int_{vol} M_{xy}(\vec{r}) e^{-i\omega_o t + \gamma \int_0^t \vec{G}(\tau)\cdot\vec{r}d\tau} d^3\vec{r}. \tag{2.22}$$

The above signal equation with spatial encoding parameter $\vec{k}(t)$:

$$\vec{k}(t) = \frac{\gamma}{2\pi} \int_0^t \vec{G}(\tau) d\tau, \tag{2.23}$$

can be further simplified by understanding that the signal S(t) is demodulated. Thus the S(t) can be rewritten without $e^{-i\omega_o t}$ as a function of the spatial encoding parameter $\vec{k}(t)$ as:

$$s(\vec{k}) = \int_{vol} M_{xy}(\vec{r}) e^{-i2\pi \vec{k}\cdot\vec{r}} d^3\vec{r} \tag{2.24}$$

Thus the signal is acquired over time, as the gradients are applied to encode the position of the changing $\vec{k}$ parameter. In a 2D case then gradients G_x and G_y can be applied such that to collect a two dimensional map of the spatial encoding parameters $k_x(t), k_y(t)$ we can rewrite these as:

$$k_x(t) = \frac{\gamma}{2\pi} \int_0^t G_x(\tau) d\tau$$

and,

$$k_y(t) = \frac{\gamma}{2\pi} \int_0^t G_y(\tau) d\tau \tag{2.25}$$

After time=t the collected signal can be represented as a function of k_x and k_y:

$$s(k_x, k_y) = \int_x \int_y M_{xy}(x, y) e^{-i2\pi[k_x x + k_y y]} dx dy \tag{2.26}$$

Therefore, from this equation the magnetization distribution $M_{xy}(x, y)$ can be recovered via fourier transformation.

In general, the Field of View (FOV) associated with other modalities, is directly associated with the area that is imaged, or sampled. In MR, sampling takes place in

the spatial frequency domain. In order to get the image the data is Fourier transformed: this transformation results in an inverse proportional relationship between the sampling rates Δk_x and Δk_y and FOV:

$$FOV_x = \frac{1}{\Delta k_x}, FOV_y = \frac{1}{\Delta k_y} \tag{2.27}$$

The signal(referred to as an "echo", described in the next section) is sampled digitally. A 2D array of $s(k_x, k_y)$ or k-space data is produced by frequency and phase encoding. During frequency encoding a gradient, G_x, is applied during the read out of the echo signal. This fills one line of k-space and resolves one spatial dimension x. To produce a second dimension a phase encoding gradient, G_y,is applied with different strength. The two steps are repeated with varying amplitudes of G_y until all of the desired k-space is acquired (see Figure 2.7). The collected k-space data is digitized into real and imaginary components which are acquired by mixing the signal with $\cos(\omega_o t)$ and $\sin(\omega_o t)$ functions. The resultant real and imaginary k-space is converted to image space using a 2D Fourier transform. Often number of points in k-space is acquired with the dimensions as a function of power of 2 to allow use of the Fast Fourier Transform (FFT) algorithm.

2.4 Gradient Echo and Spin Echo Imaging Techniques

The detected MR signal is usually in the form of what is called a resonant echo. There are two major ways to produce resonant echoes. First gradient echo technique, apply a gradient reversal to refocus spins and collect MR signal. Second the spin echo or Hahn echo, first observed and explained by Erwin Hahn in 1950, uses a 180^o RF pulse to refocus the spins and generate an echo.

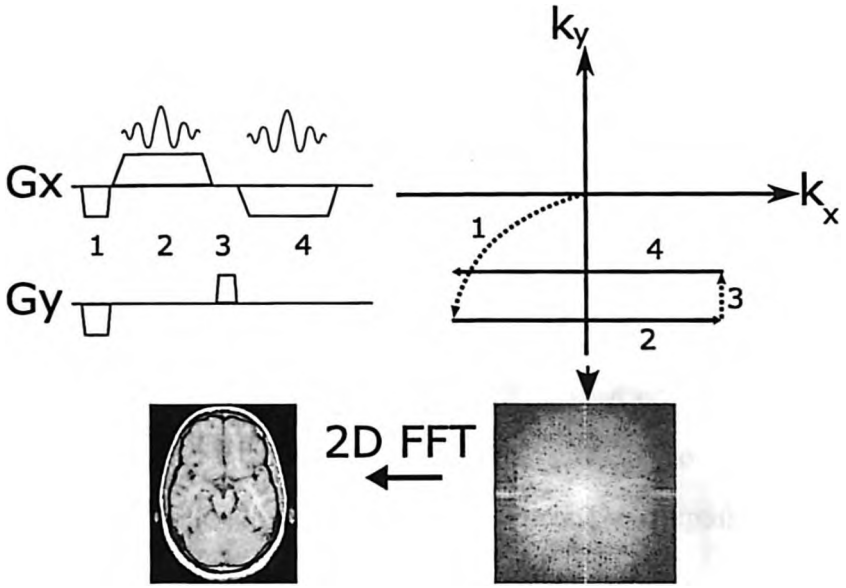

Figure 2.7: By applying G_x and G_y gradients it is possible to acquire 2 dimensional information about the distribution of $M_{xy}(x, y)$. Steps 1 through 4 show the application of gradients and their direct effect of traversing in k-space. Data is recorded only during steps 2 and 4. Data collected in the frequency domain must be reconstructed using a 2D FT algorithm to produce an anatomical image.

2.4.1 Gradient Echo

The gradient echo pulse sequence is primarily used for fast scanning. It requires only a single RF pulse, and then the echo is formed by dephasing and then re-phasing gradients. Gradient echoes are also called gradient-recalled or gradient refocused echoes. An example of the formation of gradient echo is shown in Figure 2.8. Figure 2.9 shows a pulse sequence timing diagram of a Gradient echo (GRE) pulse sequence. First an RF pulse tips the main magnetization vector into the transverse plane by angle α . Then $-G_x$ is applied such that the transverse magnetization M_{xy} will dephase a specified amount. This de-phasing occurs because spins experience different magnetic field, some precess slower while others precess faster. Rapidly switching the gradient polarity to $+G_x$ after time $TE/2$ will cause the spins that precess slower during $-G_x$ to precess faster and *vice versa*. The nuclear spins re-phase and form gradient echo at time $t = TE$. The optimal echo occurs at time TE when the areas

of the negative and positive gradients are equal. The total area of positive gradient $+G_x$ is twice the area of negative gradient $-G_x$. This is necessary to acquire a full line of k-space during frequency encoding.

One important advantage of this technique includes a requirement of only one RF pulse, thus drastically reducing specific absorption rate (SAR) (discussed bellow in Section 2.7). The most important reason for using GRE pulse sequences is acquisition speed. However if an off-resonance condition, $\Delta\omega_o$ exists prior to gradient application, there will be a net phase accumulation at the time of the gradient echo. Further problems with the GRE occurs in the presence of large susceptibility differences between tissues. It is very hard to control the magnetic field experienced by spins in different regions, and with the presence of susceptibility it is almost impossible to refocus all of the spins and produce an efficient echo.

2.4.2 Spin Echo

One of the most fundamental MRI pulse sequences is the spin echo (SE) or Hahn echo sequence. Briefly, it is formed by a 90^o excitation RF pulse followed by 180^o refocusing RF pulse. Conceptually this is demonstrated in Figure 2.10 with pulse sequence timing diagram shown in Figure 2.11. The flip angles for excitation and refocusing are set to 90^o and 180^o respectively. First the excitation pulse tips the magnetization vector into the transverse plain along the y axis. Then spins begin dephasing due to field inhomogeneities. After time $\tau = TE/2$ the amount of total dephasing accumulated to disperse spins is defined by angle ϕ. In order to re-phase spins, a 180^o pulse applied at time τ rotates spins 180^o around the x axis. The spins continue to precess at their slightly different frequencies except that their phases

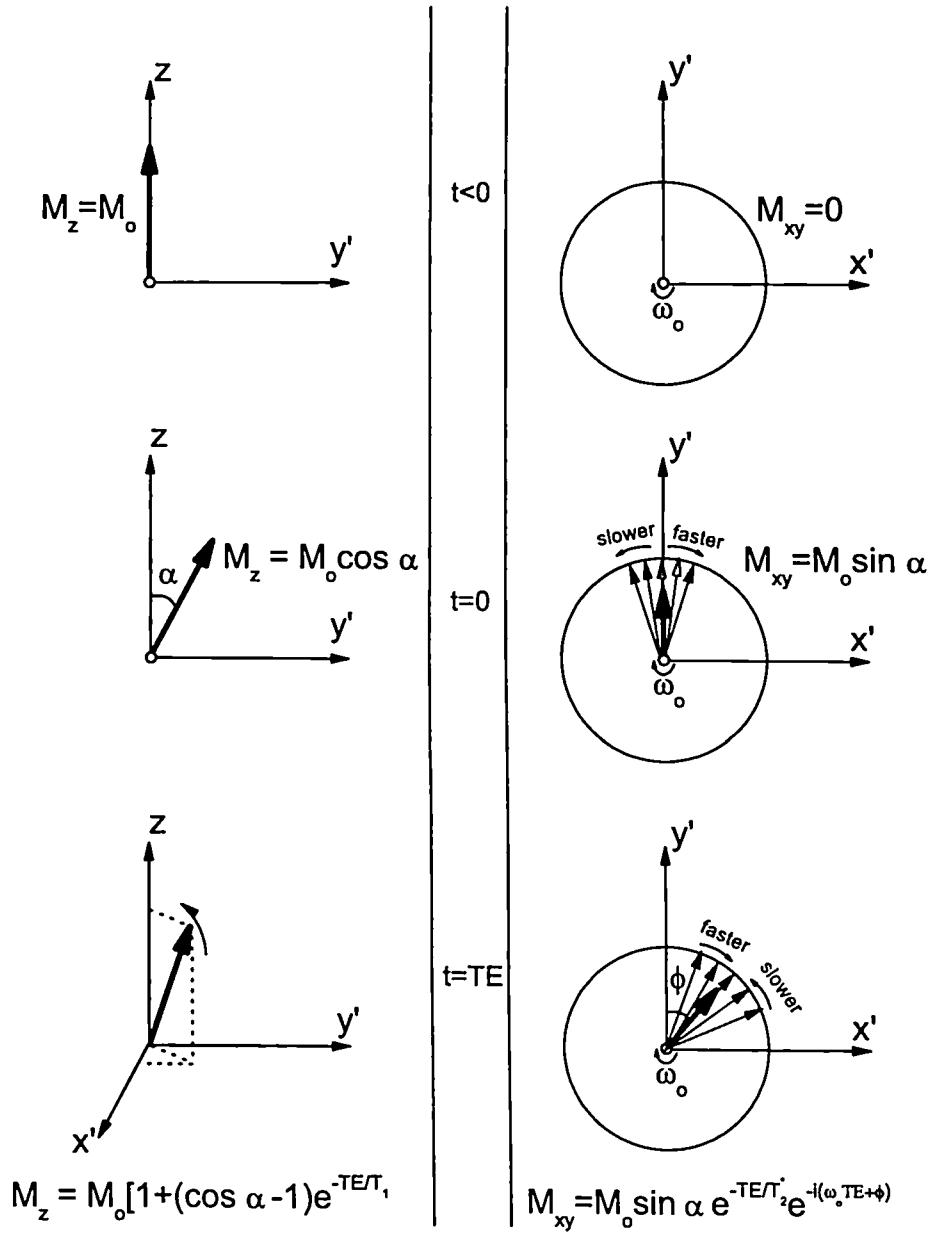

Figure 2.8: At $t < 0$ all of the bulk magnetization is along z. When B_1 is applied on resonance, transverse magnetization M_{xy} is produced along y'. Immediately spins start to dephase because of the applied gradient G_x. Spins that experience higher field, precess faster than those experiencing lower. With gradient polarity switching, spins refocus and produce an echo at time t=TE. However if an off resonance condition occurs a net phase accumulation moving M_{xy} away from y' axis will result.

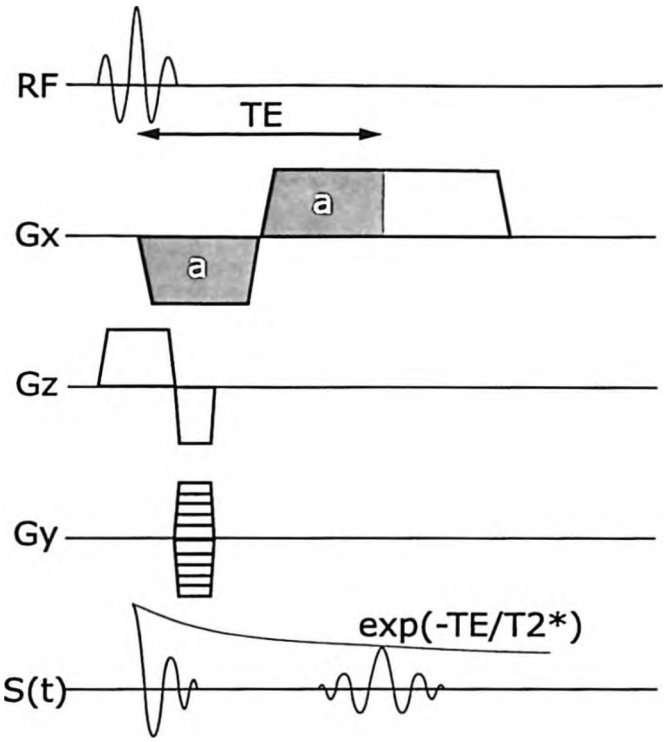

Figure 2.9: Recalled gradient echo pulse sequence timing diagram. Recalled echo is produced by a reversing G_x gradient. When the areas a and b are equal the echo will refocus producing an echo at time TE.

have been negated. Exactly after time $2\tau = TE$ spins have refocused and a spin echo results.

SE is mainly used because of its ability to obtain a specific contrast weighting of images either T_1, T_2 or proton density (Table 2.1). Spin echo is a very robust technique, it is less prone to blurring and ghosting than gradient echo sequences. As well, more importantly, it offers a greater immunity then GRE to artifacts arising from susceptibility differences between tissue interfaces that lead to local magnetic field inhomogeneity. This is because a 180^o RF pulse refocuses the off-resonance effects, leading to less imaging artifacts. The SE signal is weighted by a factor e^{-TE/T_2} while the GRE is weighted by a factor e^{-TE/T_2^*}. Hence SE is a preferred imaging method

Table 2.1: Combinations of TE and TR values and the contrast weighting they generate in spin echo imaging. *(NOTE: Numerical values are shown for B_o = 1.5 Tesla)*

	Short TE ($\leq 20ms$)	Long TE ($\geq 80ms$)
Short TR ($\leq 700ms$)	T_1 weighted	Mixed weighting
Long TR ($\geq 2000ms$)	Proton-Density weighted	T_2 weighted

for lungs, where field inhomogeneity caused by numerous tissue air interfaces cause T_2^* to be so short that it becomes a challenge to image.

2.4.3 Inversion Recovery The inversion recovery pulse sequence is a modified spin echo pulse sequence that offers greater T_1 weighting and the ability to eliminate spin population due to T_1. Application of an extra 180° inversion pulse before the 90° excitation, creates magnetization $-M_o$ in the negative z-axis (Figure 2.12). Time between the inversion RF pulse and the 90° excitation RF pulse is called the inversion time or TI. Varying TI causes a suppression of signal from various tissues and is the basis behind short tau inversion recovery (STIR) for fat suppression and fluid attenuation inversion recovery (FLAIR) for H_2O suppression. As we know according to Bloch's relationship for longitudinal relaxation (Eq. 2.15) the signal recovers exponentially according to parameter T_1 which is tissue dependent. If an excitation pulse is applied when the longitudinal magnetization for that tissue crosses the null point, signal from that tissue will be eliminated.

Advantages of the IR pulse sequence is that it can offer better T_1 weighted contrast and better signal to noise ratio then a conventional SE pulse sequence. Measurements of T_1 are usually performed using IR pulse sequence, by varying inversion time TI a longitudinal magnetization recovery graph can be produced (Figure 2.13).

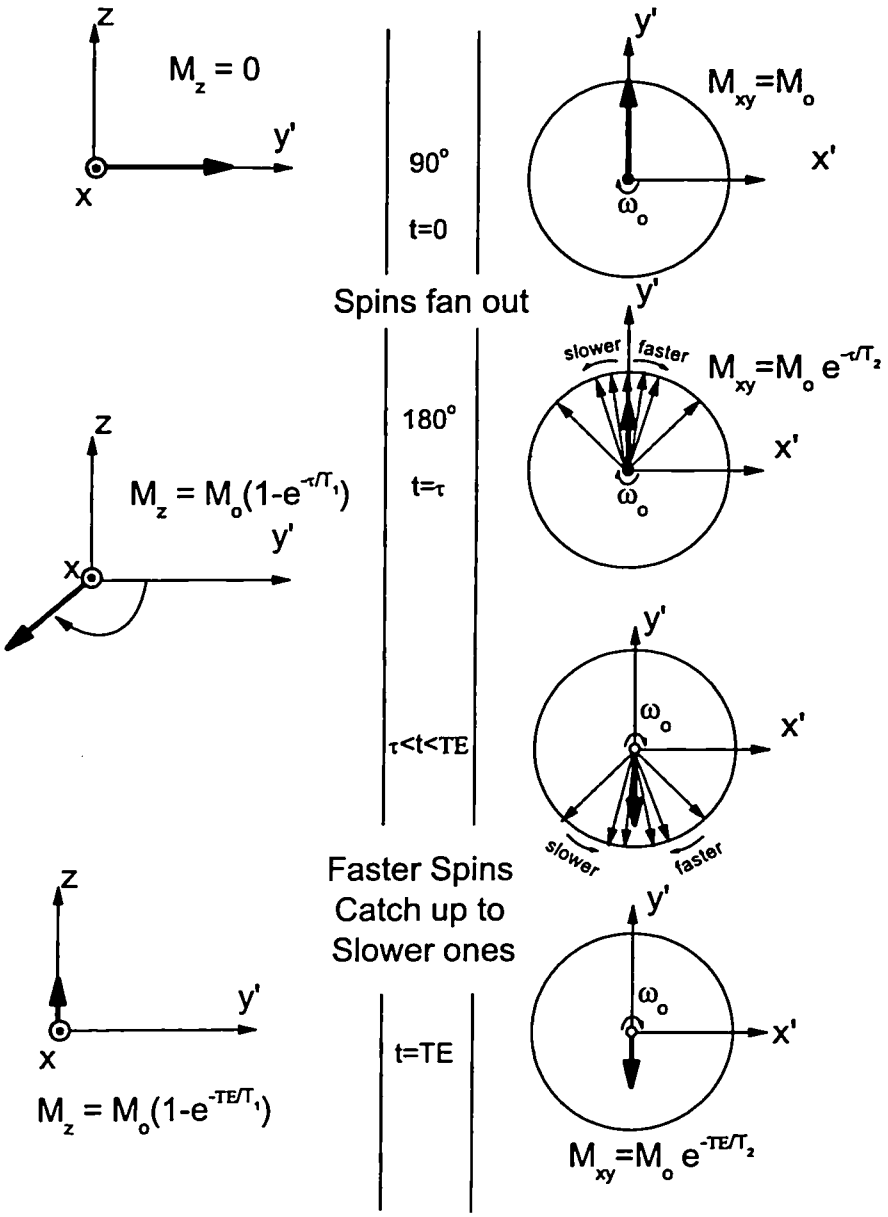

Figure 2.10: At t=0 a 90° slice selective RF pulse is applied tipping magnetization M_o onto the y' axis. Spins then begin to "fan out" at a rate which is governed by T_2. At time=τ a 180° refocusing pulse is applied, causing magnetization M_{xy} to flip about the x' axis onto the -y' axis. Now the spins that were precessing faster are located behind the main magnetization. At time $TE = 2\tau$ the spins rephase and produce a spin echo.

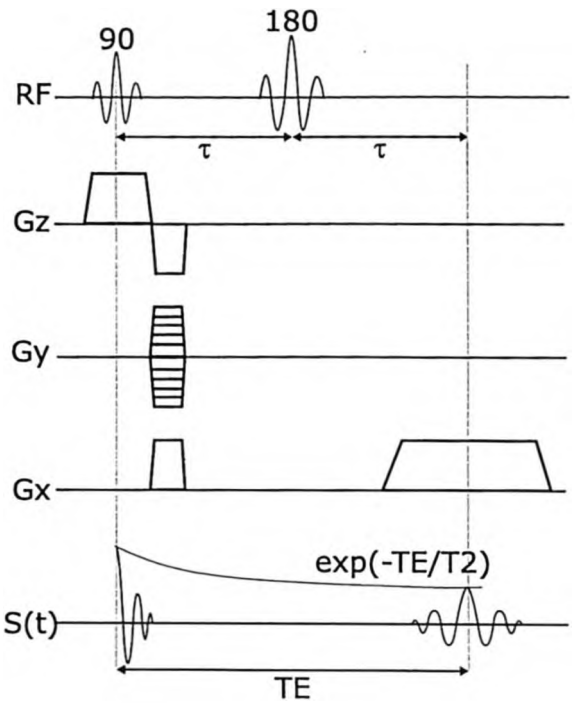

Figure 2.11: Spin echo pulse sequence timing diagram. An echo is produced by a 180^o refocusing pulse. The echo forms at time 2τ.

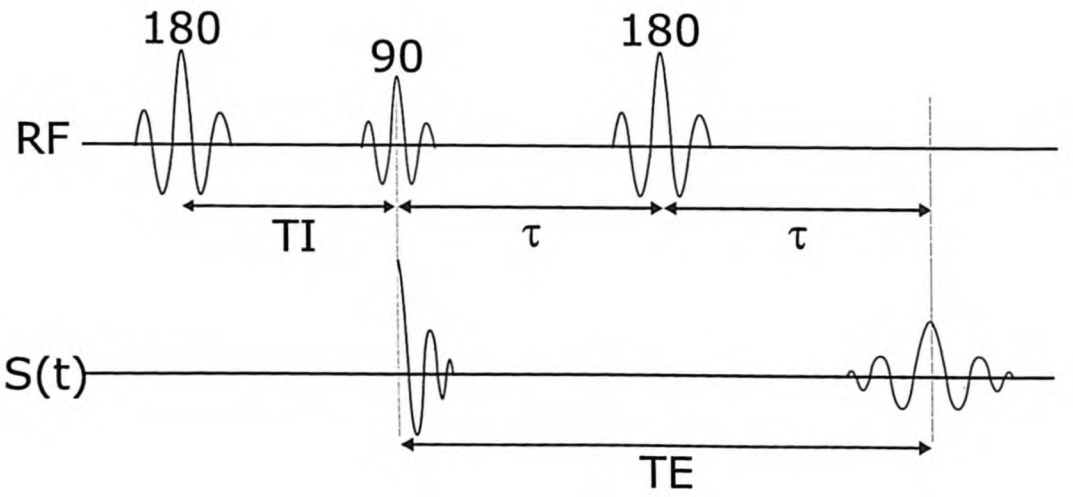

Figure 2.12: Inversion recovery is achieved by applying an inverting 180^o pulse before the conventional spin echo experiment. Magnetization has to recover from $-M_o$ to the equilibrium state.

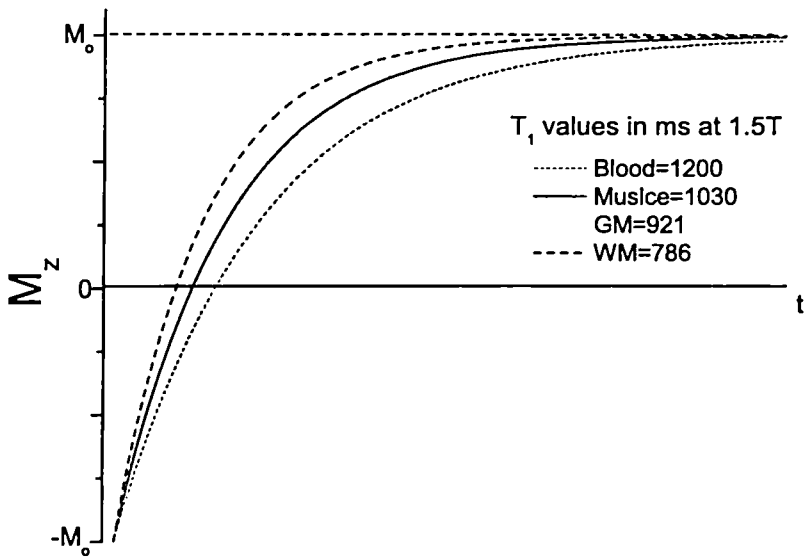

Figure 2.13: Inversion recovery pulse sequence used to measure T_1 values of different tissues by varying time TI.

2.5 Fast Spin Echo and other Rapid Pulse Sequences

2.5.1 FSE Family of Pulses

The Fast Spin Echo (FSE) family of pulse sequences, are modifications of spin echo concepts, (described in the section 2.4.2). The FSE sequences typically involve multiple 180^o RF pulses allowing multiple lines of k-space to be acquired per repetition time (TR).

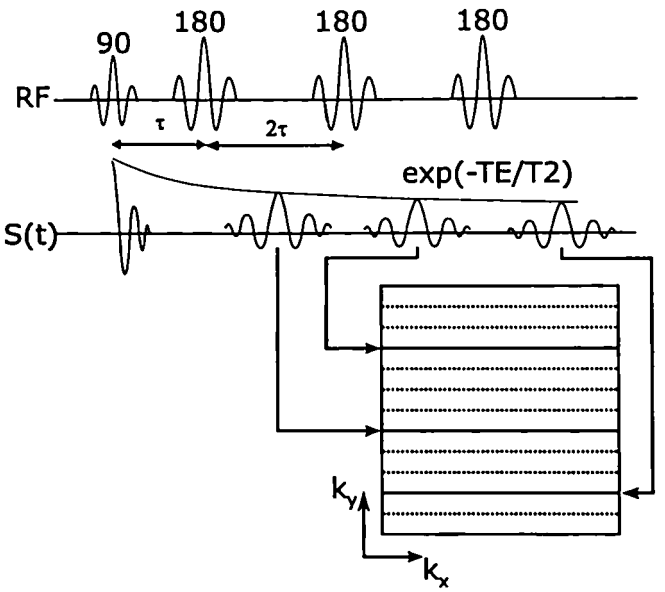

Figure 2.14: A fast spin echo pulse sequence (FSE) uses a number of 180° refocusing pulses to produce multiple echoes. The gradients are applied such that each echo fills a single line of k-space. Here 3 echoes are sampled and 3 lines of k-space are acquired in one TR.

In conventional spin echo imaging a 180° refocusing RF pulse is applied and the echo is formed within one TR period. For example a matrix size 256x256 with a TR of 1 second will take 256 seconds to collect. Acquisition of one echo depends on the bandwidth and matrix size: typically a 256 point echo with 16 kHz bandwidth is acquired in 8 ms. A considerable portion of the signal still exists after the acquisition as long as M_{xy} is present. This fact is exploited in accelerated pulse sequences. Accelerating is possible by forming multiple echoes with multiple 180° pulses separated by time 2τ. Acquiring multiple echoes and filling multiple lines of k-space is shown in Figure 2.14.

On a GE Healthcare® MR scanner the echo train length (ETL) is an FSE acceleration factor which indicates the number of echoes collected and number of k-space lines filled. ETL directly determines the scan-time reduction or the acceleration compared to a spin echo imaging experiment. By setting ETL equal to the imaging matrix it is

possible to fill the entire k-space in a single shot. This pulse sequence is called Single Shot Fast Spin Echo (SSFSE). Accelerated pulse sequences are extremely useful in clinical settings where the images have to often be acquired rapidly.

Rapid acquisition comes with the cost of image artifacts such as, blurring and ghosting along the phase encoding direction. The main cause of the blurring artifact is the multiple acquisition of echoes along the T_2 decay curve. Echoes that are collected at the end of the T_2 curve contribute smaller signal than those that were acquired at the beginning. This makes k-space acquired unevenly causing blurring artifacts in the phase direction. Ghosting is the term to describe an appearance of a weaker intensity image appearing just slightly over the image of interest. This artifact is caused by phase errors propagating and building up through the ETL. Minimizing ETL and averaging the signal by increasing number of excitations (NEX) resolves most of the problems associated with this mode of fast imaging.

Direct Current (DC) offset (baseline) can be present in the receiver hardware, or caused by eddy currents formed by rapid switching of gradients and will affect the collected k-space, by appearing as a bright spot in the middle of the image. In FSE pulse sequences phase cycling the 90^o excitation pulse by π every NEX is used to prevent such DC offset artifact.

2.5.2 Fast Spoiled Gradient Echo and EC-TRICKS

The spoiled gradient echo pulse sequence uses phase cycling of the RF pulses to enhance T_1 weighting in images. RF excitation pulses are phase cycled according to a predetermined schedule, such that at the end of every TR interval the magnetization M_{xy} is nearly zero. The Fast SPoiled Gradient Echo (FSPGR) technique is similar to the the ones described in the section above, except echoes are recalled using gradients.

Maximization of signal from the SPGR type pulse sequence can be performed by setting the flip angle to an Ernst angle α_E given by,

$$\alpha_E = \arccos(e^{-TR/T1}) \tag{2.28}$$

Elliptical Centric Time Resolved Imaging of Contrast KineticS (EC-TRICKS) is a type of keyhole imaging method used to improve temporal resolution of contrast enhanced scans. The basic principle behind EC-TRICKS is the division of k-space into equal areas that are temporally sampled in a predetermined cyclic pattern. This sampling scheme ensures the center of k-space is sampled most frequently. The center of k-space contains most of the information about image contrast, low spatial frequency, and SNR hence it is sampled more frequently.

Prior to the injection of contrast, all of k-space is sampled once and is reconstructed as a "mask". The temporal data of period T is sampled, after the injection of contrast, in a scheme such that center of k-space is sampled every 2T interavals and the rest of k-space is sampled in a fashion shown in Figure 2.15. Temporal data with the contrast agent is then subtracted from the mask to produce contrast enhanced magnetic resonance angiography (CEMRA) maximum intensity projection (MIP) images.

2.6 Contrast Enhanced Magnetic Resonance Angiography (CEMRA)

Angiography is a technique used to image blood vessels within the human body using a contrast agent. In CEMRA a bolus injection of a contrast agent is used to change blood T_1 relaxation and produce contrast. In order to suppress T_1 relaxation the injected contrast agent must be paramagnetic. One of the most commonly used

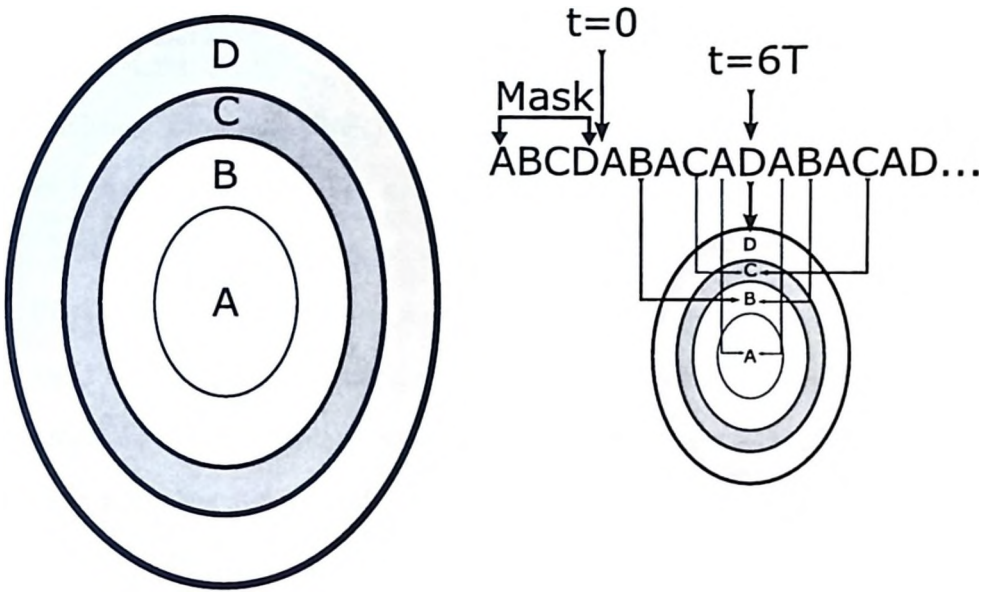

Figure 2.15: EC-TRICKS breaks downs k-space into 4 sections, ABCD. Mask is acquired first before the injection of contrast agent. Center section A contains most of the spatial information hence sampled more frequently. Then images are reconstructed for each time period T by interpolating data from other sections of k-space. Interpolation is done using two points of same section before and after the period of interest.

agents is an ionized ion of a rare earth metal Gd^{3+}. By itself Gd^{3+} is toxic however chelation with diethylenetriaminepentaacetic acid (DTPA) or diethylenetriaminepentaacetic acid bismethylamide (DTPA-BMA) results in extremely high molecular stability with almost zero toxicity.

The procedure of CEMRA involves injection of a volume of contrast agent into the antecubital vein using a power injector at a defined injection velocity. The more concentrated the bolus the more contrast between pre and post signal can be seen. Because the concentration of Gd disperses as soon as it is injected, imaging must be done on the first pass of the agent through the system. The main goal of CEMRA is to acquire images of anatomical interest during the highest concentration of bolus present within the blood vessels. This produces the highest contrast difference between vessels and tissue.

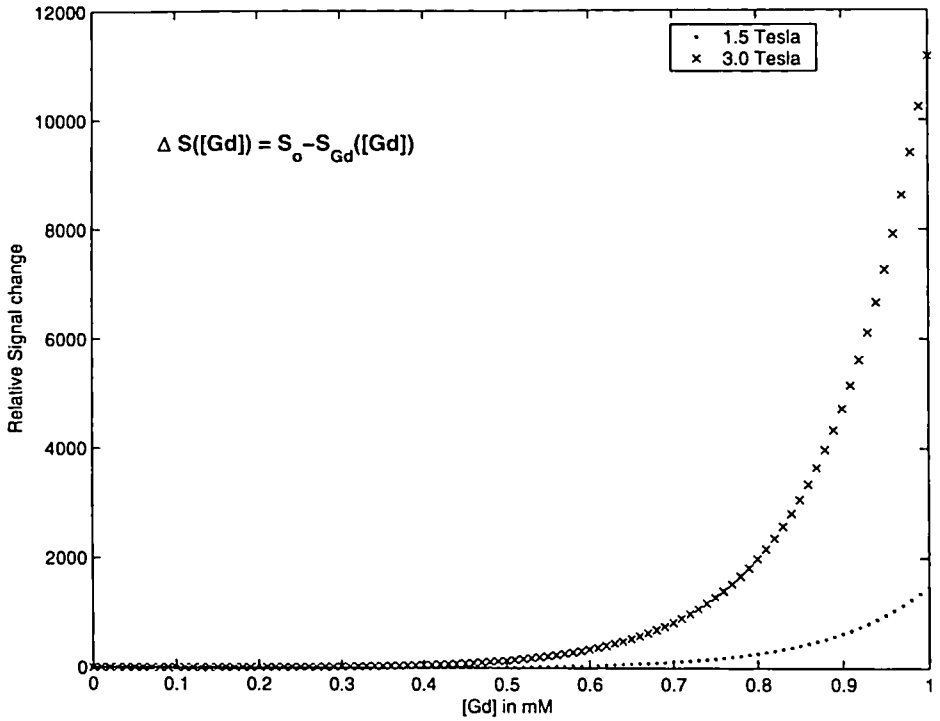

Figure 2.16: A smaller concentration of contrast agent at 3.0 T produces the same signal change as larger concentration of that same agent using 1.5 T. Therefore in order to produce similar signal enhancement on 3.0 T less contrast agent is required.

The T_1 reduction of blood can be expressed in terms of the concentration of [Gd] and agent efficiency of longitudinal relaxivity, R_1:

$$\frac{1}{T_1} = \frac{1}{T_{1o}} + R_1 \times [Gd] \tag{2.29}$$

where T_{1o} is original longitudinal relaxation time. The contrast between the tissue and the blood is also dependent on the proton density that contributes to main M_o magnetization. Hence the magnetic field difference will change the amount of [Gd] needed to produce the same signal difference (Figure 2.16).

2.7 Specific Absorption Rate

Specific absorption rate (SAR) is defined as the total RF energy absorbed by the body over the exposure time per unit mass, and is measured in watts per kilogram (W/kg). The SAR limits have previously been defined by medical regulatory bodies such as FDA. However these limits still vary from country to country. In clinical MR imaging on 1.5T scanners the amount of RF energy absorbed by patients is typically lower than set limits. However at higher magnetic fields, such as 3T, SAR becomes a serious issue when certain pulse sequence parameters are used. Depositing 4.184 W of RF energy in one second into 1 g of water will increase the temperature of that water by $1°C$.

The spatial energy deposition is not concentrated in the imaging area instead it is distributed over the entire volume that RF coil can transmit to. This makes SAR measurements relatively difficult to perform and requires specialized equipment and conditions. The calibration of the MRI scanner is done experimentally using one of three basic techniques for measuring SARs. One is to measure the electric field inside the body and knowing the conductivity of the material calculate SAR. A second basic technique for measuring SAR is to measure the temperature change due to the heat produced by the radiation, and calculate the SAR from that. A third technique is to calculate absorbed power as the difference between incident power and scattered power.

To simplify things theoretically it is possible to estimate SAR based on a scaling relationship. It is known that the energy absorption from radio waves increases with frequency. In clinical field strengths (*i.e.* $0.2 < B_o < 3.0$T) SAR increases with the square of the Larmor frequency, and hence B_o. It is also proportional to the square of B_1 amplitude, equivalently written as the flip angle α. And is also linearly

proportional to the RF bandwidth Δf. In summary we can write down the simplified SAR relationship as:

$$SAR \propto B_o^2 \alpha^2 \Delta f \tag{2.30}$$

The link between MR pulse sequence parameters and SAR is well understood. With each delivered RF pulse some percentage of its energy will be deposited in the tissue. Monitoring how often and how much RF energy is being transmitted is one of the basic concepts behind SAR management and is a built in feature in all clinical scanners. For a more complete explanation of SAR and its effects see Durney et al. (1986), Bottomley et al. (1985) and Haacke et al. (1999, Chapter 27, Section 4.5)

2.8 MRI of the Lung

The behavior of the NMR signal in the lung is peculiar. First a fundamental problem arises because lungs are a porous tissue, most of which is air space. Secondly, NMR requires protons to generate signal. Lungs contain only about 0.3 grams of tissue per cubic centimeter. Hence the NMR signal intensity for lung can be expected to be a small fraction of that in other tissues, when based on proton density. A third problem results from lung containing a plethora of air tissue interfaces. Figure 2.17 shows a porous tissue sample, where the magnetic field lines deviate from the main field B_o. This makes it virtually impossible to position a porous sample within a homogenous and uniform magnetic field. Therefore spins in porous tissue will not experience same magnetic field and will be at different Larmor frequencies ω_o. The spatial distribution of magnetic field B(x,y)in porous media with susceptibility map $\chi(x, y)$ can be written down as:

$$B(x, y) = B_o(1 + \chi(x, y)). \tag{2.31}$$

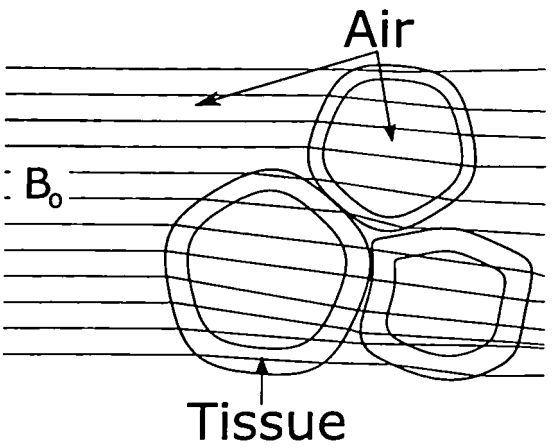

Figure 2.17: Magnetic field lines in the presence of air tissue interfaces. Magnetic field lines change direction due to the change in difference of magnetic susceptibility (χ) between air and tissue.

A distributed magnetic field strength in the lung results in many local gradients that act to dephase and shorten T_2^*. This makes lung MR imaging with GRE type pulse sequences difficult since gradients can not perfectly refocus the spins resulting in rapid signal loss. Instead spin echo pulse sequences, through application of 180° refocusing RF pulses, are used to refocus the spins (dependent on RF coil design). However the ability to perform rapid imaging with this approach is lost, and techniques to improve speed are required.

A further problem to lung MRI lies within complex physiological motion. Two main sources of motion are present: respiratory and cardiac. Respiratory motion within lungs blurs vascular and pulmonary structures, making localization of small defects very difficult. Another more serious contribution of motion is ghosting artifacts appearing in the phase encode direction. Respiratory motion artifacts, which originate from surrounding lungs structures propagate through the entire lung image, while cardiac motion ghosting localizes predominately above and below the heart, Figure 2.18 even if ghost intensity is relatively weak compared to the original structures, the result overwhelms the lung NMR signal making tissue under the ghost

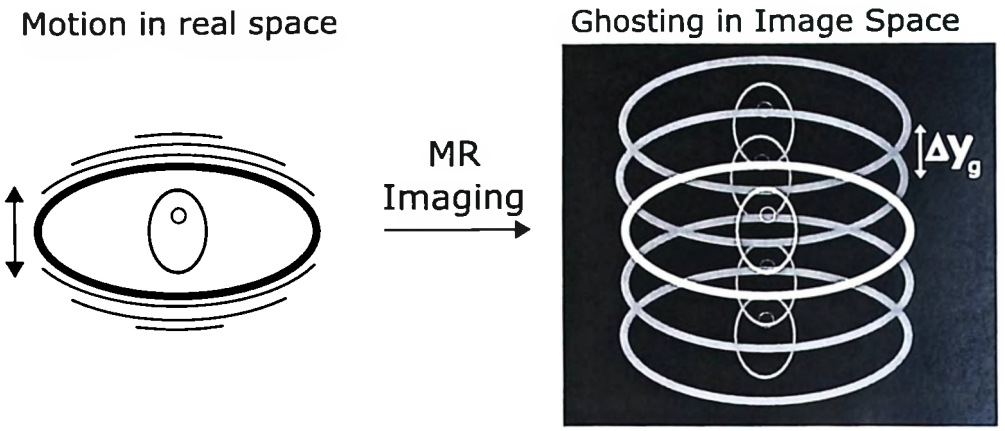

Figure 2.18: Translation of motion into ghost formation in image space. Phase encoding direction is in the direction of ghosting.

completely undiagnosable. Separation of ghosts in the image space Δy_g is modeled by Wood et al. 1988 as:

$$\Delta y_g = \frac{L_y \, NEX \, TR}{T_{m,a}} \tag{2.32}$$

where L_y is the FOV along the phase encode direction, NEX is number of signal averages, TR scan repetition time and $T_{m,a}$ is the apparent motion period. In order to suppress ghosting two strategies can be employed. Either increase the spacing between ghosts farther than the anatomy or try to minimize it such that $\Delta y_g \ll 0$. The simplest way to remove motion is through use of gating, such that $T_{m,a}$ approaches infinity as no modulation to k-space due to motion will occur. Alternatively acquiring critical parts of k-space (center lines) during periods of relatively little motion will reduce motion related contamination.

Two methods often used for gating are retrospective and prospective gating. In prospective gating data is acquired only when the physiological motion is within predefined acceptance window. Retrospective gating, on the other hand, reconstructs over sampled data, according to the physiological motion (Bernstein et al. 2004,

Chapter 12). Prospective gating has been found to produce superior image quality over the retrospective gating images (Du et al. 2001).

Imaging human lungs is thus a challenge. With the above considerations in mind the approach to MR lung imaging must produce diagnostically viable information, and it *must* be practical.

Chapter 3

Literature Survey of Previous Work

3.1 Magnetic Resonance Proton Based Lung Imaging

3.1.1 Effects of Morphology and Physiology of the Lung on NMR signal

Nuclear magnetic resonance (NMR) behavior of the lung is quite peculiar. Unlike other organs in the body, lung Magnetic Resonance Imaging (MRI) is quite challenging. On currently used medical scans, lungs appear dark on MR images and are useless for clinical diagnosis. This fact reflects unusual morphological and physiological properties of lungs.

For the purpose of understanding lung MR signal, we can structurally subdivide lungs into two portions (this is a gross oversimplification of lung structure and function). For complete morphology and physiology description see Albertine (1996).

1. The parenchymal (or respiratory) portion. This consists of a large number of tissue-air interfaces created by approximately 300 million alveoli, measuring 200-300 microns in diameter. Alveolar clusters, are attached to the alveolar ducts and in turn to the respiratory bronchioles

2. The non parenchymal portion. This is made up of pulmonary vessels, which perfuse all of the lung, conducting airways and other non respiratory structures.

During mechanical ventilation parenchymal structures (alveoli) inflate or deflate thus supplying fresh oxygen to the location of respiratory gas exchange in lungs, which occurs between the alveolar spaces and the pulmonary capillaries. Since oxygen (O_2) diffusion is impeded due to low solubility of oxygen in water, (0.3 ml/L $\times$ Hg Pa_{O2} which is 20 times smaller then the solubility of carbon dioxide in water 0.7 ml/L $\times$ Hg Pa_{O2}), large numbers of alveoli provide huge surface area for diffusion $\backsim$50-70 m^2. In a resting state, 5 liters of blood pases through the lungs per minute. During the same time the heart located adjacent to the lungs beats roughly 50-80 times, while lungs themselves have been inflated and deflated 6 to 8 times. All these physiological processes hinder MR imaging and thus need to be overcome for lung MRI.

The air, alveolar tissue, intra and extra cellular fluids all possess different magnetic permeability, with alveoli being the highest. Thus in the region of air-tissue interfaces internal magnetic field inhomogeneity in the lung predominates. Principally the magnetic field will be perturbed in the regions nearest to the air-tissue interface. Additionally, distortion of the magnetic field is angularly dependent, i.e. susceptibility is higher near the interfaces oriented parallel to the field, and less so in the regions were the interface is oriented perpendicular to the magnetic field. The result is signal loss and image blurring. Other factors such as relatively low proton density, signal loss due to cardiac and respiratory motion, pulmonary blood flow and molecular diffusion, make lung imaging additionally challenging.

NMR signal from the inflated lung, unlike any other organ in a body, decays very rapidly. A number of experiments showed signal from lungs resembles that of foam or sponge. Durney et al. (1996) and collaborators (Cutillo et al.; Case et al.; Ailion et al.) have been modeling such behavior of lungs and have contributed an enormous amount of important work in understanding the NMR signal from healthy and diseased lungs. Modeling lung NMR signal on the basis of the thin walled water

structures surrounded by air. Durney et al. (1996) and later Cutillo and Ailion (1999) have been able to mathematically model the expected NMR signal in healthy lung and a lung that suffers from pulmonary disease.

Durney et al. (1996) modeled lungs as simplified structures made up of air and a water shell, similar to soap bubbles, 5 lung models currently exist: (spherical-cell/foam, cubical-cell/foam and a Wigner-Seitz model consisting of polyhedral air cells). These models were used to simulate NMR signal from the lungs by considering the susceptibility effects on the inflation (air content) and the orientation of interface with respect to the magnetic field. The simulated free induction decay (FID) signal from the lungs with differing inflation (0-70%) showed dramatic decrease in signal intensity even after a small amount of air was present in the lung tissue. This result has been confirmed on both sponge models and excised animal lungs. Also by simulating the alveolar flooding that occurs during pulmonary edema the authors were able to model NMR signal in the diseased lung.

3.1.2 Imaging Lung Parenchyma; Opportunities

A number of techniques have been proposed that, with current advances in MR hardware sample the lung MR signal before it decays. One approach is to acquire signal from the lung as fast as possible, dramatically decreasing the probability of image blurring due to physiological and respiratory motion. This method requires a high speed accurate gradient system and a few modifications to the way images are acquired. One such technique described by Alsop et al. (1995) and Cutillo and Ailion (1999) uses sub-millisecond asymmetric echo sampling using a fast gradient system, with a switching time of 150-μs from zero to a maximum value of 23 mT/m, which are much stronger and faster compared to typical gradients (see Table 4.1). These

fast gradients are necessary in order to use ultra short echo times on order of lung T_2 and T_2^* [$T_2^* \approx 1.4$ms and $T_1 \approx 1440$ ms on a 1.5 T system].

Imaging objects with ultra short T_2^* is desirable in many medical and non-medical fields. A number of pulse sequences and techniques have been evaluated and applied in lung MR imaging e.g. gradient echo, spin echo, and projection reconstruction (PR) methods (Alsop et al. 1995; Cutillo and Ailion 1999; Bergin et al. 1991).

Gradient echo pulse sequence optimized for short echo times (sub-millisecond) works well imaging lung parenchyma, although fast and strong gradients are absolutely necessary for this technique. Utilizing small tip angle RF pulses, strong gradients are able to easily refocus the spins. Unfortunately this technique suffers from chemical shift artifacts and image blurring due to asymmetrical image acquisition. Combined with cardiac gating this might be a very promising technique especially with the use of torso phased array coils (Alsop et al. 1995). Recent reports by the same group Hatabu et al. (1999) showed much better visualization of lung parenchyma, using a similar but improved pulse sequence. The advantage of phased array multicoils however were still not utilized (Hatabu et al. 1999).

The asymmetric-echo pulse sequence with a short TE=2.8 ms has been reported and used in imaging heart vasculature by Richardson et al. (1994). This sequence was found to be less attractive for investigation of cardiac flow irregularities then originally thought causing the signal loss due to flow less pronounced. The results however were promising for detection of pulmonary emboli, due to the increased signal from the pulmonary vessels and reduced flow artifact. Unfortunately lung parenchyma was not visualized because of longer echo times.

Projection reconstruction methods have been investigated by Bergin et al. (1991). Their approach did not use phase encoding or pulse refocusing, and demonstrated sig-

nificantly shorter echo times. The gradients and a section-selective excitation pulse used in such a way as to allow center of k-space to be collected first. Thus PR techniques appear very promising in lung imaging. By using echo times as short as 50 microseconds, on an excised inflated lung (both normal and pathologic) specimens, Bergin et al. (1991) showed that signal intensity from lung parenchyma and visibility of pulmonary structures were superior on images obtained with the projection reconstruction technique compared with spin-echo images. Further optimization of MR signal frequencies for image reconstruction were performed by either using susceptibility correction or using a postprocessing algorithm to select frequencies for minimal image blurring (Bergin et al. 1992). However projection reconstruction has drawbacks. For example PR technique is very susceptible to chemical shift and even slight frequency offsets. During reconstruction frequency shifts in back PR result in blurring of the image over a considerable region, unlike the fast Fourier transformation, which shifts the location of offset signals (Alsop et al. 1995).

Another technique suggested by McKinnon (1993) for imaging tissues with short T_2 is to use self refocusing RF pulses. Self-refocusing slice selective radio frequency pulses could potentially be used to reduce imaging times in rapid gradient-echo sequences by about 20%, but at the expense of greatly increased RF power requirements. As this is over a considerable area (thorax) SAR limits would restrict the success of this method.

Knight-Scott et al. (2001) have reported imaging lung parenchyma using cardiac gated Single Shot Fast Spin Echo SSFSE (Half Fourier Single Shot Turbo Spin Echo HASTE). By looking at the changes in signal due to the cardiac cycle they came to the conclusion that the imaging should be completed after systole but before rapid filling of the ventricles. The TR in the experiment was 324 ms and the authors concluded that most of the center of k-space was acquired in the beginning of the

cardiac cycle without diastolic related contamination. In addition, the same group noted lung parenchyma signal from a spin echo based sequence with an inter-echo time of 4.5 ms, was very poor compared to gradient echo methods.

Other types of lung parenchyma imaging include, inversion recovery techniques. Jakob et al. (2001) suggested a use of one inversion pulse (IR), and then multiple Spoiled Gradient Echo SPGR (Fast Low Angle Shot FLASH) acquisitions at different intervals after an IR pulse allowing lung T_1 mapping within a single breath hold. Another inversion recovery technique described by Mai et al. (1999) uses two IR pulses in order to suppress signal from muscle and fat simultaneously. It is possible to change the relaxation times by the use of a contrast agent such as O_2. This has been applied to change the signal (i.e. shorten T_1) of lung parenchyma. The lungs are scanned pre and during 100% O_2 delivery. The images are then subtracted leaving signal that is expected to come purely from the lungs. Unfortunately this method is very sensitive to lung movement and now mostly used for lung ventilation studies (Muller et al. 2002; Muller et al. 2001).

Another recently developed technique for imaging objects with extremely short $T_2^* \leq 1ms$ is a single point imaging technique Single Point Ramped Imaging with T_1 Enhancement (SPRITE) (Halse et al. 2003; Halse et al. 2004). The only imaging requirement for SPRITE sequence is that T_2^* be long enough for phase encoding. This technique is used very efficiently in imaging solid state objects and gases but there is nothing published about the use of this sequence on biological systems. Most likely because it uses N^2 number of echoes to image a $N \times N$ matrix, which may even though the technique uses small tip angles, push the SAR limits above safety for human imaging. To date there has been no clinical application of this pulse sequence.

3.1.3 Lung Perfusion Using MRI

To look at the pulmonary vasculature there are two main types of MR imaging techniques; either invasive or non-invasive. Non-invasive methods use 2D or 3D time of flight techniques, arterial spin labeling (ASL), or employ difference in perfusion due to cardiac phases (Hatabu et al. 1989; Mai et al. 2002; Keilholz-George 2001; Mai et al. 1999; Ogasawara et al. 2004; Knight-Scott et al. 2001). An invasive method uses an intravenous injection of gadolinium chelate contrast agent such as Gd-DTPA-BMA (gadodiamide injection, Omniscan, Amersham/ GE Healthcare), to increase the contrast. The gadodiamide contrast agent produces high-quality vascular imaging without artifacts caused by flow phenomena. One advantage of intravenous MR contrast agents over conventional angiography and CT contrast agents is that, unlike iodinated contrast media, gadolinium chelates are not nephrotoxic (Berthezene et al. 1999; Bader et al. 2002).

Non-invasive perfusion has been well evaluated by Ogasawara et al. (2004). This group has performed lung imaging using an electrocardiogram-gated (ECG-gated) fast spin echo pulse sequence to study perfusion in pulmonary artery-occlusive and chronic obstructive diseases. The MR data was compared to a currently used lung scintigraphy method. Images were acquired without any breath holds and during systole and diastole periods. This technique showed diagnostic sensitivity and specificity, as high as 90.3% and 98.0% respectively, without bringing any discomfort to the patients and without use of any contrast agents.

A similar technique by Knight-Scott et al. (2001) uses ECG-gated SSFSE acquisition to image lungs in different periods of the cardiac cycle. During each ECG trigger one slice with this technique is acquired in 350 ms. Unfortunately, though, the scan times were too long; spanning over 1/3 of the cardiac cycle. Since the middle of k-space is acquired first with the SSFSE technique most of the signal change will be

acquired within 70 ms, making signal change potentially observable when triggered in different cardiac phases. Additionally most motion would be at the beginning of systole, during the center of the k-space acquisition thus making more pronounced motion artifacts. This group also compared signal change to blood flow by comparing acquired data to a mathematical blood velocity model by Berne and Levy (1993).

A number of techniques for imaging lung perfusion and ventilation have been evaluated (Mai et al. 1999). Via arterial spin labeling (ASL) using a Flow-Sensitive Alternating Inversion Recovery with an Extra Radio-frequency (FAIRER) pulse sequence. The basic principle behind this technique is that a sample of blood water is magnetically labeled using a 180^o RF pulse. Then the signal from that sample is detected as it moves through the lungs. In other words blood water is used as an endogenous freely diffusible contrast agent. ASL techniques have been used not only for perfusion measurements but also, when combined with the inhalation of some form of contrast agent such as nebulized gadolinium contrast agent vapor or 100% oxygen, they have also been shown as useful for measuring lung ventilation (Mai et al. 2002).

Intravenous MR contrast agents have been used for some time to image lung perfusion (Berthezene et al. 1999). A typical MR perfusion study involves a rapid scan capturing the pass of the bolus through the tissue. From this data then a perfusion map is constructed. Another use of contrast agent is often applied to MR angiography. This is achieved by acquiring a mask image first, before the presence of gadolinium, then a second image is acquired around the peak of the contrast bolus presence. The images are subsequently subtracted producing an angiogram. It is essential within this procedure that both scans are performed within one breath hold to avoid subtraction mismatches.

Recent work by Berthezene et al. (1999) and Ogasawara et al. (2004) compared perfusion images acquired using MR methods to perfusion scintigraphy showed ex-

cellent sensitivity and specificity of MR images in their diagnostic ability. In fact the Berthezene et al. (1999) and Ogasawara et al. (2004) suggest using MR perfusion as an alternative to perfusion scintigraphy. Although authors have used two different methods of achieving perfusion measurements the results were remarkably similar. Berthezene et al. (1999) used contrast agents to achieve MR signal changes while Ogasawara et al. (2004) suggests that the non-contrast MR techniques used in their study for measuring perfusion is enough for diagnosis, and is more economical then perfusion measurement that use an expensive contrast agent. Other reports of using Gd contrast agent for perfusion measurements by Lin et al. 2004 suggest that using only wash-in of the contrast agent data rather then wash-in and wash-out images, gives even better diagnostic capability to MR perfusion studies. Further, combining MR perfusion with MR pulmonary angiography or MR ventilation study was used for the diagnosis of pulmonary embolism and other lung diseases.

Lung perfusion and angiography is improved at 3.0 Tesla relative to 1.5 Tesla. These techniques improve at higher fields as the gain in SNR now can be traded for speed. In recent studies by Finn and Laub (2004) MRA of the lungs was performed at 3.0 Tesla with the use of time resolved contrast-enhanced angiography, and a high resolution MRA with a 30ml Gd bolus, the images are superior to 1.5T MR angiography images. A higher field also results in less demand for Gd contrast, giving equal or superior MRA image quality with reduced dose relative to 1.5 T.

3.1.4 Lung Ventilation Using MRI

The idea behind MR ventilation is fairly simple: to image lungs and observe signal change brought on by ventilation. Signal change results from inhalation of either aerosolized or gaseous contrast agents. Studies showed that a relatively uniform

enhancement could be achieved using a small particle size on order of 2.5 μm (Kauczor et al. 2002; Haage et al. 2001). But when aerosols were used in patients with airway diseases the main deposition occurred only centrally along the main bronchi branches. Dynamic imaging of ventilation is not possible because of the long administration time $\sim$10 minutes . The problems with nebulized Gd is that most of the studies are not performed in patients. All of the studies were performed either on animals or a few human volunteers (Haage et al. 2003).

First proposed in 1996 by (Edelman et al.) to study lung ventilation, ground state molecular oxygen (O_2) is one of the simplest gaseous contrast agents. Because molecular oxygen is weakly paramagnetic (2 unpaired electrons) it affects the signal from the lung by shortening T_1 of the lung tissue, typically increasing the signal by about 15%. By performing T_1 mapping of the lungs before and during administrating of 100% O_2, and then subtracting images ventilation maps are generated. T_1 maps can be generated using one of two different techniques described in section 3.1.2. This technique is susceptible to changes in diaphragm position, often causing undesirable image blurring (Hatabu et al. 2001). Alternatively other gaseous agents not relying on signal from ^{1}H, such as ^{19}F and ^{3}He ^{129}Xe gases can be used. However all these will be discussed below, section 3.2.2.

Nonetheless one of the most promising ventilation-perfusion ratio (V/Q) techniques is imaging using O_2 enhancement with ASL technique (Mai et al. 2002). The oxygen-enhancement and ASL techniques show that perfusion/ventilation ratios could be measured safely and non invasively. In this study, ECG gated Flow Sensitive Alternating Inversion Recovery FAIR acquisition, the lungs were imaged before and during delivery of oxygen. By modeling the magnetization before and after O_2 delivery, the distribution of the V/Q signal intensity (SI) ratios were similar to the V/Q ratios obtained by the multiple inert gas elimination technique (MIGET).

3.2 Non-Proton Based Lung Imaging

3.2.1 Hyperpolarization Technique

Standard lung imaging using routine MRI capabilities is a challenge due to low signal strength, from markedly lower water content, relative to other body tissues. In addition the large gas (air) content and complex motion due to cardiac and respiratory function degrades the quality of lung images. Recently, however, the possibility to increase MR signal from noble gases by optically magnetizing or hyperpolarizing the gas through spin exchange and spin collisions has been introduced as a technique for imaging gaseous spaces in lungs.

MRI is inherently a low sensitivity technique, which originates from the low magnetic energy of nuclear spins ($\Delta E = \hbar\gamma B$) compared to the thermal energy ($k_B T$) at room temperature. At room temperature and at commonly used MRI magnetic fields (1.5 T) only a small percentage of atoms (approximately $5\text{x}10^{-6}$ %) contribute to the MR signal. In order to boost MRI signal, higher magnetic fields and lower temperatures can be used, however this is not a viable solution in human MRI studies. Another approach to increase MR signal is to polarize the nuclei of interest thereby increasing the ratio of spins aligned with the magnetic field by a factor approaching 10,000x. There have been a number of techniques proposed in order to enhance polarization of nuclei beyond naturally occurring thermal polarization, the most simple of which is achieved through optical pumping of noble gases, which are biologically inert and thus ideal for medical applications.

Optical pumping is done *ex situ* next to the measurement sample, producing large nuclear polarizations of ^{3}He and ^{129}Xe. Spin exchange optical pumping is a two step process in which an alkali metal vapor is polarized using photons, and the polarization

is then transferred to the noble gas nuclei during collisions via hyperfine interactions. In order to get alkali metal vapor, the gas container is heated to ~200 °C, while it is being polarized. A system that can be kept proximal to the magnet, yet not interfering with other MR procedures, is desirable. Noble gases are biologically inert and are ideal for applications in medical imaging. In order to perform MR imaging using different nuclei like ^{3}He or ^{129}Xe, birdcage radiofrequency coils tuned to the resonating frequency of these nuclei have to be designed and built. Unfortunately these need to be single channel coils and not capable of parallel acquisition schemes as most, if not all, MR systems to date are limited to one broadband transmit/recieve channel.

3.2.2 Ventilation Measurements Using ^{3}He, ^{129}Xe and ^{19}F

Gases are able to penetrate all of the lung tissue much easier than aerosols. One of the nuclei requiring the least amount of auxiliary hardware are gases that contain ^{19}F, for example Sulfur hexafluoride (SF_6) . The only requirement for performing a ventilation study using this nucleus is the availability of RF coils tuned for ^{19}F. Sulfur hexafluoride gas is almost insoluble in blood, has no known toxic effect, is inexpensive, and has been used for many years in clinical trials as part of the multiple inert gas elimination techniques. The drawbacks are that SF_6 is not yet certified for clinical routine application. And due to the higher density relative to other physiologically inhaled gases, the effect of gas retention in the lungs after exhalation is not fully understood. Other concerns using fluorinated gases are fast T_1 relaxation times and very broad RF excitation requirements.

Scans of animal models using SF_6 gas has been performed since 2000 when it was first attempted by Kuethe et al. (2000) in mechanically ventilated animals. The

images were collected using ultra fast PR pulse sequences, in the presence of different O_2 concentration. Observing wash-in and wash-out of SF_6 Kuethe et al. (2000) and Schreiber et al. (2001) showed uniform ventilation in healthy lungs and less ventilation in lungs that were mechanically blocked by a balloon. Another ventilation study by Laukemper-Ostendorf et al. (2002) uses a fluorinated contrast agent neat liquid perfluoro-octyl-bromide (PFOB) $C_8F_{17}Br$ (LiquiVent®, Alliance Pharm. Corp., San Diego, CA, USA) in animal models. By mechanical ventilation of the lung with a solution of PFOB with differing O_2 concentrations T_1 maps were produced. Since T_1 of ^{19}F is linearly dependent on the partial pressure of the surrounding O_2, the pO_2 from the T_1 images were calculated.

When first discovered in the 1960's hyperpolarized gas was looked at as an interesting phenomenon and no more. Today with the rapid development of MR, hyperpolarized gas has become one of the most useful tools for imaging lungs, possessing the ability to image not only the morphological structure of the lung but also its functionality. Currently ^3He is used preferentially because it possesses a greater magnetic moment then ^{129}Xe and longer depolarization time. Current polarization techniques for ^3He achieve polarization rates on the order of 30-50% 6 times greater than polarizations attainable for ^{129}Xe. There are many current superior reviews on clinical application of lung imaging using hyperpolarized gas from both European and American researchers (Kauczor et al. 2002; Roberts et al. 1999).

Helium-3, is an isotope that is rare on Earth and very expensive, but it is more common on the Moon (Johnson et al. 1999). Helium-3 can be used as clean fuel in fusion reactors, because its reaction is efficient and produces low residual radioactivity. With the further developments lunar ^3He might become an inexpensive source and be widely used in clinical applications.

3.2.3 Perfusion Measurements Using ^{3}He, ^{129}Xe and ^{13}C

To date there is still very little development in using other agents other then ^{1}H to image blood flow. One such development is a Dynamic Nuclear Polarization (DNP) of ^{13}C or other nuclei that possess spin. In recent studies DNP polarized ^{13}C enriched urea samples were injected in animals to perform angiography using urea as a contrast agent (Golman et al. 2003). The advantages of this technique is quite unique, because very little background signal from surrounding tissue is recorded and only signal from the ^{13}C is visible. This technique allows not only urea but any other endogenous substances to be used as a contrast agent. However, the use of DNP polarized samples is still in early stages of the development. In addition one significant difficulty includes rapid signal decay after *in vivo* injection (Ardenkjaer-Larsen et al. 2003; Golman et al. 2002; Mansson et al. 2002; Oros and Shah 2004).

3.3 Goals of Lung Imaging

The goal of lung imaging is to acquire a "complete picture" of the lung, by evaluating health of parenchyma, perfusion, and ventilation. The ideal approach to MR lung imaging is to keep the comfort of patients high, the use of invasive techniques minimum, and to collect clinically valuable data.

3.3.1 Lung Imaging and Magnetic Field Strength.

Lung imaging at higher field strengths has not been studied extensively, partially due to the lesser availability of clinical MR systems with fields higher then 1.5 Tesla. In theory the NMR signal increases as the square of the field strength. While noise

increases linearly with field. Thus, signal to noise ratio (SNR) is proportional to magnetic field B_o

$$SNR \propto B_o. \tag{3.1}$$

The increase of signal is beneficial for many aspects of MR imaging, and spectroscopy. However, the susceptibility in lung at higher field increases, dephasing the spin rapidly, thus T_2^* of the lung is smaller at higher field. This makes it more challenging to use gradient echo pulse sequences for lung MR. Most likely the optimum field strength for the use of gradient echoes in lung imaging is somewhere between 0.5 and 1.5 Tesla.

Further improvements in the use of surface coil arrays will only favor higher field systems because SNR gain with B_o is greater when the coil loading is reduced. Alsop et al. (1995) suggests that the nature of contrast in pathology must be examined before optimal field for detecting the pathology can be set. Spin echo pulse sequences however are slower, and thus harder to image parenchyma. However, they do benefit from the increase in SNR. Thus it is possible with higher SNR at higher field to trade speed for resolution.

On the other hand low magnetic fields were reported to be used, as low as 0.2 T by Muller et al. (2001), and showed well the pulmonary system but the promise of using such low fields for evaluating lung diseases is not very promising.

3.3.2 Proposal Methods

Imaging lung parenchyma using either fast GRE, SE pulse sequences and double inversion recovery pulse sequence. Minimizing signal from fat and muscle so that only signal from lungs is being acquired. This is accomplished using two inversion pulses one of which is a fat saturation RF pulse, minimizing signal from fat, and the second 180 ^{o} RF pulse is used to null out the signal from muscle, thus signal only from the

lungs parenchyma is measured. These techniques are very SAR intensive and can be used only on 1.5 Tesla efficiently to image full lungs.

Functional imaging of the lung imaging perfusion and ventilation is tested on two systems 1.5 and 3.0 Tesla. ECG-gated FSE sequence to image perfusion non invasively will be compared to contrast agent based methods. Thus comparing a free breathing non invasive technique to image perfusion with a breath held method involving an injection of a contrast agent. ^{1}H MRI of lung ventilation is achieved through observing signal change using nebulized gadolinium. By measuring how flow and perfusion of blood changes following the administration of oxygen or Gd aerosol it is possible to correlate the data with the ventilation in the lungs.

Contrast enhanced MR angiography is the most clinically applicable technique. This study will establish a protocol required for MRI angiography of the lung both at 1.5T and 3T MR systems. Currently, no protocol for lung angiography has been established at higher fields. Lung MRA will be performed on both 1.5T clinical system with a 20-30 cc Gd-DTPA BMA at 2 cc/s injection rate. At a higher field, strength of 3T less Gd-DTPA BMA is required for MRA so the scans will be repeated with a reduced dose of Gd-DTPA BMA.

Chapter 4

Experimental Methods and Materials

This chapter describes experimental procedures and the apparatus used for lung imaging experiments. In addition a detailed description of MR hardware, accessories, and pulse sequence parameters used to collect data are presented.

4.1 MR hardware

Two MRI scanners were compared differing only in magnetic field strengths (1.5T and 3.0T) (GE Healthcare® Milwaukee, WI). The scanners are identical in physical dimensions, and specifications apart from the field strength. A 3 T scanner is shown in Figure 4.1 and some specifications comparing the two systems are provided in Table 4.1. The scanners have similar capabilities running a cross compatible software, meaning that most pulse sequences on 1.5 Tesla will recompile and run on 3.0 Tesla, if the pulse sequence is programmed to take into account field strength differences.

Two field strengths 1.5 and 3 Tesla correspond to two different Larmor frequencies in the RF range of 63.86 MHz and 127.73 MHz respectively. These RF frequency band widths are associated with very high frequency-low (VHF-LO) television channel 3-4, and the frequency band from 122 to 174 MHz is used as a general service band radio transmission. Stray RF signals in the Larmor frequency band interfere with MR, this is why most of the MR and NMR experiments must be isolated by grounded Faraday RF cages. Both scanners used in the experiments are located in specially designed RF shielded rooms.

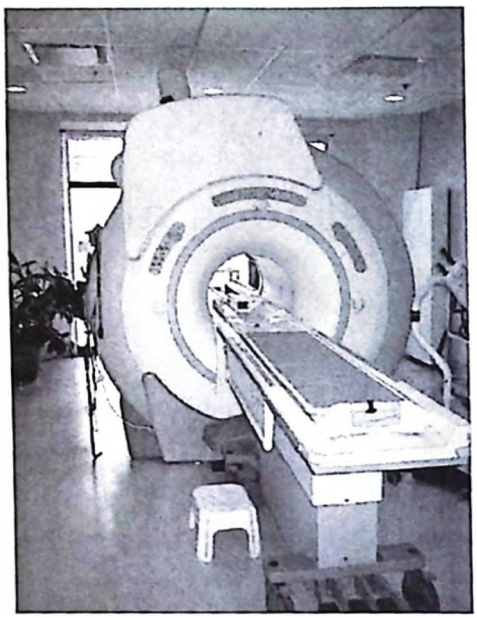

Figure 4.1: The GE Healthcare® 3.0 Tesla MRI scanner in the Imaging Research Center of St Joseph's Healthcare Hospital.

Table 4.1: Parameters of MR Magnets used in the experiments.

	GE Signa Excite 3.0 T	GE Signa Excite 1.5 T
Magnetic Field Strength (T)	3.0	1.5
Water Center Frequency (Hz)	127,799,074	63,867,605
Maximum FOV (cm)	60	60
Shimmed area (cm)	45x48	45x45
Field Inhomogeneity (ppm)	0.349593	N/A
Band Width (Hz)	500	500
RF Power (Body Coil)		
Max Output Power (Watts)	25,000	16,000
Max Average Power (Watts)	1,250	1,000
Max Pulse Energy (Joules)	125	60
Max Pulse Width (ms)	50	20
Gradients (Whole)		
Max Rise Time (μs)	288	288
Max Amplitude (Gaus/cm)	2.3	2.3
Slew rate (Tesla cm^{-1} s^{-1})	80	80
Software		
OS version	G3.0_M4A_0429.a	11.0_M4_0403.a

NMR signals are collected using RF coils. The principle behind signal acquisition lies in Faraday's law of induction, where the rotating magnetization vectors induce an electromotive force (EMF) in RF receiver coils. Perpendicular orientation of an RF coil to the rotating M_{xy} vector permits most efficient detection. Essentially an RF coil acts as tuned circuit that resonates at the Larmor frequency. RF coils may vary in size and geometry. For example each coil is designed for a specific part of the body. For imaging purposes it is necessary to excite nuclei into a coherent precession, uniformly throughout the entire sample. Thus design of RF antennas capable of generating a uniform RF field is an essential key behind good quality images. In all of the experiments described in this chapter a body coil built into the scanner was used for excitation purposes and an 8-channel torso array (USA Instruments, Inc.) was used for receiving. Two different coil arrays tuned specifically to the Larmor frequencies of the B_o fields were used (i.e. 1.5T and 3.0T).

Advantages of using an array rather then a simple coil comes from the fact that the coil can be composed of smaller elements reducing coil load and increasing coupling to the body, resulting in SNR gain. A schematic of a torso array coil is shown in Figure 4.2. It consist of two parts bottom and top with 4 coil elements each. Each element is sensitive only to a portion of the entire object. Information from all channels is recorded and summed together producing a final image. A more detailed description of how images are formed from phase array coils is included in section 4.5.1.

The main role of the gradient coils is to produce uniform magnetic field gradients, rapidly without affecting image quality. MRI scanners used for the experiments come with two gradient coil modes; a weaker gradient set designed for large field of view, "whole" mode, and stronger faster gradients for smaller field of view, "zoom" mode. For all experiments involving large field of view, gradients were used in the "whole" mode.

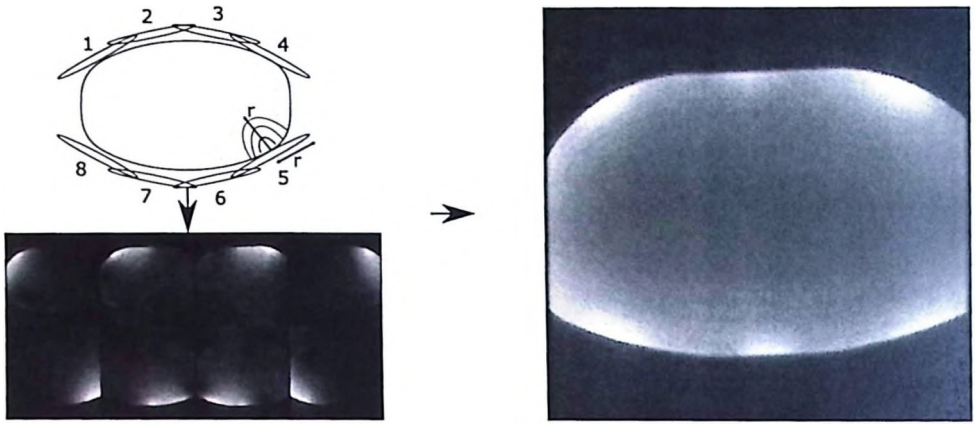

Figure 4.2: Coil Schematics. 8 Coils radius r measures signal from the surrounding tissue. Producing a composition of images for every channel of the coil. Data from all the coils is reconstructed to produce a final image.

The quality of an image largely depends on the signal to noise ratio (SNR). SNR calculations used in the experiments were based on the model that the measured signal from a single coil $\hat{x}$ can be written as:

$$\hat{x} = x + \xi \tag{4.1}$$

where x is the true signal and ξ is noise component with mean zero and standard deviation σ_ξ. SNR is then given by

$$SNR_{\hat{x}} = \frac{|x|}{\sigma_\xi} \tag{4.2}$$

If the images are averaged N times the signal to noise ratio increases. The standard deviation of the averaged noise can be written as $\sigma_{\xi_n} = \sigma_\xi/\sqrt{N}$ then signal to noise for averaged signal becomes

$$SNR_N = \sqrt{N}\frac{|x|}{\sigma_\xi} \tag{4.3}$$

So it is easily seen that SNR improvements go as square root of number of averages.

Calculating SNR for images produced by phased array coils is more complicated than the above description. The noise in the images produced using phased array coils is contributed by multiple receivers. If mean standard deviation of noise is zero then by averaging it out over multiple receivers improves SNR. However if correlation between the noise from different coils is present SNR will decrease with the increase of noise. It is possible to account for the correlated noise during image reconstruction using Eq. 4.5 (Constantinides et al. 1997).

A more correct approach for SNR measurements of images collected using multi phase array coils is described in detail by Constantinides et al. 1997. However for the purpose of this thesis the above Eq. 4.2 is sufficient, as long as the calculations are preformed in a constant manner throughout the experiments. SNR measurements are performed by placing 3 ROI's in noise, muscle, lung and highest intensity ghost. From these ROIs 9 SNR measurements for each tissue and ghost are calculated. The mean and standard deviation of the SNR is presented throughout the chapter 5.

4.2 Magnetic Resonance Contrast Agent

The contrast agent used in the experiments was Omniscan gadodiamide injection (Amersham, GE Healthcare®). It is a gadolinium complex of diethylenetriaminepentaacetic acid bismethylamide (GD-DTPA-BMA). Clinically gadodiamide can be used for MRI contrast enhancement of lesions (e.g. tumors). Additionally it is used as an angiography contrast agent to visualize the larger blood vessels. Contrast agent dose is given according to monograph provided with the product, and varies with patient weight. Some of the values are displayed in Table 4.2.

Intravenous contrast injection is followed by a "flush" of saline solution (0.9% NaCl). This ensures complete delivery of the agent and a tighter bolus of Gd-DTPA-

Table 4.2: Concentrations of Gd-DTPA-BMA used for injection as a function of body weight. Smaller doses of Gd were used at 3T to produce the same contrast enhancement as with a higher dose at 1.5T.

Body Weight (kg)	Adult Dose 1.5T 0.1 mmol/kg Volume (ml)	Adult Dose 3.0T unknown mmol/kg Volume (ml)
60	12	10
70	14	10
80	16	10
90	18	10
100	20	20

BMA. Inhalation previously attempted for lung imaging of Gd-DTPA-BMA is an off label use. Yet MSDS data on gadodiamide states possible allergic reaction to material if inhaled.

Throughout the studies the gadodiamide was administered, by trained professionals, and a physician was always present to treat any adverse effects that subject may experience. Volunteers were informed of all possible adverse reactions and consent was taken prior to contrast administration.

4.3 Ventilation Measurements Using Nebulized Gd-DTPA-BMA

Ventilation measurements were attempted by measuring signal change in the lung before and after delivery of nebulized gadodiamide. T_1 weighted multi slice fast imaging methods were applied in order to try and capture the signal change in the lungs.

A Respigard-II jet nebulizer was used to aerosolize gadodiamide producing particles of diameters 2 - 5 μm. The nebulizer has an inlet for compressed air, which

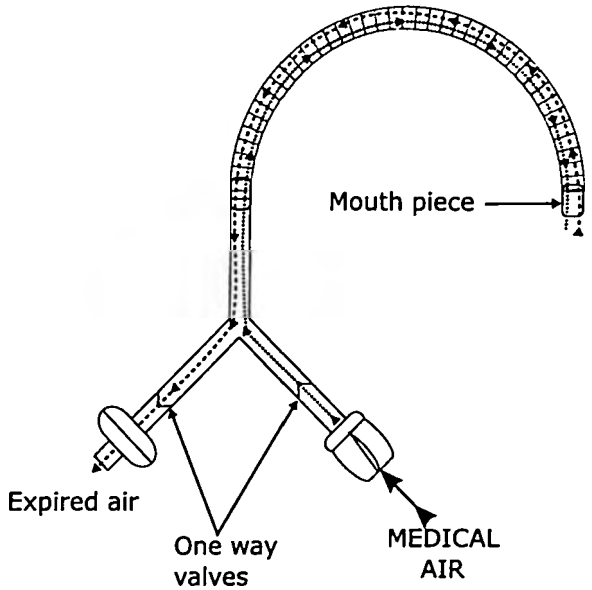

Figure 4.3: Nebulizer setup consists of a Respigard-II nebulizer, a filter that captures any expired aerosolized medication, and two one way valves. The subjects inhaled nebulized Gd through the mouth piece connected to plastic rib tubing. The one way valves were connected such that the inhaled air was 100% aerosolized mixture while most of the expired air will leave the nebulizer system through the capture filter, thus preventing expired Gd from exiting the system.

passes through and aerosolizes the Gd solution. This was connected to one end of a "y" shaped connector containing a mouth piece and filter (Figure 4.3). Hospital medical air was delivered at flow rates of 9-11 L/min in order to nebulize gadodiamide solution.

Subjects were asked to place the mouth piece in their mouth and create a tight seal around it with their lips. Gadodiamide was mixed with saline to produce a 0.16 mM solution of Gd. This was aerosolized and inhaled by 3 volunteers.

To visualize the effect of nebulized Gd in the lungs a rapid T_1 weighted pulse sequence was used, (EC-TRICKS). This sequence provides rapid imaging with the shortest TR and a better T_1 weighting comparing to all other GRE based pulse sequences, however it has a complex k-space acquisition (described in section 2.5.2). Nevertheless it was able to cover the entire lungs in one shot during a single breath

Table 4.3: Parameters used for EC-TRICKS pulse sequence during the ventilation studies with nebulized Gd, all of the parameters are for 1.5T system.

Parameter Name	Value
Pulse sequence	TRICKS
FOV(varying)	35-40 cm
Acquisition Matrix Size	160x128
Flip Angle	45
Echo Train Length	0
TR	4.7 ms
TE	1.4 ms
Slice Thickness	5-7.0 mm
Slice Spacing	0-7 mm
Number of Slices	26-34

hold. EC-TRICKS was not available at the time for 3.0T system so all of the Gd studies were performed on a clinical 1.5T scanner.

Subjects were positioned supinely, with arms above their heads, imaged using an 8 Channel torso array coil (see section 4.1). The nebulizer was provided only when required to breath aerosolized gadodiamide. The scan parameters used are shown in Table 4.3. These were chosen to have shortest TE possible, with reasonable imaging time to scan the entire lungs in one breath hold.

Two different protocols were used for ventilation studies. At first simple studies pre and post contrast delivery were acquired. Later the protocol was extended to include a longer delivery of Gd and to increase number of scan averages by repeating the scan multiple times. The second protocol was performed in the following order:

1. 5 scans breathing normal room air
2. 5 scans breathing 100% oxygen
3. 5 scans breathing nebulized saline
4. 5 scans breathing nebulized gadodiamide

Increasing the number of scans was done in an attempt to increase SNR for each of the four conditions. Each scan was performed during one breath hold, so a total of 20 breath holds was required during the entire protocol. Mask images from each of the series were averaged and compared to the different conditions.

4.4 Lung Parenchyma Imaging Using Double Inversion Recovery Pulse Sequence

Parenchyma imaging was performed using a double inversion recovery technique in which signal from the fat and muscle were suppressed by two inversion pulses leaving parenchyma signal. The result is an image that has increased parenchyma contrast compared to the other two tissues.

Signal from the thoracic fat and muscle always overwhelms that of lung parenchyma, resulting in poor contrast between the tissues, which is ultimately diagnostically useless. The principle of double IR pulses can be explained through relaxation diagrams shown in Figure 4.4. T_1 values for muscle, lung parenchyma, and fat as well as tissue spin density have to be known (Table 4.4).

Through application of two preparation 180° RF pulses, prior to a spin echo the resultant longitudinal magnetization from fat and muscle are minimized. The resultant longitudinal magnetization after two 180° RF pulses can be derived from Eq. 2.16 as:

$$M_z(TI_1 + TI_2) = M_o(1 - 2e^{-TI_2/T_1} + 2e^{-(TI_1+TI_2)/T_1}) \tag{4.4}$$

Where TI_1 is the time between the first and the second 180° pulse while TI_2 is the time between the second 180° and the 90° RF pulse (Figure 4.4). At 1.5 Tesla optimum TI_1 and TI_2 were reported to be 800 and 150 ms respectively.

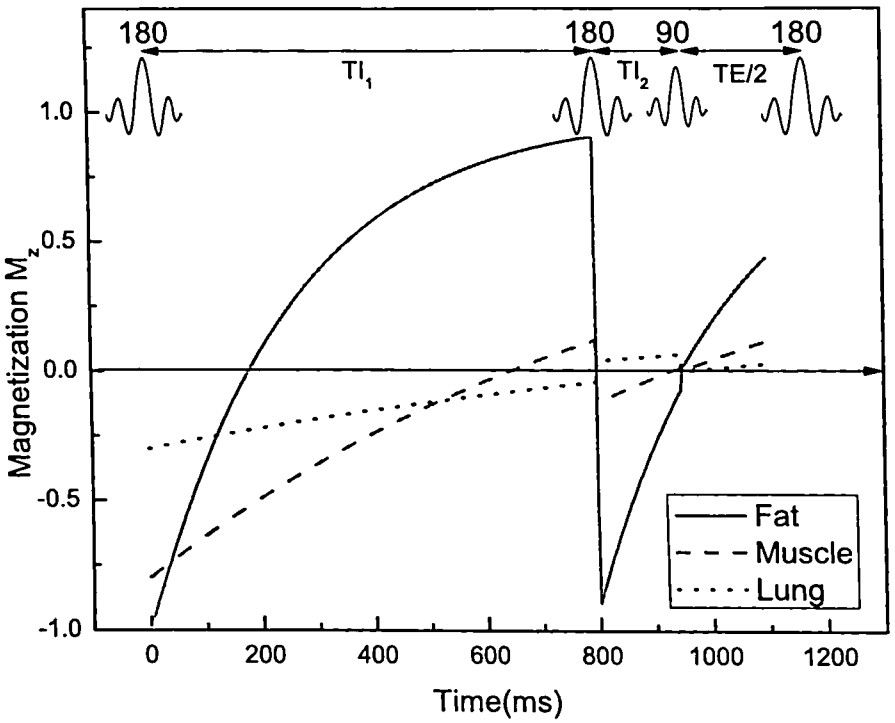

Figure 4.4: Two 180° RF pulses are applied prior to the data acquisition, if TI_1 and TI_2 are spaced properly then it is possible to suppress signal from two or more tissues. The RF timing follows $180^o - TI_1 - 180^o - TI_2 - 90^o - TE/2 - 180 - TE/2 - echo$.

Table 4.4: T_1 and spin density values of tissues at 1.5 Tesla as reported by Mai et al. 1999. Spin density was estimates from a spin density weighted image and normalized to spin density of thoracic fat.

Tissue	T_1 (ms)	Relative Spin Density
Muscle	932 ± 63	0.8
Fat	260	1
Right Lung	1370 ± 18	0.3
Left Lung	1410 ± 21	0.3

Table 4.5: Parameters used for FSE-IR pulse sequence with an extra blood suppression inversion pulse, all of the parameters were for the 1.5T system.

Parameter Name	Value
Pulse sequence	FSE-IR
FOV(varying)	35-40 cm
Acquisition Matrix Size	256x160
Echo Train Length	1-32
TR	900-2500 ms
TE	26-40 ms
Slice Thickness	5-7.0 mm
Slice Spacing	0-7 mm
Number of Slices	4-15
TI_1	800 ms
TI_2	150 ms

In the experiments the exact pulse sequence used by Mai et al. (1999) was not available. Instead an inversion recovery Fast Spin Echo (FSE-IR) pulse sequence with additional adiabatic inversion RF pulse was applied. Imaging parameters were set according to Table 4.5.

Subjects were scanned supine using an 8-channel torso phased array coil with arms above their heads. Breath holding was required during image acquisition. If scans were too long for a single breath hold they were broken down into series of acquisitions.

4.5 Perfusion Imaging

Images of lung ventilation and parenchyma were acquired in the previous two experiments. In order to gather a complete lung picture, perfusion was imaged. Two different approaches were explored for producing perfusion images. A non invasive perfusion imaging method requiring ECG gating was compared to a second method

using intravenous injection of MR contrast agent. The use of contrast agents has grown in clinical popularity for performing rapid scans, and producing valuable clinical information. However due to cardiac motion the contrast agent scans blur images around the heart. The two techniques were compared at two magnetic field strengths 1.5 and 3.0 T.

4.5.1 Non Contrast Fast Spin Echo Electrocardiogram Gating Perfusion Measurements

From previous section 2.4.2 one obvious choice for lung imaging, is a spin echo pulse sequence. The spin echo does not suffer from the rapid T_2^*, however it is a slower pulse sequence, because it is impossible to refocus a spin echo as fast as gradient echo.

For non invasive perfusion imaging a fast spin echo (FSE) pulse sequence, with electrocardiogram (ECG) gating was used. ECG trigger points were changed throughout the cardiac cycle. Recorded MR signal during different cardiac phases was used to observe lung perfusion. Respiratory motion correction was performed off-line from recorded scanner trigger points and the respiratory waveform.

Subjects, prepared by a certified MRI technologist, were positioned supine with four ECG leads connected to their chest or back. A respiratory bellows was placed around their waste to monitor respiratory cycle (Figure 4.5). Arms were positioned proximal to their sides to improve subject comfort during long scan times. Scanning parameters for ECG gating are shown in Table 4.6 while image weighting parameters are tabulated in Table 4.7, assuming that the heart rate is between 60-70 bpm, images produced were proton density and T_1 weighted.

With ECG triggering the total scan time varied according to subject heart rate. Physiologic parameters (ECG and respiratory cycle) and trigger points were recorded

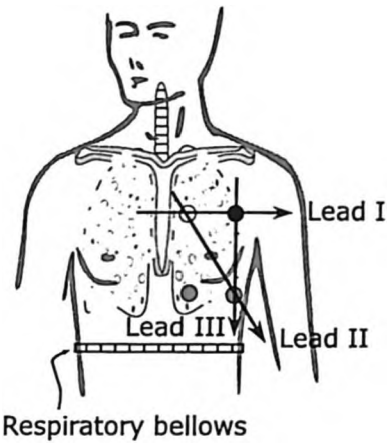

Figure 4.5: ECG leads and respiratory bellows placement. Four ECG leads were placed in spaces between the ribs to provide three possible readings Lead I -III. Respiratory bellows was placed around the waste for recording respiratory cycle.

Table 4.6: Parameters used for FSE with ECG gating pulse sequence, the scans were performed on both 1.5 and 3.0T systems. *NOTE[1]: TR will vary according to the heart rate of the subject.*

Parameter Name	Value 1.5 T & 3.0 T
Pulse Sequence	FSE
FOV(varying)	35-40 cm
Acquisition Matrix Size	128x128
Echo Train Length	6
TR	varying[1]
R windows	20%
R-R intervals	2-4
Trigger delay	13-800 ms
TE	9 ms
NEX	6-18
Slice Thickness	10 mm
Number of Slices	1

during the entire scan. Raw image data (i.e. k-space) acquired during the scan was then sorted and reconstructed off-line using an in house Matlab® script that took into account respiratory motion.

Table 4.7: Parameters used for FSE pulse sequence, and image weighting they produce.

1.5 Tesla			
	PD	T_2	T_1
TR (ms)	Long, > 2000		Short, < 600
TE (ms)	Short, < 30	Long, > 90	Short, < 20
ETL	Short, < 8	Long, > 8	Short, < 4

3.0 Tesla			
	PD	T_2	T_1
TR (ms)	Long, > 2000		Short, < 800
TE (ms)	Short, < 30	Long, > 80	Short, < 20
ETL	Short, < 8	Long, > 8	Short, < 6

Simultaneous respiratory and cardiac gating can not be performed on the GE Excite MRI Scanner. It is possible to perform cardiac gating and respiratory compensation with a simple spin echo pulse sequence. Respiratory compensation involves matching k-space to respiratory cycle (i.e. k-space lines are acquired according to the current position of the respiratory cycle). However we wanted to accelerate acquisition time through the use of FSE pulse sequence. Thus instead of using online reconstruction, frequency data of k-space was saved and then reconstructed using physiological data, collected during the scan.

Scanner software was modified such that k-space data was recorded on disk in sequential manner as it was acquired. The ECG and respiratory waveforms, with trigger points were also recorded in a file. The k-space acquisition ordering of FSE pulse sequence, was recovered from the pulse sequence code, for the parameters listed in Table 4.6 the manner of k-space acquisition is shown in Figure 4.6. Each line of k-space was acquired from one refocused echo, but with the use of the FSE, and scan parameters listed in Table 4.6, raw data was acquired in a series of 22 view windows

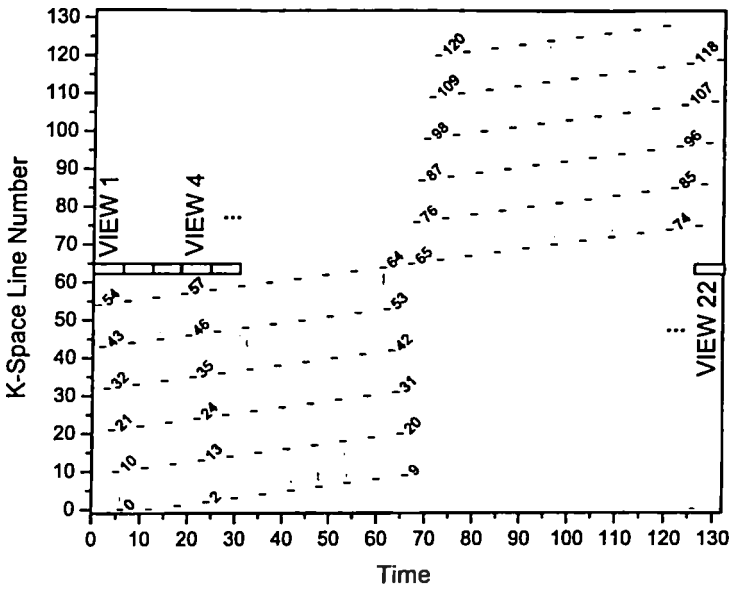

Figure 4.6: Each line of k-space was acquired according to the above figure. Each view was collected after a trigger, in total 5-6 lines of k-space can be acquired simultaneously. Those lines that have a value of a zero are considered baselines, and are added to the end of the data file. This acquisition scheme is repeated every NEX.

each sampling 6 lines of k-space. The time to acquire one view window $T_{View\ Window}$ depends on ETL and TE as

$$T_{View\ Window} = ETL \times TE.$$

Each of the views belong to a time point triggered from the ECG signal as shown in Figure 4.7. The trigger point was always an R wave, only the trigger delay data was varied and was collected throughout the entire cardiac cycle.

Respiratory motion correction was performed using a minimal variance algorithm (MVA). The basic principle behind this algorithm is to sort k-space data according to the physiologic state. First k-space data is over sampled in time. It is sorted

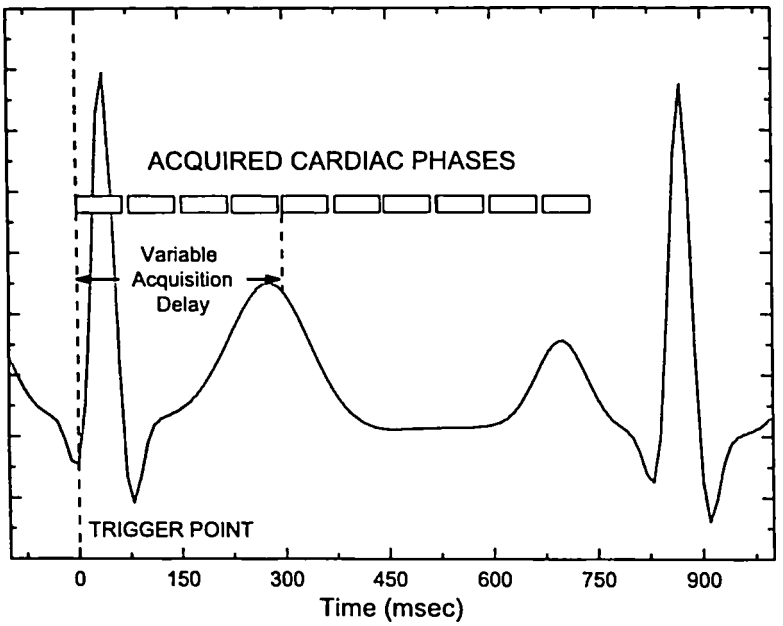

Figure 4.7: ECG trigger points vary throughout the entire cardiac cycle. Images are acquired only during the short window after the variable trigger.

according to its location in k-space and time point of collection. The limit of allowed physiological motion is preset by the user. Subsequently data that was collected outside of the permitted range is discarded. Remaining data is sorted into appropriate k-space positions and reconstructed (see Figure 4.8 and appendix A for more details). In addition to k-space reordering, location of k-space data from multiple coils needed identified and used in final reconstruction.

Images from the 8 individual coils of the torso phased array were combined using a sum-of-squares (SoS). As shown by Larsson et al. (2003) and Roemer et al. (1990) SNR improvements of an optimally reconstructed image from known coil sensitiv-

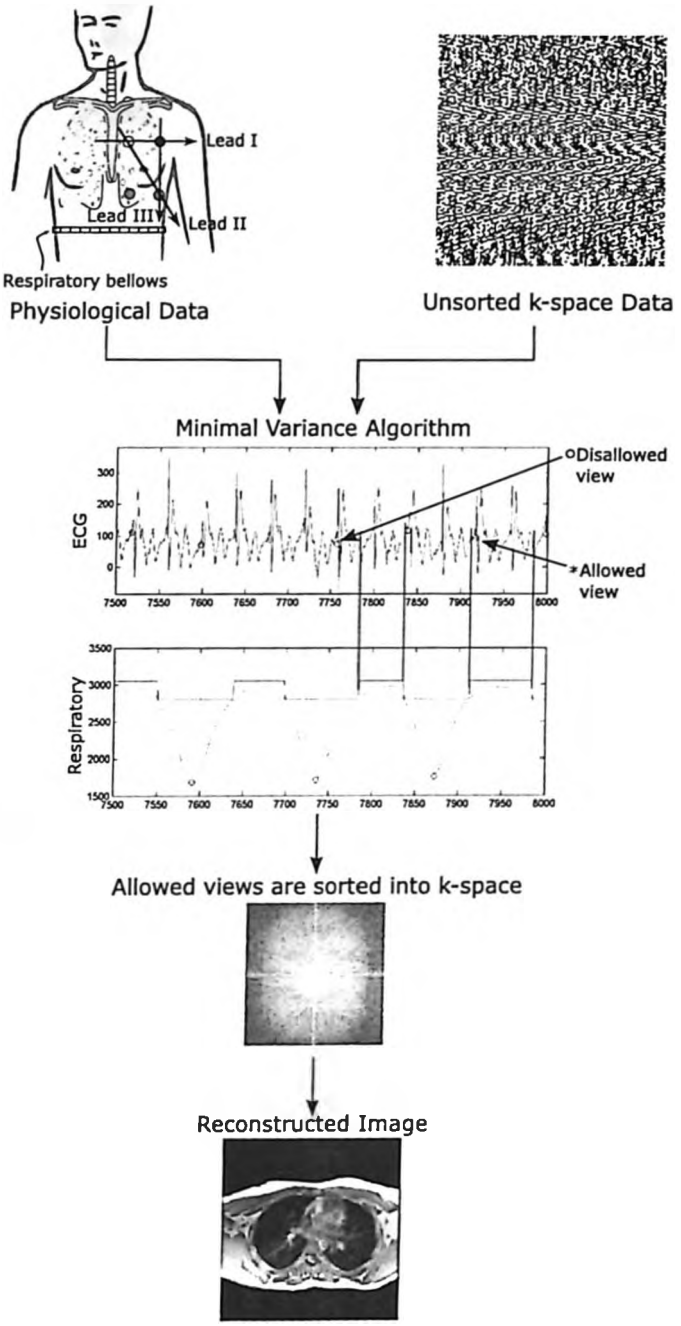

Figure 4.8: Physiological data and k-space data was first recorded over an extended period of time usually over sampled by a factor of at least 3 times. A minimal variance of physiological data was specified by the user or can be calculated automatically. In this figure k-space data collected during inspiration is filtered and allowed views of k-space are combined to produce the final image.

ity profiles over the SoS method is minuscule. Image I(x,y) was thus reconstructed according to:

$$I(x,y) = \sqrt{\sum_{j}^{n} \left(\frac{I_j(x,y)}{\sigma^2} \right)}, \tag{4.5}$$

where $I_j(x,y)$ refers to image from coil j, and σ^2 is the mean squared deviation of noise or noise variance. The scanner measures the noise variance for each coil during the scan by collecting data without gradients or RF pulses at the readout bandwidth of the prescribed scan. This data is called a baseline, and in the FSE pulse sequence it is collected when the view collects the 0^{th} line of k-space (Figure 4.6).

Because data was collected over a long period of time subject motion was unavoidable. Some subjects had to be moved out and put back in to the magnet due to a concern or a discomfort. In order to realign the images, ImageJ (http://rsb.info.nih.gov/ij/) software with StackReg plug-in (http://bigwww.epfl.ch/thevenaz/stackreg/) was used to align images between the scans.

4.5.2 Contrast Enhanced Magnetic Resonance Angiography

All bolus injections were delivered via power injector (Medrad, Spectris Solaris MR Injection System). Subjects were prepared by insertion of a plastic catheter into an antecubital vein, on a subject's left or right arm. The catheter was connected to the power injector containing two syringes: one containing the contrast agent and a second containing saline solution which was dripped through the intravenous line to prevent clotting until the contrast material was delivered. A 10-20 cc of contrast was injected at a rate of 2 cc/s followed by a 15 cc saline flush.

Two pulse sequences, EC-TRICKS and SPGR were applied for contrast enhanced perfusion scans. It is critical to match the timing of the bolus passing through the

Table 4.8: Parameters used for SPGR pulse sequence, the scans were performed on 1.5 and 3.0T system.

Parameter Name	Value 1.5 T & 3.0 T
Pulse Sequence	SPGR
FOV(varying)	40-44 cm
Acquisition Matrix Size	256x128
Echo Train Length	0
TR	7.6 ms
TE	1.7 ms
NEX	1
Flip Angle	73^o
Slice Thickness	10 mm
Number of Slices	1
Temporal Phases	30

respiratory organ with the image acquisition. The first experiments measured bolus timing in a healthy volunteer. This was accomplished by acquiring a series of 60 images with the temporal resolution of 1 second. The scan was performed in a single breath hold. Even though the bolus arrival varies from person to person we had an estimated time, which all other scans were referenced.

During experimental scans subjects were required to breath hold. The EC-TRICKS pulse sequence was prescribe to balance temporal and spatial resolution, while performing the entire scan in a single breath hold. This was done to minimize anatomic displacement that would ensue during two different breath holds.

The SPGR sequence was setup using the parameters shown in Table 4.8. At the time of the experiments the EC-TRICKS pulse sequence was not available for 3.0 T, so a 1.5 T version of the pulse sequence was modified in order to run on 3.0 T hardware. Parameters for the scan are listed in Table 4.9.

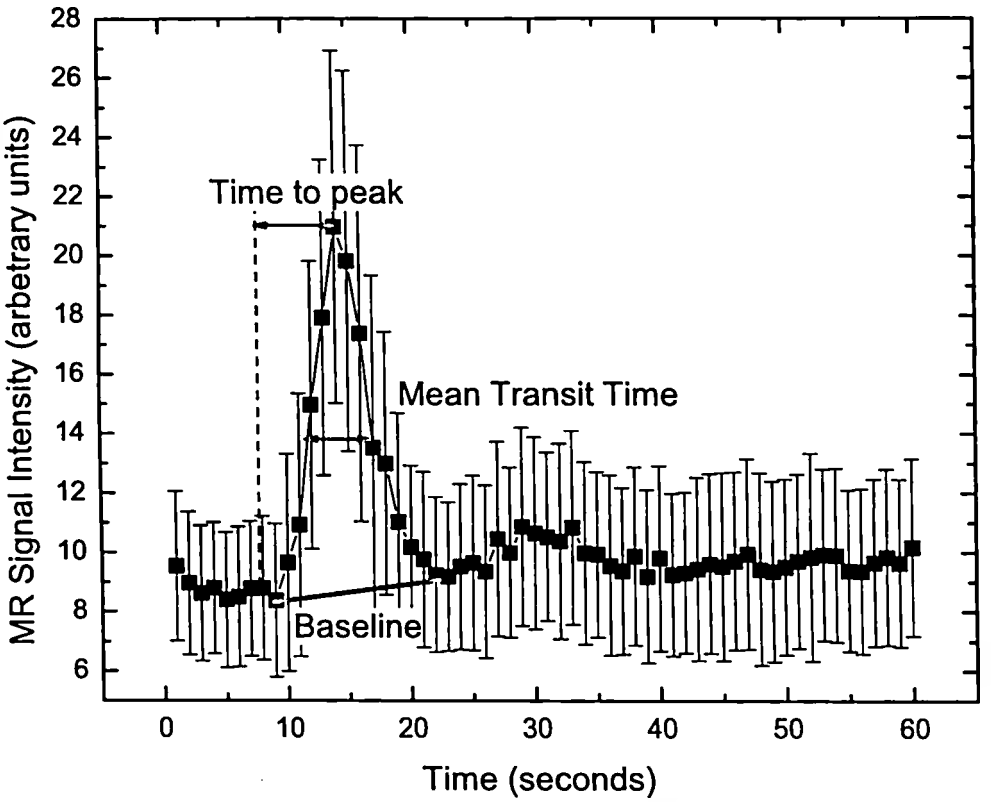

Figure 4.9: MR signal change in lung during a contrast agent bolus pass. Parameters such as: area under the curve, mean transit time and time to peak were used to calculate perfusion map.

Contrast enhanced perfusion maps were produced by pixel wise evaluation of signal changes with time, bolus mean transit time, time to peak, enhancement integral parameters were used to evaluate Gd-bolus based perfusion (Figure 4.9). Perfusion weighted maps were calculated using Functool2 software (GE Healthcare®).

Table 4.9: Parameters used for EC-TRICKS pulse sequence, the scans were performed on 1.5 and 3.0T system.

Parameter Name	Value 1.5 T & 3.0 T
Pulse Sequence	EC-TRICKS
FOV(varying)	40-44 cm
Acquisition Matrix Size	128x128
Echo Train Length	0
TR	NA
TE	0.95 ms
NEX	1
Flip Angle	6-15^o
Slice Thickness	2.5 mm
Locations per Slab	10
Total Slab thickness	25 mm
Number of Slices	1
Delay Time After Mask	0 ms
Temporal output phases	20

4.6 Relaxometry Measurements of Gd-DTPA-BMA at 3.0 and 1.5 T in Saline

The relaxivity of Gd-DTPA-BMA in saline was measured at two different magnetic field strengths 1.5 T and 3.0T, and two different temperatures (20°C and 37°C). Warm water, doped with 1 mM concentration of $MnCl_2$ (Manganese Chloride, M-3634, Sigma-Aldrich Co.) to shorten T_1 and nullify its signal, was circulated using a VWR (1167P, VMR International) programmable temperature controller. 3 cm diameter, 50 cc VWR centrifuge tubes with screw on lids, placed in a 3×6 arrangement in a plastic test tube holder acted as the phantom device. The entire set up was lowered into a 45x20 cm insulated bath, (setup shown in Figure 4.10). The vials were securely held in place to prevent any vibrational disturbances. Each vial had different concentrations of gadolinium which was mixed by diluting 0.5 mM/ml Gd-DTPA-BMA in an aqueous saline solution of 0.9% NaCl (concentrations used are shown in Table 4.10).

Table 4.10: Concentrations of Gd (mM) used in a 3 × 6 arrangement of tubes.

Gd Concentration (mM)		
0	0.05	0.1
0.15	0.2	0.25
0.3	0.35	0.4
0.5	0.6	0.8
0.9	2	3
4	5	6

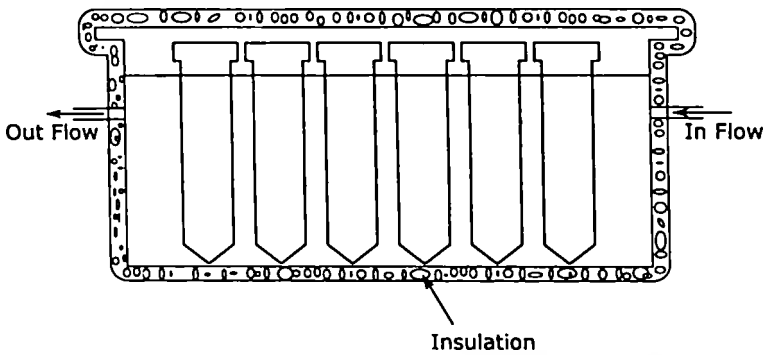

Figure 4.10: A temperature bath setup for gadodiamide relaxivity measurements. Flowing water is doped with $MnCl_2$ to significantly reduce T_1 of water.

An inversion recovery pulse sequence was used to calculate T_1 value of different Gd-DTPA-BMA concentrations. In order to speed up the measurements and minimize temperature fluctuations during the scan, the FSE-IR pulse sequence was used.

The pulse parameters were TE=16.3 ms, TR=10,000 ms and ETL = 12, inversion time TI varied from 50 to 2500 ms in total 25 data points were collected (50, 100, 150, ... 950, 1000, 1100, 1200, 1500, 2000, 2500) with a 26cm FOV, slice thickness of 2 cm and acquisition matrix of 256x128. Signal received from the FSE-IR pulse sequence as a function of TI can be written down mathematically as:

$$S(TI) = A\sqrt{(1 - 2Be^{-TI/T_1})^2} \tag{4.6}$$

where A and B are constants. Parameter $A \propto M_o$ while B denotes the deviation from a perfect 180^o pulse.

The calculation of T_1 values were obtained by measuring mean signal intensity in a circular region of interest (ROI) of the image. Mean and standard deviation data of the ROI was measured using ImageJ software. Data was fitted using a three parameter least-squares fit based on the Levenberg-Marquardt (LV) method, to Eq. 4.6. Origin Lab software's LV algorithm was used to perform the fit. R_1 was calculated as a slope of a linear Eq. 2.29 using a least squares fitting method.

Chapter 5

Results

Results presented in this chapter focus on various proton based MRI protocols assessed at 1.5 and 3.0 Tesla. Evaluation of Gd-DTPA-BMA relaxivity at two field strengths, through phantom measurements is also presented.

5.1 Gd Enhanced Ventilation Measurements

Ventilation measurements using Gd-DTPA-BMA were done on a test trial basis, only two volunteers were scanned, with one of the subjects being scanned multiple times. Images collected were analyzed by calculating relative percentage of signal $\%\Delta SI$ enhancement using the equation:

$$\Delta SI = \left(\frac{SI_1 - SI_2}{SI_1} \right) \times 100\% \tag{5.1}$$

where SI_1 is post-contrast and SI_2 is the pre-contrast image. The images acquired using the TRICKS pulse sequence on a 1.5 T system at 1 NEX were of significantly low SNR (Table 5.1). The percent signal change from pre and post aerosolized delivery of the Gd contrast agent was observed to be insignificant throughout the images: mean percent signal change, (mean value $\pm$ standard deviation), was 0.426$\pm$10.8. Similar results for percent signal change were obtained in other tissues surrounding lungs. The images were inherently of poor quality and unusable even for differentiating anatomic structures see Figure 5.1. In order to try and improve SNR of the EC-

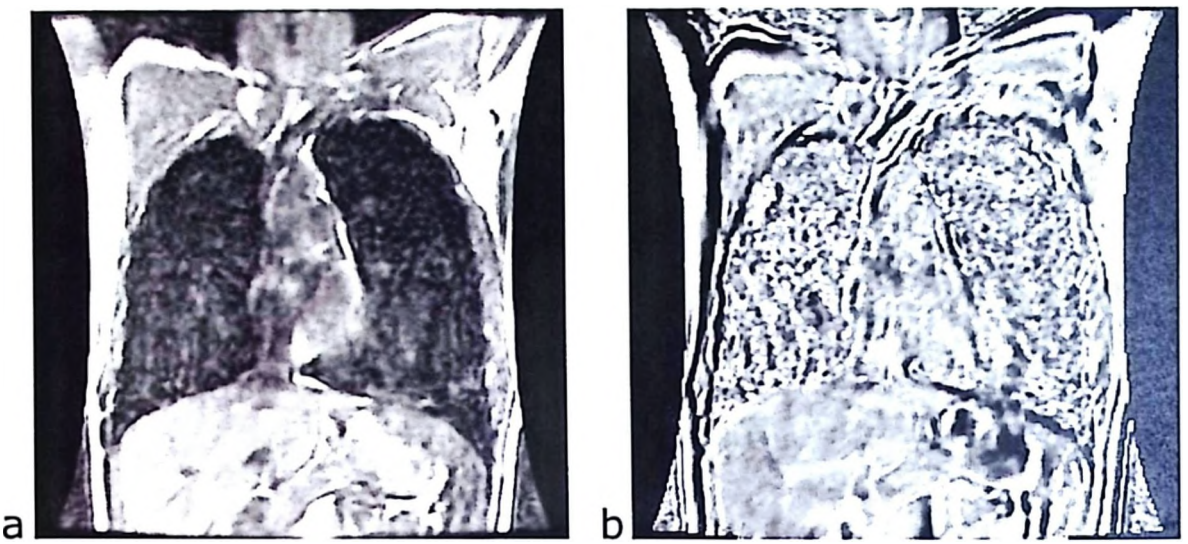

Figure 5.1: Lung ventilation images acquired at 1.5T using the EC-TRICKS pulse sequence at 8 NEX. Images were of low SNR and poor quality. a) Image of the lung pre ventilated contrast delivery. b) Percent signal change of pre and post Gd delivery. Lung structure is difficult to differentiate from image.

TRICKS sequence, scans were averaged over eight breath holds. Averaging resulted in an 11% gain of SNR comparing to 1 NEX (Table 5.1).

Table 5.1: Ventilation SNR at two fields. *Note: the SNR can not be compared between the two systems as two different pulse sequences were used.*

	1.5 Tesla TRICKS		**3.0 Tesla** SPGR
	1 NEX	8 NEX	1 NEX
SNR_{muscle}	17.05±11.57	19.51±12.5	120.45±60.1
SNR_{lung}	4.82±3.3	5.03±3.34	8.18±4.1

The higher field system did not have the TRICKS pulse sequence available, instead an SPGR pulse sequence was used. On a 3.0 Tesla system the mean signal change pre and post Gd inhalation in the lungs was 8.03±13.5%. The percent signal change for muscle was 2.84±2.64%. Significant bulk tissue motion was observed in the images (Figure 5.2), making it difficult to image ventilation without using a standardized method to produce uniform breath holds and minimizing motion between the scans.

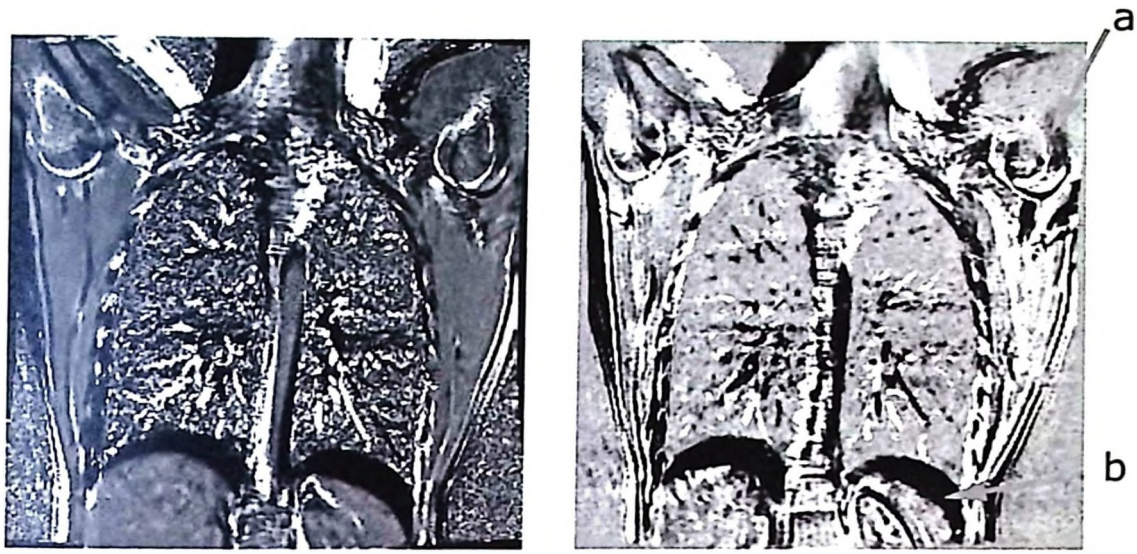

Figure 5.2: Lung ventilation images acquired at 3.0T using a SPGR pulse sequence. The left image shows signal change pre and post Gd inhalation. In the lungs mean signal change with standard deviation was found to be 8.03±13.5% and 2.84±2.64% in muscle. On the right a subtraction image of pre Gd from the post Gd delivery is shown. a) Ghosting of the head of the humerus produced by motion between the acquisitions. b) Two different breath holds cause signal loss in the location of the diaphragm.

5.2 Suppression of Muscle and Fat Signal Using Double Inversion Recovery

A double inversion recovery was used in attempt to perform imaging of the lung parenchyma. Suppression of the lipid and muscle signal was successfully performed in two volunteers, however there was still very poor differentiation between lung tissue parenchyma and other organs (Figure 5.3a). The data was acquired rapidly in a single breath hold. Scans were triggered from a peripheral pulse oximeter. In order to optimize suppression of signal from both muscle and fat, some scans were performed by varying inversion times. Lung and muscle signal change are shown in Figure 5.3b. However not enough data points were sampled in order to find optimal TI_2 for the suppression of MR muscle tissue signal.

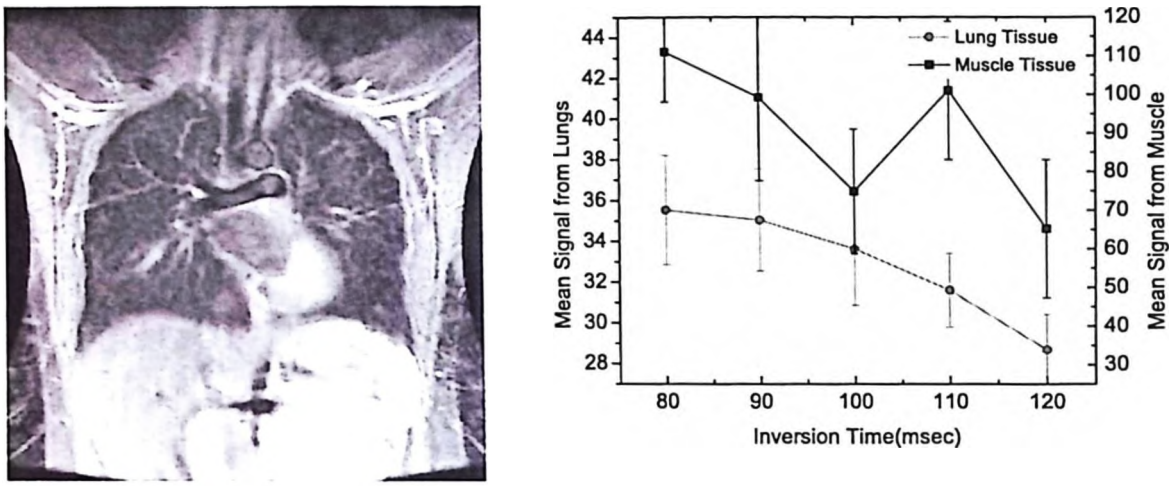

(a) (b)

Figure 5.3: (a)Lung images acquired at 1.5T using a FSE-IR pulse sequence with an extra black blood suppression pulse (TI_1=800ms TI_2=150ms, Subject 1). Mean SNR for the lungs was found to be 18.97±11.6 and 53.05±32 for muscle. The muscle and fat are suppressed but not suppressed enough to clearly see lung parenchyma. A breath hold technique requires fast acquisitions leading to long ETL, this contributes to blurring in the phase direction, which is already problematic due to lung motion. (b) By setting TI_1=800 ms and varying TI_2 the signal from the lungs and muscle are being suppressed (Subject 2). However not enough data was collected to measure signal from muscle suppression at the optimal TI_2=150ms.

5.3 Fast Spin Echo and SE with Electrocardiogram Gating

Breath holding techniques for eliminating respiratory motion are often difficult for people to perform. Another downside of breath hold techniques is a requirement for faster scans, which cause reduced SNR and blurring.

In this and the following section perfusion imaging of the lung was approached using two different methods. This section describes the results of perfusion imaging using a non-contrast, free breathing technique. The contrast for the perfusion in this technique uses lung blood flow to perturb the MR signal. In order to eliminate respiratory and cardiac motion retrospective gating was used.

Table 5.2: The FSE clearly brings numerous advantages over conventional spin echo. Calculations are for both sequences acquiring images at 128x128 matrix size, with 2-RR intervals and heart rate of 60 bpm. Fast spin echo specific parameters were ETL=6 , NEX=18. Increased NEX was necessary to over-sample data for retrospective gating.

	Fast Spin Echo	Spin Echo
NEX	18	6
Total Scan Time (minutes)	13.2	25.6
Usable data (%)	33-66	100
SAR (%)	84	100

5.3.1 Efficiency of FSE Motion Correction with Retrospective Gating and SE with Respiratory Compensation.

FSE imaging offers considerable advantages over SE techniques. For example, acquisition is faster and SAR is lower (Table 5.2). One disadvantage however is not all of the acquired FSE data can be used for retrospective gating. In order to minimize motion, only about 33% of acquired data that fall within the limits of the respiratory cycle is reconstructed. More data can be recovered by reconstructing data in expiration and inspiration respiratory phases.

Signal to noise and contrast to noise calculations were performed on 12 circular ROIs: 3 each for muscle, lung, highest intensity ghost, and in the background between the ghosts. ROIs were placed identically between subjects. Lung ROIs were kept away from major vessels. For the FSE sequence SNR measurements were averaged over three subjects.

Image acquisition using spin echo with respiratory compensation is slow, and respiratory motion correction is not perfect. Also the ghosting from muscle-fat still appeared in all of the images, albeit with lower SNR comparing to that of lung. Ghosting from the tissue surrounding lungs was observed in all of the images in the phase direction. Respiratory compensation and motion correction were comparable

Table 5.3: A comparison of SNR on 1.5 T and 3.0 T scanners using SE with respiratory compensation. Spin echo scans were performed with identical scan parameters on each system (1 NEX). Data from two different subjects are compared.

	SE with Respiratory compensation	
	1.5 Tesla	3.0 Tesla
SNR_{muscle}	102.3148±30.0	180.37±39.7
SNR_{lung}	12.26±3.5	22.17±4.7
SNR_{ghost}	6.72±1.6	13.81±2.7
$CNR_{muscle/lung}$	90.05±26.7	158.20±36.7
$CNR_{muscle/ghost}$	108.7±23.7	166.55±38.2

Table 5.4: Reconstruction of k-space data with and without motion correction at 3.0 Tesla. In total 9 SNR and CNR data points were measured and averaged over three different subjects. The data without motion correction was reconstructed for 6 NEX. As it was determined that only 33% of data can be used for motion correction, some lines of k-space were not averaged exactly to 6 NEX from the 18 NEX data set during retrospective gating reconstruction.

	FSE k-space data reconstruction on 3.0 Tesla	
	Without Motion Correction	With Motion Correction
	6 NEX	~6 NEX
SNR_{muscle}	207.87±50.9	204.29±47.0
SNR_{lung}	22.13±2.9	23.10±2.8
SNR_{ghost}	6.02±0.6	5.54±0.8
$CNR_{muscle/lung}$	185.74±48.8	181.19±44.8
$CNR_{muscle/ghost}$	202.03±50.6	198.28±46.9

in the inability to suppress ghosting. Note, the signal and contrast to noise ratios (of ghosts) were comparable between spin echo and fast spin echo experiments (Table 5.3 and 5.4). It is hard to quantify ghost suppression through SNR and CNR measurements. Instead ghosting was judged non-parametrically as high, moderate or low using visual inspection.

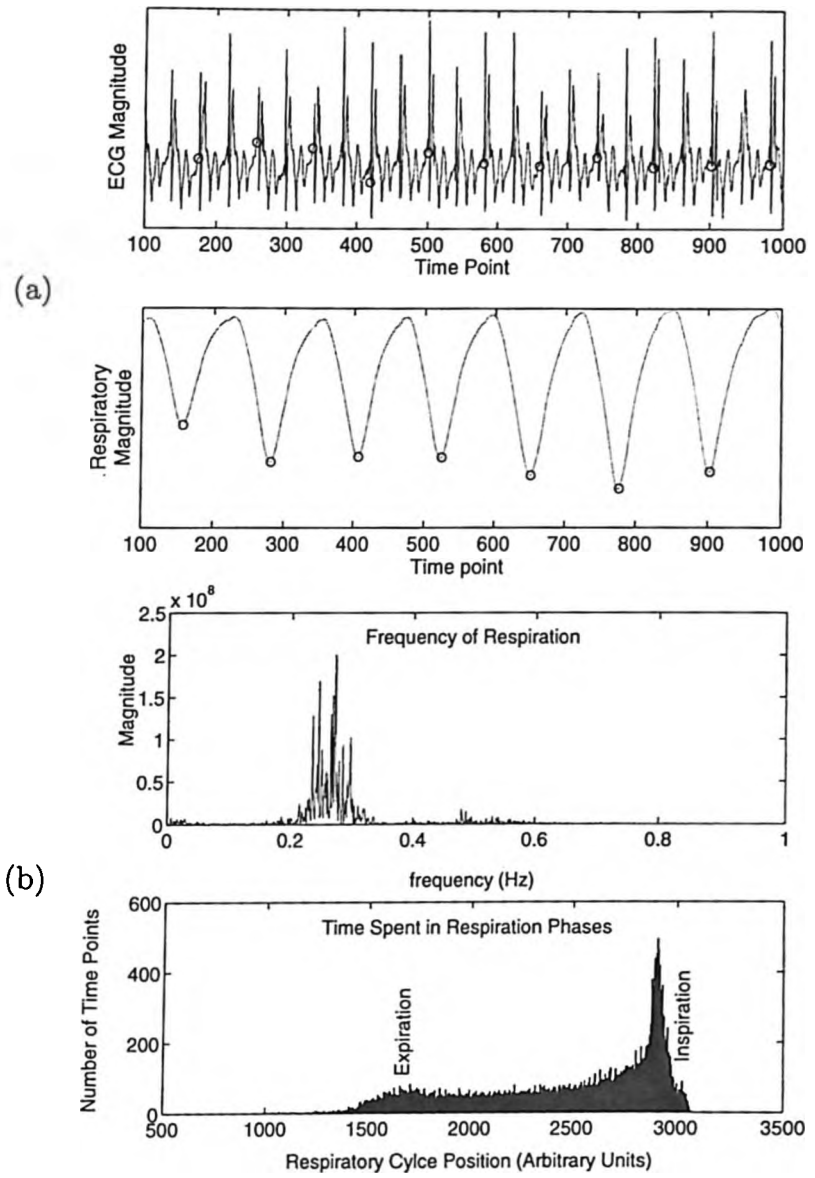

Figure 5.4: (a) Respiratory and cardiac waveforms (b) A fourier spectrum of the Respiratory waveform, and the inspiration

5.3.2 Physiological Motion

Physiological motion, measured using ECG leads and respiratory bellows, was recorded throughout the entire scan. In order to determine the ideal reconstruction position of the respiratory cycle, a histogram of values was plotted, showing time spent along the breathing phases (Figure 5.4). It has been determined that during

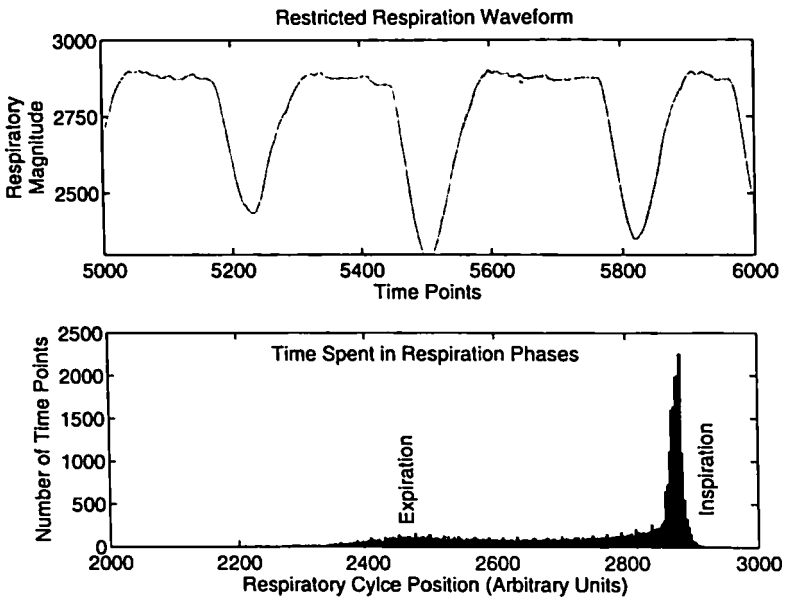

Figure 5.5: The coil restricts some respiratory motion ensuring inspiration was always in the same position. The respiratory bellows was adjusted ensuring good registration within the respiratory cycle before the torso array RF coil was connected together. The amount of time spent in the inspiration phase has increased five fold.

normal breathing the time spent in the inspiration phase is 4 times longer then during expiration. This measurement was used during k-space reconstruction: views collected only in the inspiration phase were reconstructed to produce images with reduced motion artifacts. In an attempt to recover more data the rest of the views were not discarded. Instead the expiration phase was also reconstructed.

In large volunteers the 8 channel torso coil array restricted motion such that the inspiration was observed always at the same point (Figure 5.5). Subjects were asked to breath normally during the scan. The histogram analysis of the data showed that the time spent during inspiration increases 5 fold making it 20 times longer than the expiratory phase. Using a similar technique it might be possible to use a feed back mechanism for subjects to control their breathing pattern.

Collected k-space was reconstructed to produce images in two respiratory phases: inspiration and expiration. Measurements of lung displacement during normal, quiet

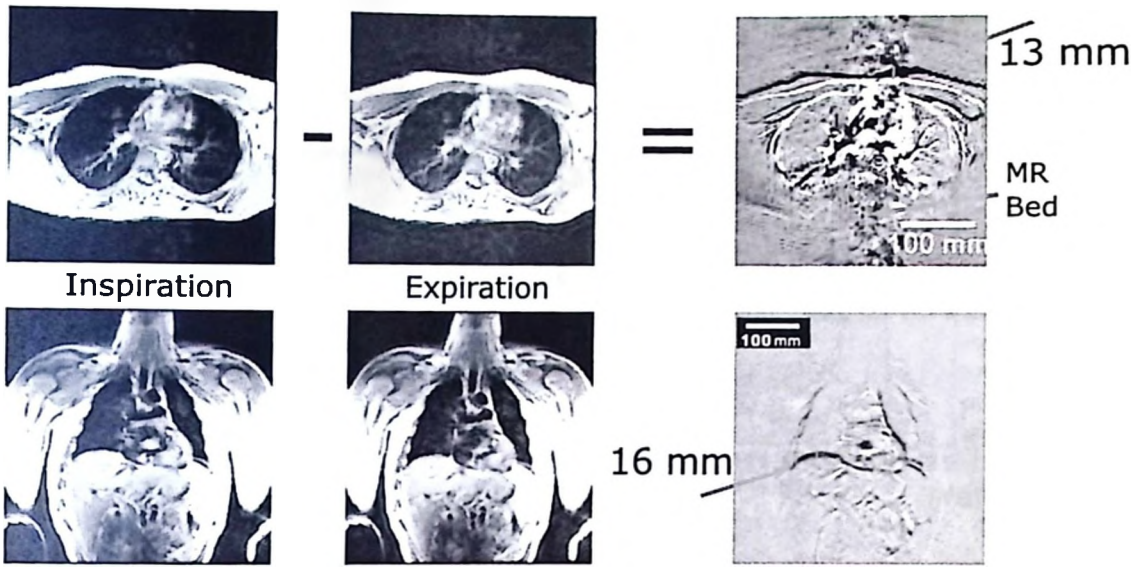

Figure 5.6: Free quite-breathing MR data was acquired coronally and axially. Data was reconstructed producing images during inhalation and expiration phases. Subtracted images show distinct motion, predominant in the anterior direction. This was expected since no motion can occur posteriorly because the subject was laying on the MRI bed. *(Note: subtraction is not perfect because the images are reconstructed with different NEX).*

breathing were performed in axial and coronal views. Images reconstructed in the exhalation phase were subtracted from images from the inhalation phase, producing an area of dark bands denoting motion. These dark bands are the result of displacement of tissue during respiratory cycle (Figure 5.6). Motion was significantly higher in diaphragm areas and anterior chest wall correlating well with the actual physical motion. From axial images the chest of the subject was displaced on average 9.7±3.6 mm with a maximum of 16 mm. Coronal imaging showed diaphragm displacement of 16±2.9 with a maximum of 20 mm.

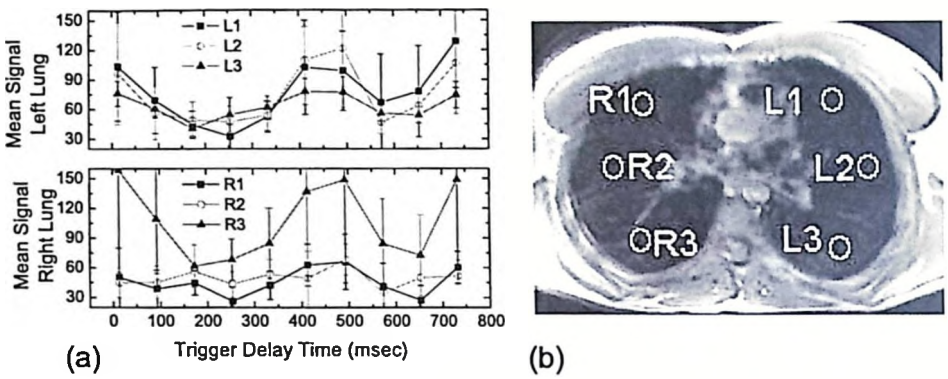

Figure 5.7: Images collected using an ECG gated FSE pulse sequence with varying trigger delays. The zero point of the trigger delay corresponds to the peak of the R wave. Mean subject heart rate during the scan was 70 bpm. MR signal cycling with the cardiac cycle was observed throughout both lungs.

5.3.3 Physical Modulation of Lung MRI Signal.

MR is a unique form of imaging in a sense that you can perform perfusion imaging without the absolute necessity of contrast media. Often these techniques use motion of spins to produce perfusion contrast (section 3.1.3). FSE offers a potential opportunity to image lung perfusion qualitatively. By imaging in various phases of the cardiac cycle MR signal change caused by blood flow was used to assess lung perfusion.

In total eight healthy subjects were scanned at 3.0 Tesla using a ECG gated FSE pulse sequence. Three people were scanned with 6 NEX and 10 phases in the cardiac cycle. For one only 6 cardiac cycle phases were acquired due to subject's request. Five people were scanned with 18 NEX and retrospective gating covering 5 cardiac points. Two out of the five scans had poor ECG signal causing inconsistent and poor triggering rendering data unusable. Two subjects were scanned using a 1.5 Tesla scanner however physiological data was not collected because of the hardware

and pulse sequence incompatibility. One of the subjects was scanned using SE with respiratory compensation over a 5 cardiac cycle points.

Ghosting due to respiratory and cardiac motion was observed in all scans. In several scans some images were predominately corrupted with motion artifacts throughout the lungs making the analysis impossible (those image were discarded). Only in two subjects was between-scan motion severe enough that images had to be realigned.

Signal changes during systole and diastole were observed throughout both lungs, (Figure 5.7). Lung signal change was compared to the signal change in muscle and background (Figure 5.8). Correlation was observed only between lung signal and cardiac cycle. No significant signal change was observed in muscle throughout the cardiac cycle. Background signal was dominated by noise and ghosting thus signal change was sporadic.

Qualitative perfusion images were obtained with two imaging techniques, spin echo and fast spin echo at both 1.5 and 3T. For all cases images collected in systole were subtracted from those in diastole(Figure 5.9(b,d)). Percent difference between the signal in systole compared to diastole was similarly done using Eq. 5.1 (Figure 5.9(a,c) and Figure 5.10). Lung parenchyma was better delineated compared to simple subtraction. Integrating over the entire cardiac cycle improved lung visibility substantially. For all methods 3T, with its improved SNR was superior at showing lung tissue. Spin echo, although slower in acquisition, did not show appreciable difference compared to FSE at either field strength.

Qualitative perfusion images were obtained by three methods. The first technique involved subtraction of images collected in a systole from images collected in diastole (Figure 5.9b). The second method involves calculating the percent signal change between diastole and systole images (the later was calculated using Eq. 5.1, produced

images are shown in Figure 5.9(a,c) and Figure 5.10). The third method involved pixel wise integration throughout the cardiac cycle to produce perfusion images (5.9d). Images collected on a 1.5 Tesla scanner were evaluated in a similar manner (Figure 5.11). Correlation between signal change and cardiac cycle was observed only in the lung tissue (Figure 5.11a). Perfusion images were produced from spin echo pulse sequence data (Figure 5.11c) and fast spin echo pulse sequence (Figure 5.11d).

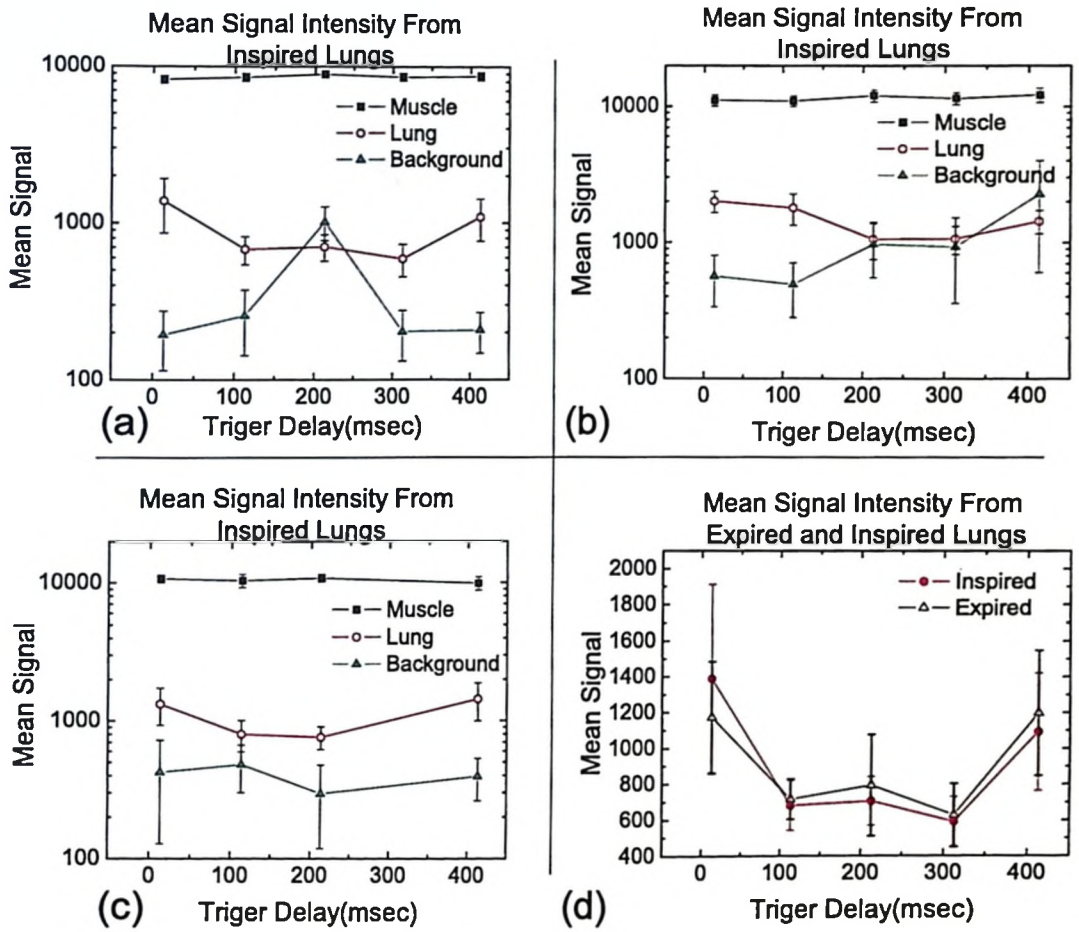

Figure 5.8: Signal change in muscle, lung and background with trigger delay.
(a-c) Data reconstructed in the inspiration phase for three subjects on 3.0 Tesla scanner. No correlation between the signal change in muscle and background was found, however it is clearly observed in the signal change in lungs as a dip around 200 msec after the trigger delay. The mean heart rates for subjects a,b and c during the scan were 64, 70 and 70 respectively.
(d)MR signal change with cardiac phase during inspiration and expiration were found to be similar. The ROI was placed in the same location of the two reconstructed data sets.

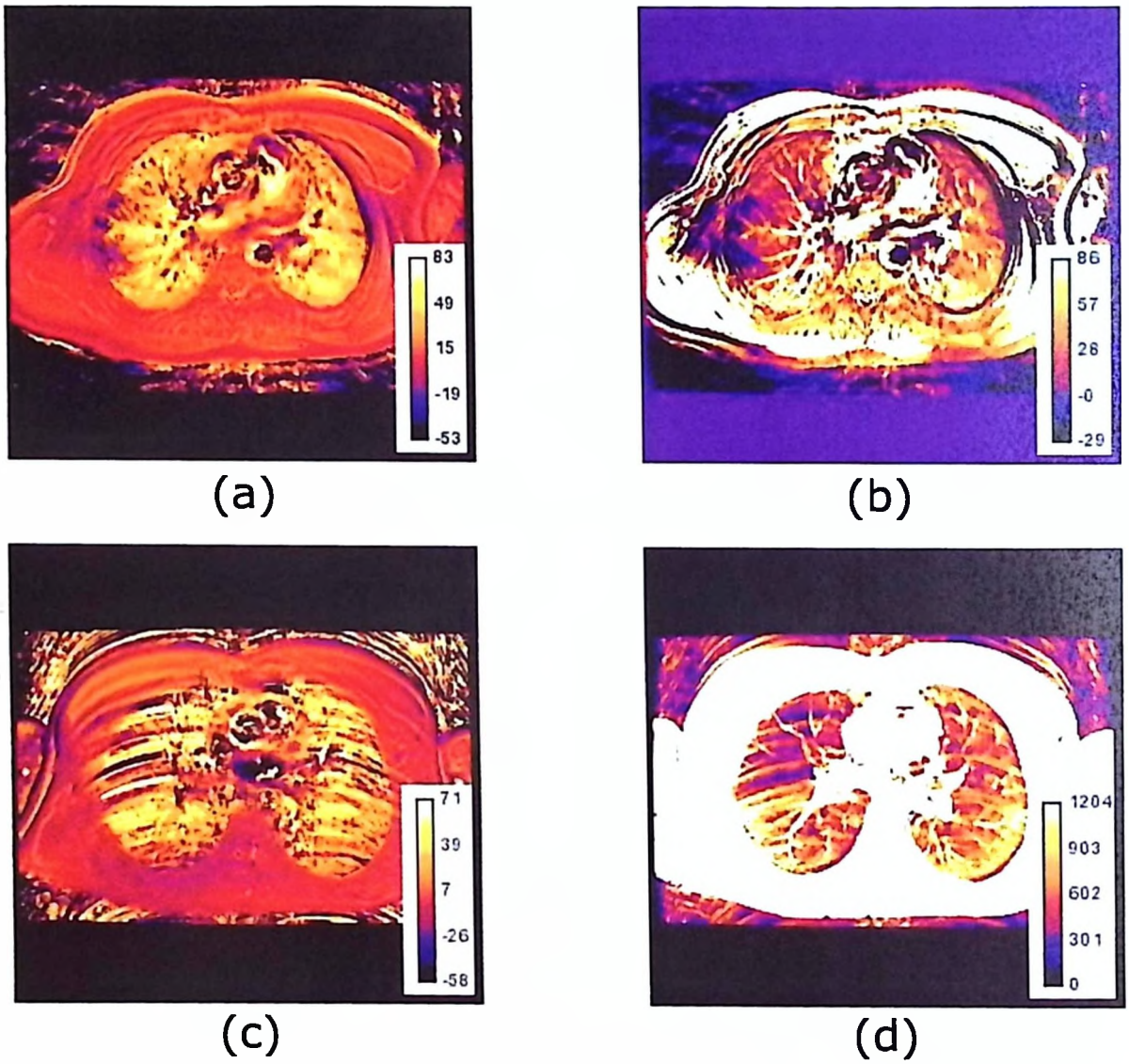

Figure 5.9: Qualitative perfusion images at 3 Tesla.
(a,b) Subject 1 (a) Percent signal change between diastole and systole. Calibration bar units are in percent signal change. (b) Subtraction image diastole minus systole.
(c,d) Subject 2 (c) Percent signal change between diastole and systole. Calibration bar units are in percent signal change. (d) Integral image through the entire cardiac cycle. Subtraction image (b) and integral image (d) show better vasculature then percent signal change images (a,c). Data from both subjects was reconstructed without using retrospective gating.

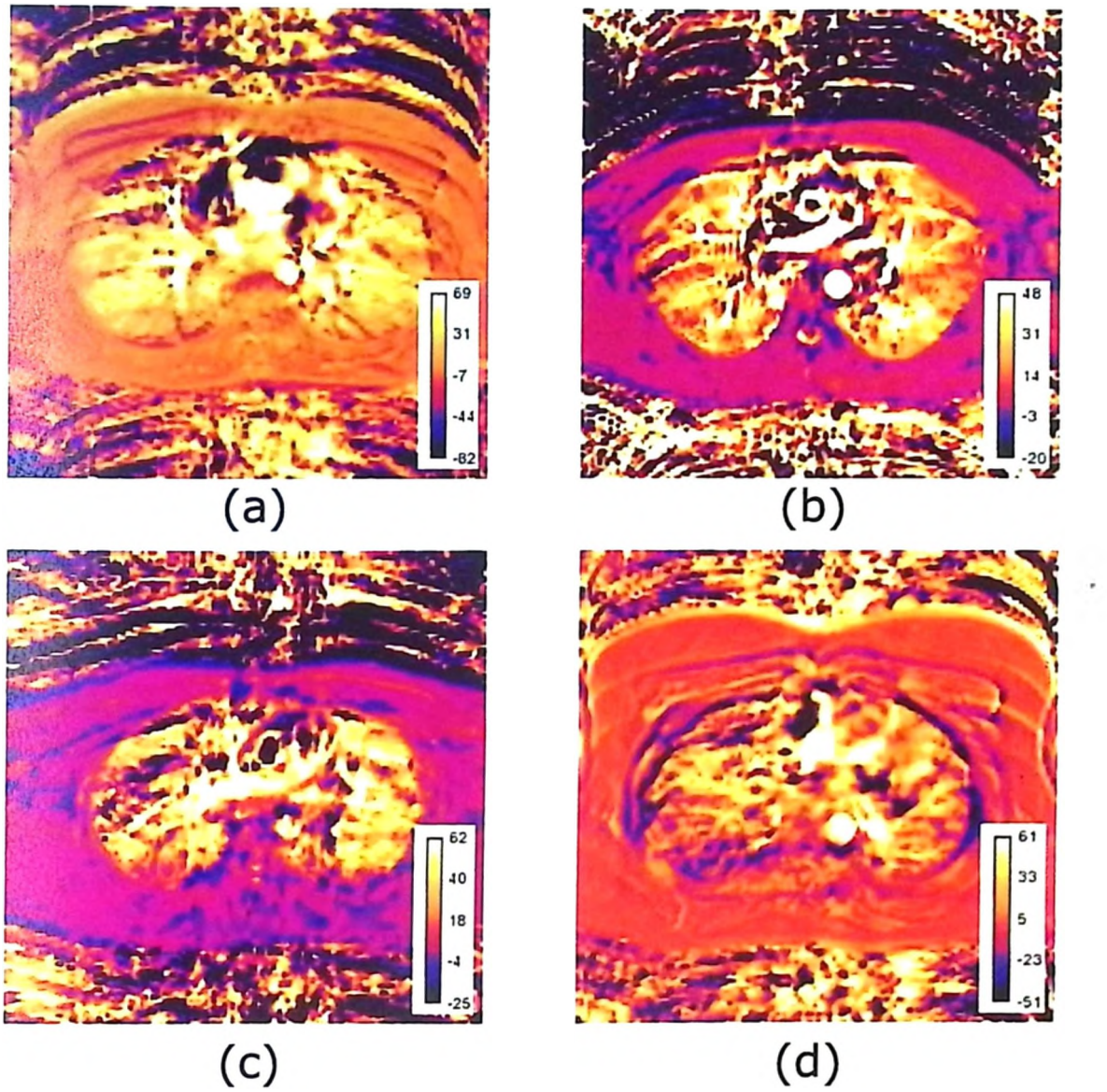

Figure 5.10: Qualitative perfusion images shows percent signal change between systole and diastole images collected using an ECG gated FSE pulse sequence at 3.0 Tesla. Images are for 4 different subjects reconstructed to 128×128 pixels, with motion retrospective gating. The percent signal change in images was not scaled to any one value thus muscle shows up as different colors.

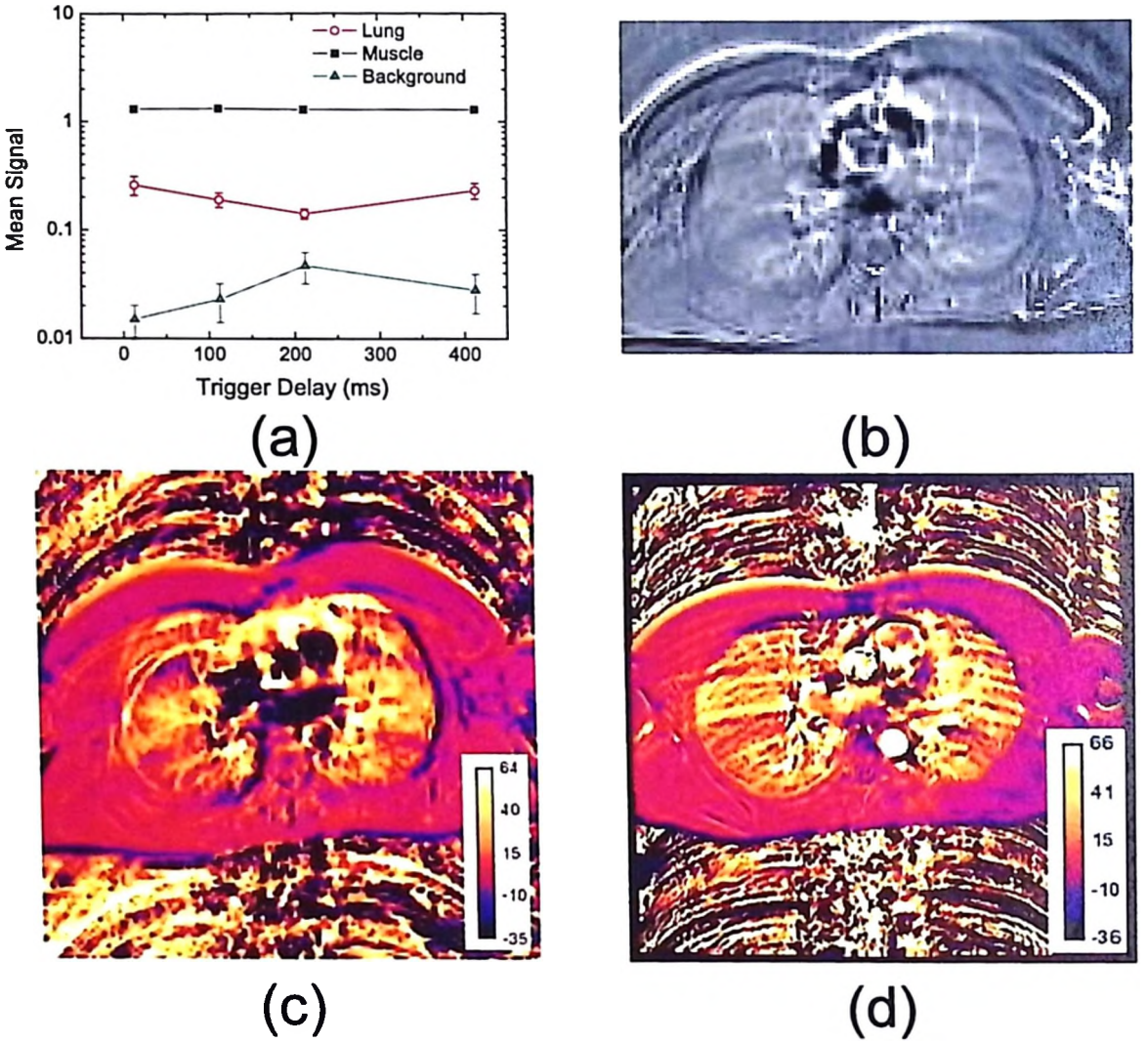

Figure 5.11: (a) Signal change in muscle, lung and background with trigger delay at 1.5 Tesla (Subject 1). (b) Perfusion image calculated by subtracting images in systole from images in diastole. (Subject 1) (c) Percent signal change perfusion image calculated from diastole and systole images collected using ECG gated FSE sequence (Subject 1). (d) Percent signal change perfusion image calculated from SE with respiratory compensation sequence (Subject 2). ECG gated FSE data reconstructed from k-space set without retrospective gating as no physiological data was recorded at 1.5 Tesla.)

5.4 Contrast Enhance Magnetic Resonance Angiography (CEMRA)

This section describes data collected using contrast agent dependent (Gd-DTPA-BMA) perfusion imaging. Here a breath holding technique was used to eliminate respiratory motion. This technique,a minimally invasive procedure, does not use cardiac gating, thus heart motion artifacts are present in the images.

Contrast enhanced images were collected using two pulse sequences: EC-TRICKS and SPGR. The scans were performed during a single breath hold, throughout first passage of the contrast through the lungs. In total 10 scans with the use of a contrast agent were performed 8 of which were performed at 3.0 T. In an attempt to correlate FSE and CEMRA images all of the scans except one were performed axially in order to match the scan plane that FSE images were acquired in. SPGR and EC-TRICKS scans were performed in the same subject, with SPGR first in order to time the bolus. The signal intensity vs time curves are shown in Figure 5.12. The signal peak was observed at 15 seconds for both scans. This arrival time was used to estimate bolus arrival window for the EC-TRICKS pulse sequence. In addition the magnitude and peak area were comparable between methods.

All axial EC-TRICKS images suffered significantly from flow and cardiac motion artifacts. Three out of eight EC-TRICKS axial scans had significant respiratory motion due to subject's inability to hold their breath steady during the scan. Coronal images did not suffer from flow artifact in either SPGR or TRICKS pulse sequences. Axial and coronal perfusion maps, were calculated by measuring time to peak and positive enhancement integral (Figure 5.14).

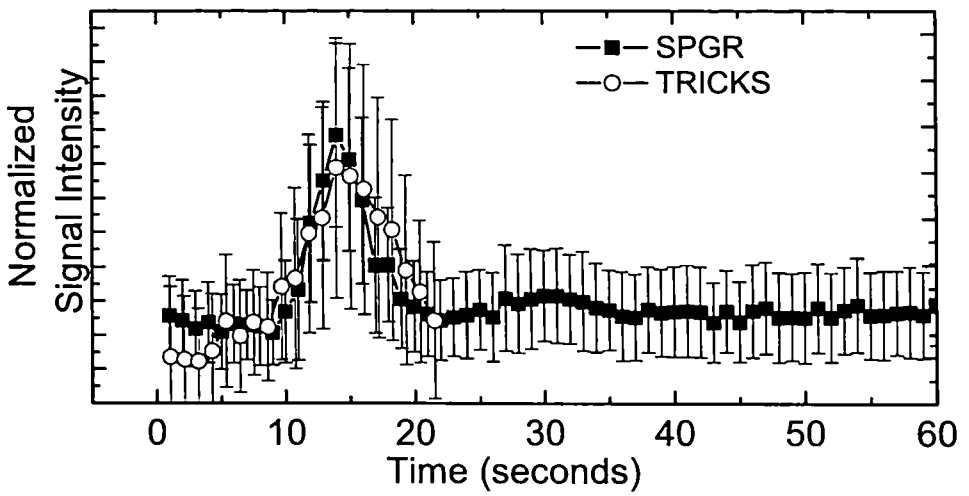

Figure 5.12: Signal change due to contrast. Scans were performed in the same subject using 10 cc of Gd for each scan.

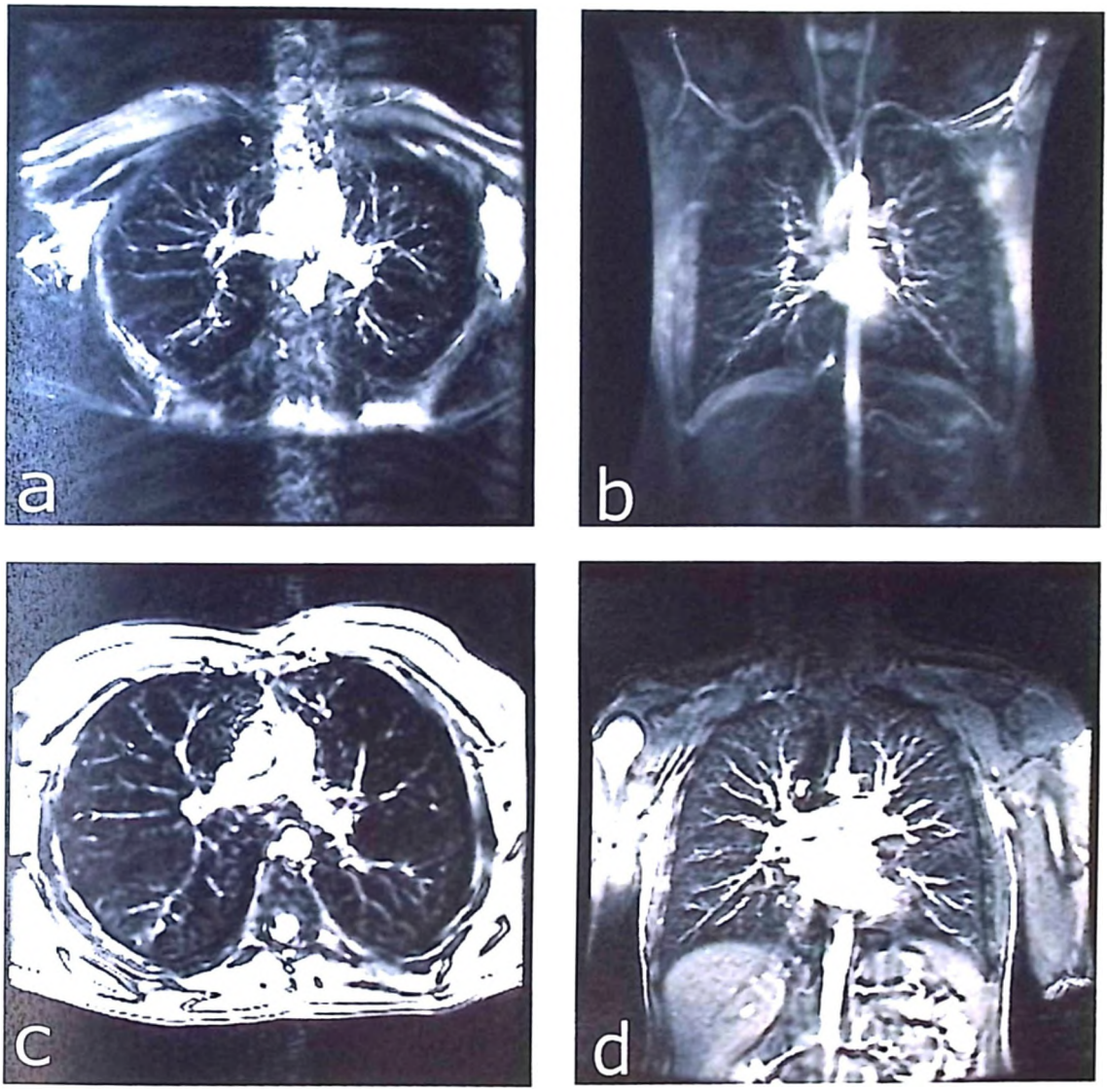

Figure 5.13: For all subjects the peak of the Gd bolus was observed arriving in the lungs in 15 to 20 seconds.
(a) Axial EC-TRICKS on 3T
(b) Coronal EC-TRICKS on 3T
(c) Axial SPGR on 3T
(d) Coronal SPGR on 1.5T

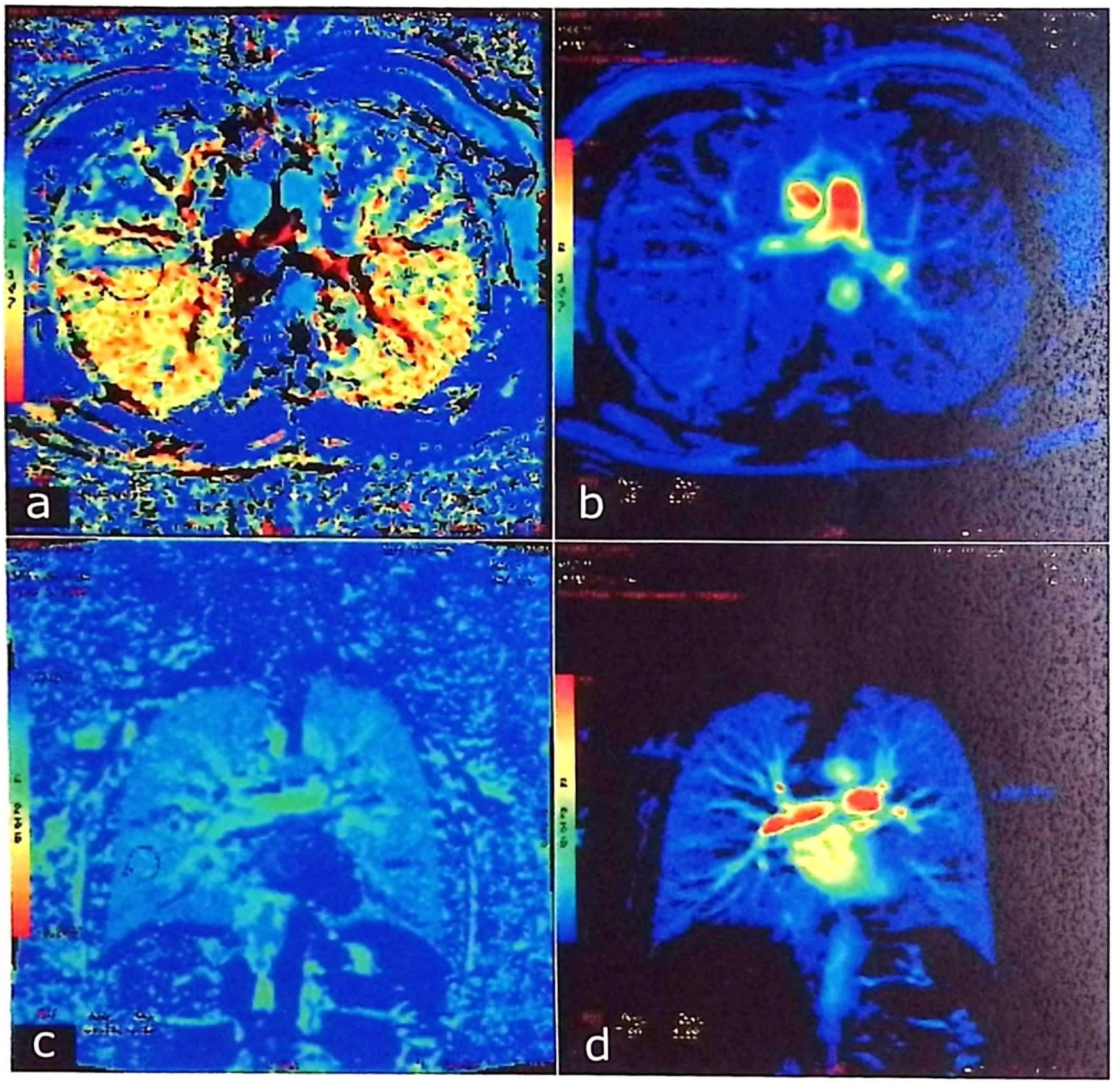

Figure 5.14: Gd enhanced perfusion maps calculated from SPGR images using Functool2 software.
a) Axial Map of Time to Peak 3.0 T
b) Axial Map of Positive Enhancement Integral 3.0 T
c) Coronal Map of Time to Peak 1.5 T
d) Coronal Map of of Positive Enhancement Integral 1.5 T

5.5 Relaxometry Measurements of Gd-DTPA-BMA at 3.0 and 1.5 T in Saline

Figure 5.15(a) shows inversion recovery relaxation curves produced using a SE-IR pulse sequence. Measurements of T_1 were performed by fitting Eq. 4.6 to 25 data points. Two phantoms were used in the experiments. For measurements at room temperature 9 different concentrations of Gd-DTPA-BMA were used varying concentration from 0.5 to 10 mM. While the experiments performed at 37°C used 18 different mixtures varying in concentration from 0.05 to 6 mM.

Relaxometry measurements were performed and compared to the current literature values known for 1.5 Tesla. Experiments were performed at room temperature (20±1°C) and 37±0.1°C. Relaxation, R_1, for Gd-DTPA-BMA at 1.5T was $4.06\pm0.3(mM \cdot s)^{-1}$ at room temperature (Figure 5.15b). Published work by Reichenbach et al. (1997), relaxivity values at 1.5 T of Gd-DTPA-BMA in deionized water, were reported to be $4.59(mM \cdot s)^{-1}$ at 23°C.

The higher field strength and higher temperature decreased relaxation potency of the Gd-DTPA-BMA as expected. Experiments at room temperature were performed using two pulse sequences at 3 Tesla. Spin echo with inversion recovery and fast spin echo with inversion recovery pulse sequences were used to perform T_1 measurements (Figure 5.15c,d). The two pulse sequences showed comparable results within 1% discrepancy of each other (Figure 5.15e). For the temperature experiments a FSE-IR pulse sequence was used in order to minimize temperature fluctuations that could occur during long scan times. The relaxivity of Gd-DTPA-BMA at 37°C and 3T decreased to $3.35\pm0.09(\text{mM} \cdot \text{s})^{-1}$ (Figure 5.15f).

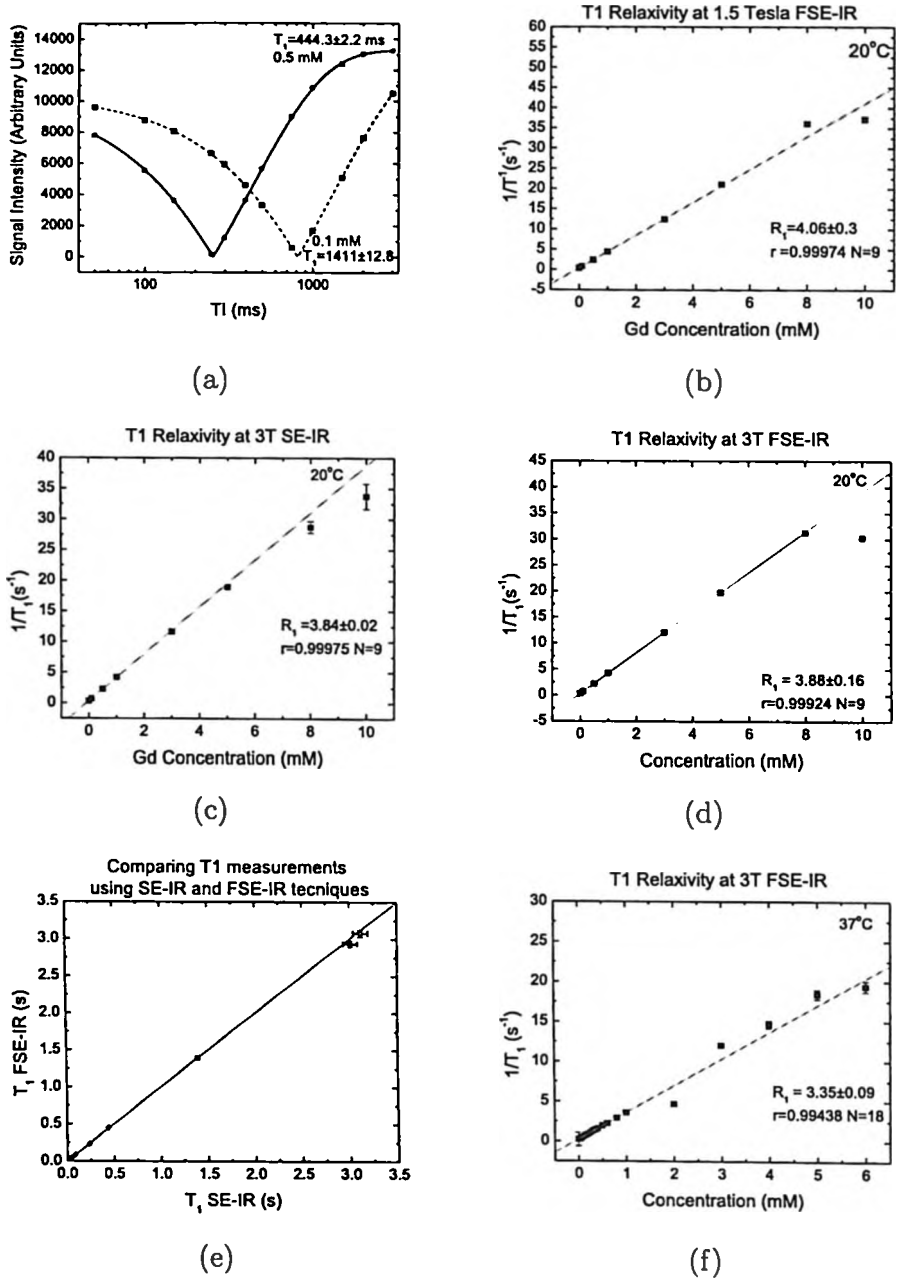

Figure 5.15: R_1 relaxation measurements of Gd-DTPA-BMA at 1.5T and 3T
a) Typical relaxation curves measured at by varying inversion time. Two concentrations of Gd-DTPA-BMA are shown 0.1 mM and 0.5 mM. A 25 point fit using Levenberg-Marquardt algorithm was performed for each concentration of Gd-DTPA-BMA. b)Relaxometry measurements at 1.5 Tesla (20°C) using FSE-IR. c)Relaxometry measurements at 3.0 Tesla (20°C) using SE-IR. d)Relaxometry measurements at 3.0 Tesla (20°C) using FSE-IR. e)Direct comparison of SE-IR and FSE-IR T_1 measurements by plotting T_1 values measured by two pulse sequences. f)Relaxometry measurements at 3.0 Tesla (37°C) using FSE-IR.

Table 5.5: Both increased temperature and increased field strength(B_o) act to decrease R_1. Summary of relaxivity values for GD-DTPA-BMA in saline.

R_1 $(mM \cdot s)^{-1}$	Field (Tesla)	Temperature (^oC)	Pulse Sequence
4.06±0.3	1.5	20	Fast SE IR
3.84±0.02	3.0	20	SE IR
3.88±0.16	3.0	20	Fast SE IR
3.35±0.09	3.0	37	Fast SE IR

Chapter 6

Discussion

In this thesis I have clearly demonstrated that proton based lung imaging can be performed successfully at 3.0 Tesla. The increased magnetic field strength above typical clinical scanners of 1.5 T does bring advantages when applied to lung perfusion imaging. This advantage could be used to study normal and diseased pulmonary hemodynamics (e.g. pulmonary hypertension, stenosis) and parenchymal lung diseases. Because there is a very close relation between cardiac output and pulmonary function, blood flow can act as a contrast agent. The ability to image the entire lung, building a complete picture consisting of perfusion, ventilation and structural information is beyond the scope of this short masters thesis. MR techniques used to image lung ventilation and parenchyma at 3.0 Tesla are not out of reach but rather need further study and optimization.

Successful MR imaging of the lung is highly dependent on the ability to compensate for respiratory and cardiac motion. Two different methods for minimizing motion artifacts have been used in this thesis. The first technique, a free breathing cardiac gated technique relying on blood flow as contrast, is likely more suitable for patients. However free breathing acquisitions required long scan times ($\sim$13 minutes) and thus it becomes more difficult to correct for all respiratory motion. Evaluation of diseased lung images with artifacts could be problematic. The second technique involved Gd-based contrast perfusion combined with breath holding to eliminate respiratory motion. Cardiac motion was not accounted for in this technique, because it

Table 6.1: Percent signal change for 1.5 T are from two subjects measured from 5 ROIs. 3.0 Tesla are measured from 5 subjects 2 ROIs each.

Percent Signal Change	
1.5T	3.0T
39.77	151.28
35.33	202.58
48.49	94.538
31.29	33.128
70.10	77.698
21.29	40.088
77.16	45.548
23.77	91.958
26.86	34.608
83.09	84.048

is critical to time image acquisition and contrast arrival correctly to produce useful results. Two techniques both bring certain advantages and disadvantages to the field of lung perfusion imaging. The Gd-based imaging offers increased signal and significant clinical value if done properly. The non contrast based method offers a great deal of information not only on perfusion but also pulmonary hemodynamics.

The variation of flow and MR signal during the cardiac cycle is complex but well understood (reviewed by Bernstein et al. (2004); Haacke et al. (1999)). In a recent report by Miyazaki et al. (2000) variation in MR signal with cardiac phase was shown in ascending and descending aorta, and superior vena cava at 1.5 Tesla. An 85% signal increase between blood velocity of 60 and 10 cm/s was measured using a half Fourier FSE pulse sequence. As the pulmonary artery branches into smaller vessels lung blood velocity decreases. In another study mean pulmonary blood flow of 11.0±2.1 cm/s through the pulmonary trunk, in resting healthy individuals, was measured compared to significantly increased blood flow (20.5±3.0 cm/s) in patients with pulmonary hypertension (Saro et al. 2001). Achievement of more accurate blood flow signal can lead to better differentiation between healthy and diseased lungs. FSE

experiments showed lung signal increase of 85.55±55.0% at 3.0 Tesla between, systolic and diastolic phases. Mean signal change between systole and diastole for 1.5 T was 45.72±23.03% (Table 6.1). Using a Student's t-test to compare percent signal change between the two MRI systems gives $t(9)=2.43$, $p = 0.037$ suggesting that 3.0 Tesla is more sensitive to signal changes due to blood flow than 1.5 Tesla. In order to perform a scan of the entire cardiac cycle however with sufficient SNR (through increased NEX), up to 13 minutes per data point is required, making it hard to observe signal change throughout the entire cardiac cycle. A faster way to measure blood flow is through the use of cine phase-contrast (Kellenberger et al. 2005). However the perfusion maps in this thesis were produced using only two points: one in systole and one in diastole thus requiring only two scans (Figure 5.9, 5.10).

In another experiment data was collected throughout the entire cardiac cycle with 80ms temporal resolution(Figure 5.7, Figure 6.1). The MR signal change across the cardiac cycle can be summarized as; the faster blood flows the more MR signal decreases. A detailed physiological explanation is as follows: The ECG QRS complex marks the end of atrial systole and beginning of ventricular systole. Subsequently isovolumetric contraction of the heart ventricles followed by rapid ejection of blood occurs (Figure 6.1a). The end of systole is marked by the T wave, during which reduced ejection of heart blood occurs (Figure 6.1b). The end of the T wave marks the beginning of diastole, where ventricular volume is at a minimum (isovolumetric relaxation; Figure 6.1c). When ventricular pressure drops valves open and the blood accumulated in the atria flows rapidly into ventricles (Figure 6.1d). The filling slows until the ventricles are full (Figure 6.1e). The beginning of the P wave marks the end of diastole. The observed MR signal change with the cardiac cycle correlates well with physiology. The first dip shown in Figure 6.1a-b is most likely due to blood

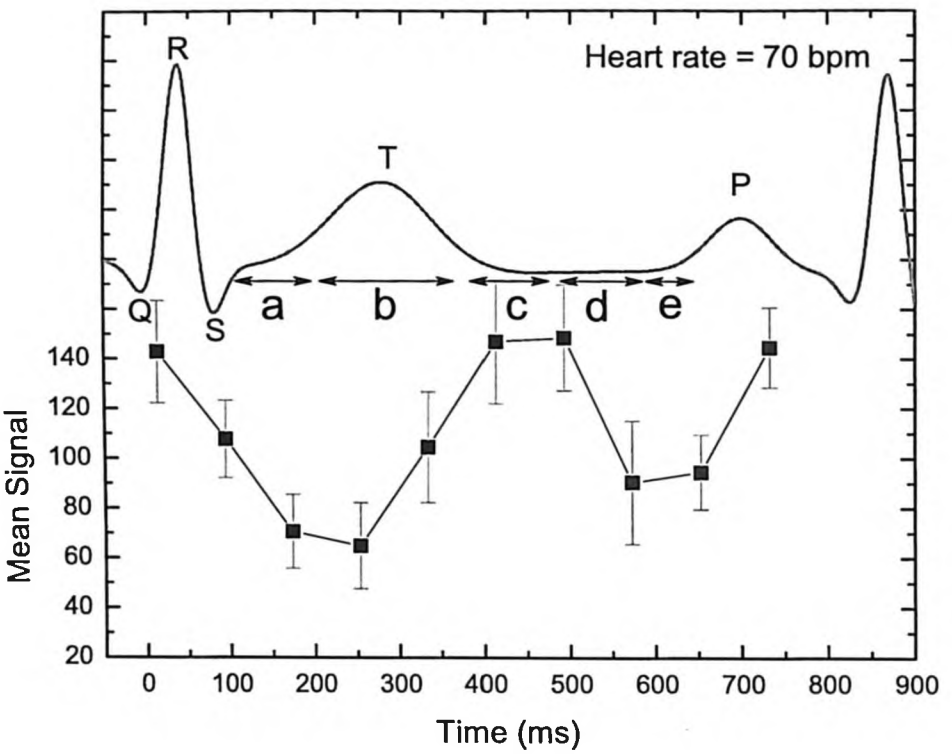

Figure 6.1: MR signal change due to cardiac cycle.
a) Rapid Ejection
b) Reduced Ejection
c) Isovolumetric Relaxation
d) Rapid Ventricular filling
e) Reduced Ventricular filling

flowing away from the heart. The second dip (Figure 6.1d-e) is speculated to be due to blood returning flow to the heart which is slower and thus smaller in appearance.

Ogasawara et al. (2004) also observed a similar dip of the MR signal during diastole in healthy subjects, however no explanation was given to its origin. Further, (Ogasawara et al.), showed the signal change between diastole and systole differs between diseased and healthy lung. However the authors made no observations to

correlate the entire cardiac cycle with MR signal. From a technical point of view development of this non-contrast technique into a powerful imaging modality to evaluate lung disease will require a faster imaging method that is economical yet provides maximal patient comfort. In addition SAR (specific absorption rate) must be considered as this becomes a potential problem when trying to image the entire lungs at 3 Tesla; multi-slice imaging must be done carefully to get a high deal of coverage without over heating the patient.

Application of Gd for perfusion and MRA is a powerful method already shown as enhanced at 3.0 Tesla. Finn and Laub (2004) suggested resolution of pulmonary MR angiography at 3T is similar to CT angiography. Perfusion images produced using Gd enhancement are of course clinically important. The experiments in this thesis have showed that decreased Gd dose using 3.0T can have similar enhancement as 1.5T with higher dose. To explain this relaxivity modulation spin lattice relaxation rate (R_1) of Gd-DTPA-BMA was measured at both field strengths: spin-lattice relaxivity of Gd decreased with increasing field, as expected. This higher polarization of spins at higher field allows use of lower dose to produce MRA images of comparable quality to full dose at 1.5T. However in order to achieve CT angiography comparable resolution with the higher field system, a higher dose of Gd must be used (Finn and Laub 2004). Axially acquired lung contrast-based perfusion images, done to match non-contrast enhanced images, was not successful as the axial images suffered from flow and cardiac motion artifacts in the phase encoding direction and motion during breath holds resulted in severe subtraction artifacts.

Two MRI pulse sequences were evaluated for performing dynamic contrast enhanced MRI (DCE-MRI) of lung. These perfusion techniques were performed with Gd-DTPA-BMA contrast agent. An elliptic centric time resolved pulse sequence (EC-TRICKS) similar to the keyhole approach, used to capture the arrival of contrast bolus

was coded and used for the first time at 3.0 Tesla. This sequence is typically applied in distal limbs using the advantage of producing a time course of Gd contrast MR angiography images irrespective of different filling rates in (for example) each leg. It does not require accurate timing as other sequences that require a timing bolus, as it is possible to run the pulse sequence continually to capture the start, passage, and ending of the entire bolus. Axially acquired pulmonary angiographic images were of substandard quality. Coronal acquisition was far superior (Figure 5.13). One caveat of EC-TRICKS is the requirement for breath holding (up to 30 seconds), a potential difficulty for individuals with pulmonary disease. The pre-contrast mask and perfusion images must all be acquired during the same breath hold. Failure of this complete acquisition results in subtraction error and data miss-registration. It is not possible for a subject to perform the identical breath hold twice. Performing mask and contrast images on successive breath holds was attempted on one subject as a test. However the reconstructed images were of very poor quality largely due to subtraction errors. Even some of the healthy subjects were not able to hold their breath during this study, resulting in motion artifacts in subtracted images. Another disadvantage of EC-TRICKS is temporal resolution is sacrificed for spatial resolution, and vice versa. Ideally high resolution images would be clinically more useful but they require precise timing of the bolus to the tissue. More work is required to optimize this acquisition scheme as bolus timing varies largely from person to person.

A SPGR pulse sequence was also used as a DCE-MRI procedure. This sequence offers more T_1 weighting then other gradient echo based pulse sequences. As with EC-TRICKS axial images were also contaminated with flow and motion artifacts in the PE direction (Figure5.13c). Coronal images were superior, as with EC-TRICKS. However the biggest difference between the SPGR and EC-TRICKS pulse sequences is that instead of performing high resolution MR angiography, SPGR images a bolus pass

that can be tracked almost in real time with 1 second temporal resolution. Perfusion maps are routinely processed using this approach by evaluating signal change with time: parameters such as bolus mean transit time (MTT), time to peak (TTP), and enhancement integral can by used to evaluate Gd-bolus based perfusion (Figure 4.9). Perfusion mapping was calculated using Functool2 software (Advantage Windows workstation 4.2, GE Healthcare) (Figure 5.14). The TTP, measured axially, at 3.0T, was reduced in the posterior positions of the lungs. This is explained physiologically through the elastic nature of lungs acting as a spring that is influenced by gravity. The top of the "spring" would be expanded further than the bottom because the top has mass pulling (stretching) it downward as the subject lies on the MRI bed. Similarly posterior lung tissue is more compressed under its own weight, resulting in greater blood volume and thus a faster bolus TTP.

Correlation of perfusion techniques (contrast vs non-contrast approaches) has proved to be difficult as there is was no gold standard, reference, or model to work from. Perfusion defects were not observed by in any of healthy subjects. Similar signal change was observed between non-contrast and contrast based methods (Figure 6.2). Lutterbey et al. (2005) reported successful evaluation of diffuse lung disease on 3.0 Tesla using a T_2 weighted FSE sequence. Their findings were similar to "gold standard" CT lung images. However only gross changes in lung morphology were visible and healthy normal lung appeared dark. In order to perform further evaluation of MR lung imaging it is necessary to have a disease model to work with.

In this thesis proton based lung MR imaging was applied in an attempt to image ventilation and parenchyma. Proton based ventilation imaging however is still very much in development. Both oxygen and nebulized Gd have been shown at 1.5T to barely achieve contrast needed to evaluate ventilation. These techniques require multiple breath holds and a long inhalation time of the contrast agent (10 minutes) in

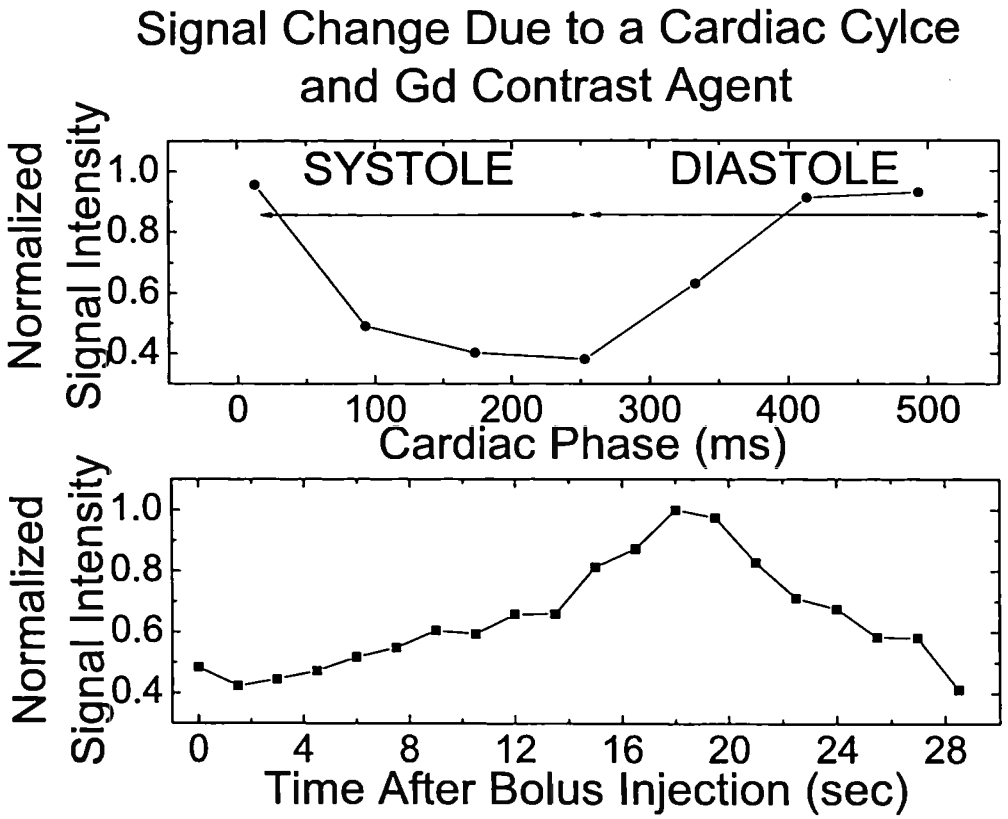

Figure 6.2: Signal change in the lungs during cardiac cycle and signal change due to bolus injection of the contrast agent. Comparable absolute signal magnitude changes were observed through the entire lung from both methods, although the methods differ temporally.

order to see enhancement (Haage et al. 2003). For breath held imaging a breathing maneuver can be used to try and insure the same breath hold pattern throughout the studies. However these are difficult to achieve perfectly and likely excessively problematic for the general clinical population. A potential downside of Gd-DTPA-BMA as a ventilation agent is this is an off-label use and has not been clinically tested for side effects.

Tests with TRICKS for ventilation assessment was sensible with it's centric ordered acquisition and short TE. Unfortunately signal change from image to image

varied greatly, due to bulk tissue motion. Again, averaging signal from multiple breath holds made this approach unusable. Nonetheless optimization of flip angle, and acquisition possibly using the MVA could lead to applicability of this method for lung ventilation assessment at 3T. The SPGR pulse sequence was also an attempt to image lung full volume rapidly in a single breath hold. Mismatch due to breath holds did not produce any significant enhancement. A better way to image ventilation however could be to use T_1 or T_2 mapping pulse sequences. There is no reason why proton ventilation imaging is not possible at 3.0T and more studies need to be performed to achieve a successful ventilation protocol.

In summary lung imaging at 3.0 Tesla is possible and was demonstrated for contrast and non-contrast perfusion imaging. Two techniques differ temporarily yet produce similar results. Contrast enhanced imaging was used to produce perfusion maps and MR angiography images. It was found that a reduced dose of contrast agent at 3.0 Tesla produced images comparable to full dose at 1.5 Tesla. For high resolution contrast enhanced MR angiography a higher dose and optimized EC-TRICKS pulse sequence parameters are needed. In addition a technique for timing the bolus needs development. Non-contrast perfusion performed better at 3.0 Tesla as higher fields provide enhanced sensitivity to flow and thus increase percent signal enhancement. However in order to evaluate which perfusion technique is more clinically valuable a study involving a diseased population is necessary.

Bibliography

Ailion, D., T. Case, D. Blatter, A. Morris, A. Cutillo, C. Durney, and S. Johnson (1984). Application of NMR spin imaging to the study of lungs. *Bull Magn Reson 6*, 130–139.

Albertine, K. (1996). *Structural organization and quantitative morphology of the lung.In: Cutillo A.G. (ed.) Application of Magnetic Resonance to the Study of Lung.* Futura Publishing Co, Inc.

Alsop, D., H. Hatabu, M. Bonnet, J. Listerud, and W. Gefter (1995). Multi-slice, breathhold imaging of the lung with submillisecond echo times. *Magn Reson Med. 33*(5), 678–82.

Ardenkjaer-Larsen, J., B. Fridlund, A. Gram, G. Hansson, L. Hansson, M. Lerche, R. Servin, and et.al. (2003). Increase in signal-to-noise ratio of >10,000 times in liquid-state NMR. *PNAS 100*(18), 10158–10163.

Bader, T., R. Semelka, M. Pedro, D. Armao, M. Brown, and P. Molina (2002). Magnetic resonance imaging of pulmonary parenchymal disease using a modified breath-hold 3d gradient-echo technique: Initial observations. *J Magn Reson Imaging 15*, 31–38.

Bergin, C., G. Glover, and J. Pauly (1991). Lung parenchyma: magnetic susceptibility in mr imaging. *Radiology 180*, 845–848.

Bergin, C., D. Noll, J. Pauly, G. Glover, and A. Macovski (1992). MR imaging of lung parenchyma: a solution to susceptibility. *Radiology 183*(3), 673–6.

Bergin, C., J. Pauly, and A. Macovski (1991). Lung parenchyma: projection reconstruction MR imaging. *Radiology 179*(3), 777–81.

Berne, R. and M. Levy (1993). *Principles of Physiology*, Chapter The cardiac pump., pp. 397416. St Lois: Mosby, Inc.

Bernstein, M. A., K. F. King, and X. J. Zhou (2004). *Handbook of MRI Pulse Sequences*. Elsevier Academic Press.

Berthezene, Y., P. Croisille, M. Wiart, N. Howarth, C. Houzard, O. Faure, P. Douek, M. Amiel, and D. Revel (1999). Prospective comparison of MR lung perfusion and lung scintigraphy. *J Magn Reson Imaging 9*(1), 61–8.

Bottomley, P. A., R. W. Redington, W. A. Edelstein, and J. F. Schenck (1985). Estimating radiofrequency power deposition in body NMR imaging. *Magn Reson Med 2*(4), 336–49.

Case, T., C. Durney, D. Ailion, A. Cutillo, and A. Morris (1987). A mathematical model of diamagnetic line broadening in lung tissue and similar heterogenous systems: calculations and measurements. *J Magn Reson 73*, 304–314.

Constantinides, C. D., E. Atalar, and E. R. McVeigh (1997). Signal-to-noise measurements in magnitude images from NMR phased arrays. *Magn Reson Med 38*(5), 852–7.

Cutillo, A., K. Ganesan, D. Ailion, A. Morris, C. Durney, S. Symko, and R. Christman (1991). Alveolar air-tissue interface and nuclear magnetic resonance behavior of lung. *J Appl Physiol 70*, 2145–2154.

Cutillo, G. and D. Ailion (1999). Modeling the nuclear magnetic resonance behavior of lung: From electrical engineering to critical care medicine. *Bioelectromagnetics 20*, 110–119.

Du, Y., E. McVeigh, D. Bluemke, H. Silber, and T. Foo (2001). A comparison of prospective and retrospective respiratory navigator gating in 3d mr coronary angiography. *The International Journal of Cardiovascular Imaging (formerly Cardiac Imaging) 17*(4), 287–294.

Durney, C., D. Ailion, and A. Cutillo (1996). *Susceptibility effects (tissue-induced inhomogenous broadening) in lung magnetic resonance imaing. In: Cutillo AG (ed) Application of Magnetic Resonance to the Study of Lung.* Futura Publishing Co, Inc.

Durney, C. H., H. Massoudi, and M. F. lskander (October 1986). *Radiofrequency Radiation Dosimetry Handbook. 4th Edition.* Electrical Engineering Department The University of Utah Salt Lake City, UT 84112.

Edelman, R. R., H. Hatabu, E. Tadamura, W. Li, and P. V. Prasad (1996). Non-invasive assessment of regional ventilation in the human lung using oxygen-enhanced magnetic resonance imaging. *Nat Med 2*(11), 1236–9.

Finn, P. and G. Laub (2004). Contrast enhanced mr angiography of the pulmonary circulation at 3.0t: Initial experience with a phased array coil. *Proc. Intl. Soc. Mag. Reson. Med. 11*, 672.

Golman, K., J. H. Ardenkjaer-Larsen, J. S. Petersson, S. Mansson, and I. Leunbach (2003). Molecular imaging with endogenous substances. *Proc Natl Acad Sci U S A 100*(18), 10435–9.

Golman, K., J.-H. Ardenkjaer-Larsen, J. Svensson, O. Axelsson, G. Hansson, L. Hansson, H. Johannesson, I. Leunbach, S. Mansson, J. S. Petersson, G. Pettersson, R. Servin, and L.-G. Wistrand (2002). 13C-angiography. *Acad Radiol 9 Suppl 2*, S507–10.

Gorter, C. (1936). Negative results of an attempt to detect nuclear magnetic spins. *Physica 3*, 503.

Haacke, E. M., R. W. Brown, M. R. Thompson, and R. Venkatesan (1999). *Magnetic Resonance Imaging: Physical Principles and Sequence Design.* Wiley-Liss.

Haage, P., G. Adam, S. Karaagac, J. Pfeffer, A. Glowinski, S. Dohmen, and R. Gunther (2001). Mechanical delivery of aerosolized gadolinium-dtpa for pulmonary ventilation assessment in mr imaging. *Investigative Radiology 36*(4), 240–243.

Haage, P., S. Karaagac, E. Spuntrup, G. Adam, and R. Gunther (2003). Mr imaging of lung ventilation with aerosolized gadolinium-chelates. *Fortschr Rontgenstr 175*, 187–193.

Halse, M., D. J. Goodyear, B. MacMillan, P. Szomolanyi, D. Matheson, and B. J. Balcom (2003). Centric scan SPRITE magnetic resonance imaging. *J Magn Reson 165*(2), 219–29.

Halse, M., J. Rioux, S. Romanzetti, J. Kaffanke, B. MacMillan, I. Mastikhin, N. J. Shah, E. Aubanel, and B. J. Balcom (2004). Centric scan sprite magnetic resonance imaging: optimization of snr, resolution, and relaxation time mapping. *J Magn Reson Imaging 169*(1), 102–117.

Hatabu, H., D. Alsop, J. Listerud, M. Bonnet, and W. Gefter (1999). T_2^* and proton density measurement of normal human lung parenchyma using submillisecond echo time gradient echo magnetic resonance imaging. *Eur J Radiol 29*(3), 245–52.

Hatabu, H., W. Gefter, H. Kressel, L. Axel, and R. Lenkinski (1989). Pulmonary vasculature: high-resolution MR imaging. Work in progress. *Radiology 171*(2), 391–5.

Hatabu, H., E. Tadamura, Q. Chen, K. Stock, W. Li, P. Prasad, and R. Edelman (2001). Pulmonary ventilation: dynamic mri with inhalation of molecular oxygen. *European Journal of Radiology 37*, 172–178.

Jakob, P., C. Hillenbrand, T. Wang, G. Schultz, D. Hahn, and A. Haase (2001). Rapid quantitative lung 1h t1 mapping. *J Magn Reson Imaging 14*, 795–799.

Johnson, J. R., T. D. Swindle, and P. G. Lucey (1999). Estimated solar wind-implanted helium-3 distribution on the moon. *Geophysical Research Letters 26*(3), 385–388.

Kauczor, H., A. Hanke, and E. van Beek (2002). Assessment of lung ventilation by mr imaging: current status and future perspectives. *European Radiology 12*, 1962–1970.

Keilholz-George, S. (2001). *Quantitative perfusion mapping with arterial spin labeling magnetic resonance imaging.* Ph. D. thesis, University of Virginia.

Kellenberger, C. J., C. K. Macgowan, K. S. Roman, F. Al-Habshan, L. N. Benson, A. N. Redington, and S.-J. Yoo (2005). Hemodynamic evaluation of the peripheral pulmonary circulation by cine phase-contrast magnetic resonance imaging. *J Magn Reson Imaging*.

Knight-Scott, J., S. Keilholz-George, V. Mai, and J. Christopher (2001). Temporal dynamics of blood flow effects in half- fourier fast spin echo 1h magnetic resonance imaging of the human lungs. *J Magn Reson Imaging 14*, 411–418.

Krasnoholovets, V. (2000). On the nature of spin, inertia and gravity of a moving canonical particle. *Indian Journal of Theoretical Physics 48*(2), 97–132.

Kuethe, D., A. Caprihan, H. Gach, I. Lowe, and E. Fukushima (2000). Imaging obstructed ventilation with NMR using inert fluorinated gases. *J Appl Physiol 88*(6), 2279–86.

Larsson, E. G., D. Erdogmus, R. Yan, J. C. Principe, and J. R. Fitzsimmons (2003). SNR-optimality of sum-of-squares reconstruction for phased-array magnetic resonance imaging. *J Magn Reson 163*(1), 121–3.

Laukemper-Ostendorf, S., A. Scholz, K. Burger, C. P. Heussel, M. Schmittner, N. Weiler, K. Markstaller, B. Eberle, H.-U. Kauczor, M. Quintel, M. Thelen, and W. G. Schreiber (2002). 19F-MRI of perflubron for measurement of oxygen partial pressure in porcine lungs during partial liquid ventilation. *Magn Reson Med 47*(1), 82–9.

Lin, Y.-R., M.-T. Wu, S.-Y. Tsai, H.-W. Chung, K.-S. Hsieh, and N.-J. Peng (2004). Comparison of pulmonary perfusion measurement by dynamic contrast-enhanced mri versus perfusion scintigraphy: disagreement and solution. *Proc. Intl. Soc. Mag. Reson. Med. 11*, 675.

Lutterbey, G., J. Gieseke, M. von Falkenhausen, N. Morakkabati, and H. Schild (2005). Lung MRI at 3.0 T: a comparison of helical CT and high-field MRI in the detection of diffuse lung disease. *Eur Radiol 15*(2), 324–8.

Mai, V., K. Hagspiel, J. Christopher, H. Do, T. Altes, J. Knight-Scott, A. Stith, T. Maier, and S. Berr (1999). Perfusion imaging of the human lung using flow-sensitive alternating inversion recovery with an extra radiofrequency pulse (fairer). *Magn Reson Med 17*(3), 355–361.

Mai, V., J. Knight-Scott, and S. Berr (1999). Improved visualization of the human lung in ^{1}h mri using multiple inversion recovery for simultaneous suppression of signal contributions from fat and muscle. *Magn Reson Med 41*(5), 866–70.

Mai, V., B. Liu, J. Polzin, W. Li, S. Kurucay, A. Bankier, J. Knight-Scott, P. Madhav, R. Edelman, and C. Q. (2002). Ventilation-perfusion ratio of signal inten-

sity in human lung using oxygen-enhanced and arterial spin labeling techniques. *Magn Reson Med 48*, 341–350.

Mansson, S., E. Johansson, J. Svensson, L. Olsson, F. Stahlberg, J. Petersson, and K. Golman (2002). Echo-planar MR imaging of dissolved hyperpolarized 129Xe. *Acta Radiol 43*(5), 455–60.

McKinnon, G. (1993). On self-refocusing pulses for rapid gradient-echo imaging. *Magn Reson Med 29*(2), 260–2.

Miyazaki, M., S. Sugiura, F. Tateishi, H. Wada, Y. Kassai, and H. Abe (2000). Non-contrast-enhanced MR angiography using 3D ECG-synchronized half-Fourier fast spin echo. *J Magn Reson Imaging 12*(5), 776–83.

Muller, C., R. Loffler, M. Deimling, M. Peller, and M. Reiser (2001). MR lung imaging at 0.2 T with T1-weighted true FISP: Native and oxygen-enhanced. *J Magn Reson Imaging 14*, 164–168.

Muller, C., M. Schwaiblmair, J. Scheidler, M. Deimling, J. Weber, R. Loffler, and et.al. (2002). Pulmonary diffusing capacity: Assessment with oxygen-enhanced lung mr imaging preliminary findings1. *Radiology 222*, 499–506.

Ogasawara, N., K. Suga, M. Zaki, M. Okada, Y. Kawakami, and N. Matsunaga (2004). Assessment of lung perfusion impairment in patients with pulmonary artery-occlusive and chronic obstructive pulmonary diseases with noncontrast electrocardiogram-gated fast-spin-echo perfusion MR imaging. *J Magn Reson Imaging 20*, 601–611.

Oros, A. and N. Shah (2004). Hyperpolarized xenon in NMR and MRI. *Physics in Medicine and Biology 49*, R105–R153.

Reichenbach, J., T. Hacklander, T. Harth, M. Hofer, M. Rassek, and U. Modder (1997). ^{1}H T_1 and T_2 measurements of the MR imaging contrast agents Gd-DTPA and Gd-DTPA BMA at 1.5T. *European Radiology 7*, 264–274.

Richardson, D., J. MacFall, H. Sostman, and C. Spritzer (1994). Asymmetric-echo, short TE, retrospectively gated MR imaging of the heart and pulmonary vessels. *J Magn Reson Imaging 4*(2), 131–7.

Roberts, D., B. G. Warren, J. A. Hirsch, R. R. Rizi, L. Dougherty, R. E. Lenkinski, J. S. Leigh, Jr., and D. S. Mitchell (1999). Pulmonary perfusion: Respiratory-triggered three-dimensional mr imaging with arterial spin tagging-preliminary results in healthy volunteers. *Radiology 212*, 890–895.

Roemer, P. B., W. A. Edelstein, C. E. Hayes, S. P. Souza, and O. M. Mueller (1990). The NMR phased array. *Magn Reson Med 16*(2), 192–225.

Saro, J. P., J. A. Rafael, J. J. D. Lima, M. F. Botelho, and M. J. Ribeiro (2001). First pass evaluation of blood velocity in the pulmonary artery. *Nucl Med Commun 22*(7), 813–6.

Schreiber, W., B. Eberle, S. Laukemper-Ostendorf, K. Markstaller, N. Weiler, A. Scholz, K. Brger, C. Heussel, M. Thelen, and H. Kauczor (2001). Dynamic (19)F-MRI of pulmonary ventilation using sulfur hexafluoride (SF(6)) gas. *Magn Reson Med 45*(4), 605–13.

Wood, M. L., V. M. Runge, and R. M. Henkelman (1988). Overcoming motion in abdominal MR imaging. *AJR Am J Roentgenol 150*(3), 513–22.

Appendix A

Motion Correction Algorithm

The code that uses minimal variance algorithm to minimize amount of ghosting caused by motion the code is written to run in Matlab®. The following functions have to be activated on the MRI scanner in order to record data necessary for the reconstruction using this code.

- Function to put the pulse sequence in the debug mode and write k-space trajectory to a file. (Needed every time there is a scan parameter change that will effect k-space trajectory.)
- Function to turn off processing and sorting of k-space data.
- Function to save unmanipulated recorded data to the hard disk.
- Function to interface with the physiological monitoring system and write data to disk at a specified frequency.

The variables used to activate above functions can be found in the pulse sequence code.

The Matlab function to read raw data file header can be constructed using the PERL script downloadable at *http://rsl.stanford.edu/research/software.html.*

This function loads raw data file and a file with view ordering information into the `raw_data` variable.

```
function [raw_data,phdr,hdr,viewmap] = loadpfile;
```

```
[pfile_name, pfile_path] = uigetfile('*.7', 'Open a raw Pfile');
hdr.pfile_id = ...
fopen( [num2str(pfile_path) num2str(pfile_name)] , 'r', 'l');


    [vfile_name, vfile_path] = ...
    ...uigetfile( 'fse*' ,  'Open a fseopt_viewmap file' );
    s2 = ['viewmap =...
    ... load(''-ascii'', '''...
    ... ,num2str(vfile_path), num2str(vfile_name) ''');' ];
    eval(s2);
    clear('s2','vfile_path','vfile_name');


    s = dir([num2str(pfile_path) num2str(pfile_name)]);
pfilesize = s.bytes; clear('s');

phdr = readpfilehdr(hdr.pfile_id);


hdr.phdr_size = 61464;
hdr.filename = pfile_name;
hdr.path = pfile_path;
hdr.file_contents = phdr.rdb.file_contents ;
hdr.filesize = pfilesize;
hdr.run_int = phdr.rdb.run_int;
hdr.psd_iname = phdr.image.psd_iname;
hdr.freq  = phdr.rdb.da_xres;
hdr.phase = phdr.rdb.da_yres;
hdr.xres = phdr.rdb.da_xres;
hdr.yres = phdr.rdb.da_yres;
hdr.zres = phdr.rdb.rc_zres;
hdr.nslices = phdr.image.slquant;
hdr.nex = phdr.image.nex;
hdr.fov = phdr.rdb.fov;
hdr.etl = phdr.image.echo_trn_len;
hdr.slthick = phdr.image.slthick;
hdr.ex_desc = phdr.exam.ex_desc;
hdr.se_desc = phdr.series.se_desc;
hdr.coilname = phdr.image.cname;
        hdr.numcoils = 0;
        hdr.date = phdr.rdb.scan_date;
```

```
    [file_name, file_path] = ...
    ...uigetfile( 'ECG*' ,  'Open a Physiolgoical data file' );

    [token, rem] = strtok(file_name, '_' ); clear('token')
    Phys_files = dir(fullfile(file_path,['*',rem])); clear('rem')

    for f = 1:4
        clear('s1','s2')
        s1 = [ '[token,rem] = ...
...strtok(Phys_files(',int2str(f), ',1).name, ''_'');' ];
        eval(s1);
        s2 = ['phys_data.',...
...token ,' = load(''-ascii'', ''' ...
...num2str(file_path), token,rem,''');' ];
        eval(s2);
    end

    [e_m,e_n] = size(phys_data.ECGData);
    [r_m,r_n] = size(phys_data.RespData);

    et_max = max(phys_data.TrigEcg);
    rt_max = max(phys_data.TrigResp);

    if et_max > e_m
        etbad_indx = find(phys_data.TrigEcg > e_m);

        display(['Found a missmatch in a Trigger arrays'])
        display(['Removing index from TrigECG'])
        display(etbad_indx)
        phys_data.TrigEcg(etbad_indx) = [];

    end
    if rt_max > r_m
        rtbad_indx = find(phys_data.TrigResp > r_m);

        display(['Found a missmatch in a Trigger arrays:']);
        display(['Removing index from TrigResp:']);
        display(rtbad_indx);
        phys_data.TrigResp(rtbad_indx) = [];
    end

    [te_m,te_n]=size(phys_data.TrigEcg);
    phys_data.TrigEcg_orig=phys_data.TrigEcg;
```

```
        hdr.time = phdr.rdb.scan_time;

    if strncmp(hdr.coilname,'8HRBRAIN',4)  == 1
        hdr.numcoils = 8;
    elseif  strncmp(hdr.coilname,'HEAD AIN',4)  == 1
        hdr.numcoils = 1;
    elseif strncmp(hdr.coilname,'8US TORSOPA',4)  == 1
        hdr.numcoils = 8;
    else
         flag = 0
         while flag == 0
            disp(['I can not determine type of Coil! ']);
            hdr.numcoils = input('Enter number of coils: 1-16:');
            if hdr.numcoils < 1 | hdr.numcoils > 16
                flag = 0;
                disp(['Number of coils must be between 1 and 16!']);
            else
                flag = 1;
            end
        end
    end

xres = hdr.xres;
yres = hdr.yres*hdr.numcoils*hdr.nex;
pointer = hdr.phdr_size;
fseek(hdr.pfile_id,pointer,'bof');
raw_data.R = fread(hdr.pfile_id,[xres,yres],'short',2);
fseek(hdr.pfile_id,pointer+2,'bof');
raw_data.I = fread(hdr.pfile_id,[xres,yres],'short',2);
   eval(['p' num2str(phdr.rdb.run_int) '_raw_data = raw_data;']);
   eval(['p' num2str(phdr.rdb.run_int) '_hdr = phdr;']);
   eval(['p' num2str(phdr.rdb.run_int) '_viewmap = viewmap;']);
pfstatus = fclose(hdr.pfile_id);
if pfstatus == 0
    clear('pfstatus', 'pointer');
else
    disp(['ERROR closing file']);
end
```

This function loads physiological data recorded by the scanner.

```
function phys_data = Physdata
    clear('file_name', 'file_path');
```

```
    phys_data.TrigEcg = phys_data.TrigEcg_orig(1:2:te_m)

    figNumber = figure;
    [m,n] = size(phys_data.ECGData);
    x = 1:1:m;
    subplot(2,1,1), plot(x,phys_data.ECGData,...
    'b-',phys_data.TrigEcg,...
    phys_data.ECGData(phys_data.TrigEcg),'ko');
    subplot(2,1,2), plot(x,phys_data.RespData,...
    'r-', phys_data.TrigResp,...
    phys_data.RespData(phys_data.TrigResp),'ko');
    figure(figNumber);
```

This function sorts k-space into individual echoes arrays.

```
function  [sortedvmap, separated_data] = ...
separatepfile(hdr, raw_data, viewmap);

etl = hdr.etl;
nex = hdr.nex;
numchanels = hdr.numcoils;
newvmap=zeros(1,5);
echo_cntr=zeros(etl,1);
for view = 1:1:max(viewmap(:,4))
    echo=zeros(etl,4);
    pointer = etl*(view-1);
    echo(1:etl,:) =...
    viewmap((1+pointer):(etl+pointer),:);
        for num = 1:1:nex
echo_cntr=echo_cntr+1;
            echo(:,5) = echo_cntr;
            newvmap = cat(1,newvmap,echo);
end
end
sortedvmap = newvmap(find(newvmap(:,2)),:);

[m,n] = size(sortedvmap);
clear('R','I');

for echo = 1:1:max(sortedvmap(:,5))
    echoindex = 0;
    for index = 1:1:m
        if sortedvmap(index,5)==echo
```

```
            echoindex = [echoindex,index];
        end
    end
    echoindex(1)=[];
    pos_str=['separated_data.echo' ...
    num2str(echo) '.pos=sortedvmap(echoindex,2)'';' ];
    eval(pos_str);

    ch_pointer=0;
    for ch = 1:1:numchanels
        ch_pointer=(m+nex)*(ch-1);
        data_str=['separated_data.echo' ...
num2str(echo) '.ch' num2str(ch) '=...
raw_data.R(:,echoindex+ch_pointer) + ...
raw_data.I(:,echoindex+ch_pointer)*i ;'];
        eval(data_str);
    end
end
```

This function is the actual minimal variance algorithm.

```
function  echoes = minvar(phys_data,max,min)
[tm,tn]=size(phys_data.TrigEcg);
phys_data.TrigEcg_2RR=phys_data.TrigEcg(1:2:tm);
[m,n] = size(phys_data.ECGData);
x = 1:1:m;
for point = 1:1:m
    if (phys_data.RespData(point) ...
    < max) & (phys_data.RespData(point) > min)
    phys_data.RespAllow(point,1) = 1;
    else
    phys_data.RespAllow(point,1) = 0;
    end
end

[k,l] = size(phys_data.TrigEcg);
cntr = 0;
for triger = 1:1:k
    if phys_data.RespAllow(phys_data.TrigEcg(triger)) == 1
        cntr = cntr+1;
        phys_data.AllowedEcho(cntr,1) ...
= phys_data.TrigEcg(triger);
        phys_data.allowed_echonum(cntr,1) = triger;
```

```
    end
end

echoes = phys_data;
figNumber = figure;

subplot(2,1,1)
plot(x,phys_data.ECGData,'b-',...
    phys_data.TrigEcg,...
    phys_data.ECGData(phys_data.TrigEcg),'ko',...
    phys_data.AllowedEcho,...
    phys_data.ECGData(phys_data.AllowedEcho),'r*');
subplot(2,1,2)
plot(x,phys_data.RespData,'r-',...
    x,phys_data.RespAllow*(max-min)+min,'b-',...
    phys_data.TrigResp,...
    phys_data.RespData(phys_data.TrigResp),'ko');
figure(figNumber)
```

This function performs sorting of echoes according to the information provided from previous function. And reconstructs k-space data from all channels into a single magnitude image using SoS method.

```
function reconedimage = echorecon(separated_data, allowedecho, hdr);

xres = hdr.xres;
yres = hdr.yres;
numchanels = hdr.numcoils;

[m,n] = size(allowedecho');
fig_array = figure('Name', strcat('Images from individual Coil:'));
fig_comb = figure('Name', strcat('Reconed Image:'));

for ch=1:1:numchanels
    initpos_str = ['comb.pos.ch',num2str(ch),'=zeros(1,yres);'];
    initkdata_str = ['comb.kdata.ch',...
    num2str(ch),'=zeros(xres,yres);'];
    eval(initpos_str);
    eval(initkdata_str);

    for ec = 1:1:n
```

```
        clear('echo_cache','pos_cache');
        data_str = ['echo_cache = separated_data.echo',...
num2str(allowedecho(ec)),'.ch',num2str(ch), ';' ];
        pos_str = ['pos_cache = separated_data.echo',...
num2str(allowedecho(ec)),'.pos;' ];
        eval(data_str);
        eval(pos_str);

        if rem(allowedecho(ec),2) ~= 0
            echo_cache = echo_cache.*(-1);
        end

        [pm,pn] = size(pos_cache);
        for ec_indx = 1:1:pn
          combk_str=['comb.kdata.ch',num2str(ch),...
         '(:,pos_cache(ec_indx)) = [comb.kdata.ch',num2str(ch),...
         '(:,pos_cache(ec_indx))+echo_cache(:,ec_indx)];'];
         combp_str=['comb.pos.ch',num2str(ch)...
         ,'(pos_cache(ec_indx)) = [comb.pos.ch',num2str(ch),...
         '(pos_cache(ec_indx))+1];'];
         eval(combk_str);
         eval(combp_str);
        end
    end

    for av_indx = 1:1:yres
        avg_str=['comb.kdata.ch',num2str(ch),...
       '(:,av_indx) = comb.kdata.ch',num2str(ch),...
       '(:,av_indx)./(comb.pos.ch',num2str(ch),'(av_indx));'];
       kposit_str = ['kposit = comb.pos.ch',num2str(ch),'(av_indx);'];
       eval(kposit_str);
       if kposit==0
          disp(['Zero Line in kspace at:', num2str(av_indx)])
       else
          eval(avg_str);
       end

    end

    imgrec_str=['reconedimage.ch',num2str(ch),...
' = abs(fftshift(ifft2(comb.kdata.ch',num2str(ch),',xres,yres)));'];
    eval(imgrec_str);
```

```
    figure(fig_array),
    plot_str= ['subplot(2,',...
    num2str(numchanels/2),',',num2str(ch),...
    '), imshow(reconedimage.ch',num2str(ch),',[]);'];
    eval(plot_str);
end

imgsos_combined=zeros(xres,yres);
for chsum = 1:1:numchanels
    sos_str = ['imgsos_combined...
    = imgsos_combined + reconedimage.ch',num2str(chsum),'.^2;'];
    eval(sos_str);
end
imgsos_combined = sqrt(imgsos_combined);
reconedimage.combined = imgsos_combined;
figure(fig_comb), imshow(imgsos_combined,[]);
```